Addis Ababa University
አዲስ፡አበባ፡ዩኒቨርሲቲ
Seek Wisdom, Elevate your Intellect and Serve Humanity

Stability and Photovoltaic Performance Studies of Bulk Heterojunction Polymer Solar Cells

By

Endale Tsegaye Mohammed

A Thesis Submitted to
The Department of Chemistry

Presented in Fulfillment of the Requirement for the Degree of Doctor of Philosophy (Physical Chemistry)

Addis Ababa University
Addis Ababa, Ethiopia
February, 2017

Addis Ababa University

School of Graduates Studies

This is to certify that the thesis prepared by Endale Tsegaye Mohammed, entitled: *Stability and Photovoltaic Performance Studies of Bulk Heterojunction Polymer Solar Cells* and submitted in fulfillment of the requirements for the Degree of Doctor of Philosophy (Physical Chemistry) complies with the regulations of the University and meets the accepted standards with respect to originality and quality.

Signed by the Examining Committee:

External Examiner:______________________Signature:____________Date:___________

Internal Examiner:______________________Signature:_____________Date:__________

Internal Examiner:______________________Signature:_____________Date:__________

Advisor:______________________________Signature:_____________Date:__________

____

Chair of Department

Abstract

Stability and Photovoltaic Performance Studies of Bulk Heterojunction Polymer Solar Cells

Endale Tsegaye Mohammed
Addis Ababa University, 2017

This dissertation reports a research done on the stability and photovoltaic performance studies of bulk heterojunction polymer solar cells. Different techniques were used, in order to study the stability and performance of polymer solar cells fabricated using different polymers and fullerenes.

Two fullerene derivatives with different electron affinity were used to fabricate polymer solar cell based on P3HT as donor. Results obtained from UV-visible, FTIR and *J*-*V* measurement showed that the P3HT:PCBM film and solar cells fabricated from P3HT:PCBM as active layer have much better air stability than those made from P3HT:ICBA as active layer. Due to lower electron affinity of ICBA, the blend of P3HT:ICBA photobleached at a faster rate compared to PCBM.

Effect of sol-gel synthesized TiO_x layer on the stability and performance of P3HT:ICBA based solar cells were investigated by spectroscopic and electrical measurement methods. Results from *J*-*V* measurements indicates that P3HT:ICBA/TiO_x solar cell has better performance and stability compared to the reference device. The higher value of short-circuit current density and open-circuit voltage for P3HT:ICBA/TiO_x solar cell indicate the role of TiO_x layer as the optical spacer and hole blocking layer, respectively. The results from UV-visible absorbance, *J*-*V* and *C*-*V* measurement on light irradiated P3HT:ICBA/TiO_x solar cell demonstrates that TiO_x layer can be used to protect P3HT:ICBA active layer from oxygen and water attack under ambient air and to improve the working lifetime of P3HT:ICBA based device.

Investigation on the effect of two fullerene derivatives with similar electron affinity on the photovoltaic performance and stability of P3HT based solar cells is presented. From UV-visible measurements it is found out that P3HT mixed with both $PC_{61}BM$ and $PC_{71}BM$ has good ambient air photochemical stability. However, device based on P3HT:$PC_{61}BM$ has better stability compared to P3HT:$PC_{71}BM$ based device.

The impact of two different fullerenes with similar electron affinity on the photovoltaic performance and stability of PCDTBT based solar cells were studied. Results from UV-visible absorbance indicate that unlike that of pure film of PCDTBT, blend of PCDTBT with $PC_{61}BM$, $PC_{71}BM$ and 1:1 mixture of $PC_{61}BM$ and $PC_{71}BM$ has relatively constant absorbance under light exposure. The results show the stabilizing power of acceptor fullerenes when mixed with PCDTBT. The results from *J-V* measurement indicates that the solar cells made from PCDTBT:$PC_{61}BM$ and PCDTBT:$PC_{61+71}BM$ have better stability under light exposure in ambient air compared to the device based on PCDTBT:$PC_{71}BM$. When only $PC_{71}BM$ is used as acceptor the device has higher rate of decay of PCE.

The effect of DIM on the PCE and stability of PSCs made of PCDTBT:$PC_{71}BM$ is investigated. PCE of the device based on PCDTBT:$PC_{71}BM$ processed with DIM is higher than the reference device. In terms of device stability, the PSCs processed with DIM showed poor stability at longer light exposure time. For the device without DIM especially as the light exposure time was increased, the device stability was better. The result from IS measurement shows that for pristine PCDTBT:$PC_{71}BM$ devices with DIM, the active layer resistance is lower compared to device without DIM. However, after irradiating the device for 5 hr the resistance of the device processed with DIM is higher and it is consistent with decreased PCE of aged device.

The investigation presented on the application of NIL for performance improvement of organic solar cells shows that, NIL is really promising technique for improving efficiency of polymer solar cells. Nanopatterning of the PEDOT:PSS electrode can be used as a way to improve the cell efficiency. In our case relative increase of the 60%, from 0.8% to 1.3% of efficiency is obtained. The increased interfacial area and higher hole collection contributed for the improved photovoltaic performance of nanopatterned device.

Keywords: polymer solar cells, degradation, photochemical stability, lifetime, charge carrier mobility, P3HT, PCDTBT, ICBA, $PC_{61}BM$, $PC_{71}BM$, TiO_x, DIM, nanopatterning

Acknowledgments

First and foremost I would like to express my deepest gratitude and respect to my advisor Prof. Teketel Yohannes for his dedicated guidance, consistent supervision, helpful advice and sincere criticisms during the various stages of the research conducted, preparation of the progress report and final thesis. I also thank him for facilitating the research fellowship in ICTP-TRIL program for conducting part of my research work in Italy. For my stay in Italy, I were given financial support by "The Abdus Salam International Center for Theoretical Physics" (ICTP), the ICTP Programme for Training and Research in Italian Laboratories (TRIL) and IOM-CNR, therefore, it is a must to acknowledge both institutions.

I would like to thank Hawassa University for giving me the opportunity to continue my PhD study in Physical Chemistry. My appreciation also goes to Addis Ababa University, Department of Chemistry for providing me with the necessary facilities. I also thank Addis Ababa University, Department of Chemistry, Physical Chemistry stream members: Prof. Teodros Solomon, Dr. Ahmed Mustefa, Dr. Shimeles Admassie and Dr. Mesfin Redi for their comments and sincere criticisms on the research progress reports.

It is a must to express my sincere thanks to Dr. Massimo Tormen who has allowed me to do my research work in his laboratory at IOM-CNR Trieste, Italy. I really appreciate his follow up of my progress while I was in his laboratory and sharing his deep scientific knowledge and spirit. Working with him is really a blessing.

I would like to thank my labmates who offered countless hours of training, discussion and brainstorming in the area of polymer solar cells. Dr. Istem Özen thought me how to synthesize TiO_x. Dr. Simone Dal Zilio, Dr. Enrico Sovernigo, Dr. Alessandro Pozzato and Dr. Lisa Vaccari gave me training on the use of various instruments I used for characterization of polymer solar cells.

Finally, I would like to thank my father (Tsegaye Mohammed), mother (Worknesh W/Yesus), brothers, sisters and my friends (Dr. Fedlu Kedir, Bedasa Abdisa, Hagos Teku, Yishake Tsegazeab, Biniyam Berhanu, Dr. Andrea Radivo) for their continuous encouragement during my Ph.D study.

Table of Contents

List of Figures

List of Tables

List of Acronyms

A	acceptor
AM	air mass
AR	aspect ratio
BHJ	bulk heterojunction
CT	charge transfer
D	donor
DCB	dichlorobenzene
DIM	diiodomethane
DIO	diiodooctane
DTGS	deuterium tryglycine sulfate
EQE	external quantum efficiency
FF	fill factor
FTIR	fourier transform infrared spectroscopy
HOMO	highest occupied molecular orbital
ICBA	indene-C_{60} bisadduct
IQE	internal quantum efficiency
IS	impedance spectroscopy
ISOS-L	international summit on OPV stability-light
ITO	indium tin oxide
LUMO	lowest unoccupied molecular orbital
MALDI-TOF	matrix-assisted laser desorption/ionization time-of-flight
MIS	metal insulator semiconductor
MPP	maximum power point
nm	nanometer
NIL	nanoimprint lithography
OPV	organic photovoltaic
PA	polyacetylene
PAL	photoactive layer
PCE	power conversion efficiency
PCDTBT	poly[N-9'-hepta-decanyl-2,7-carbazole-alt-5,5-(4',7'-di-2-thienyl-2',1',3'-benzothiadiazole)]
$PC_{61}BM$	[6,6]-phenyl-C_{61}-butyric acid methyl ester

$PC_{71}BM$	[6,6]-phenyl-C_{71}-butyric acid methyl ester
PEDOT:PSS	poly(3,4-ethylenedioxythiophene):poly(styrenesulfonate)
PL	photoluminescence
P3HT	poly(3-hexylthiophene)
PPV	polyphenylene vinylene
PSC	polymer solar cell
PSN	polysulfur nitride
PTB7	Poly({4,8-bis[(2-ethylhexyl)oxy]benzo[1,2-b:4,5-b']dithiophene-2,6-diyl}{3-fluoro-2-[(2-ethylhexyl)carbonyl]thieno[3,4-b]thiophenediyl})
PV	photovoltaic
RH	relative humidity
rpm	rotation per minute
RT	room temperature
SCLC	space charge limited current
SEM	scanning electron microscopy
TFL	trap free limited
TGA	thermogravimetric analysis
TiO_x	titanium sub-oxide
UPS	ultraviolet photoelectron spectroscopy
WVA-NIL	water vapor assisted nanoimprint lithography
XPS	X-ray photoelectron spectroscopy

List of Symbols

A	area
A*	Richardson constant
Al	aluminum
d	gap between the electrodes
C	capacitance
C_{60}	buckminsterfullerene
E_g	bandgap
f	frequency
G	generation rate
I	illumination intensity
I	current
I_{ph}	photocurrent
I_{MMP}	current at maximum power point
I_{sc}	short-circuit current
I_D	diode current
I_o	reverse saturation current
I_{dark}	dark current
J	current density
J_o	reverse saturation current density
J_{sc}	short-circuit current density
k	Boltzmann constant
n_o	free charge carrier density
n_t	trapped carrier density
N_t	trap density
N_a	acceptor impurity concentration
n	diode ideality factor
N_c	density of states in the conduction band
N_v	density of states in the valence band
P	power
P_{max}	maximum light power
P_{in}	incident light power
P_c	charge collection probability

q	elementary charge
R	resistance
R_s	series resistance
R_{sh}	shunt/parallel resistance
T	absolute temperature
V	voltage
V_{bi}	built-in potential
V_{MMP}	voltage at maximum power point
V_{oc}	open-circuit voltage
W	depletion width
s	second
Z	impedance
Φ_b	barrier height
η	efficiency
θ	trap factor
ε	dielectric constant
ε_s	relative dielectric constant
ε_o	permittivity of vacuum
μ	charge carrier mobility
λ	wavelength
ω	angular frequency

1. Introduction

1.1. Background

The global energy supply is currently based mainly on fossil fuels such as oil, natural gas and coal. These fossil fuels cause serious environmental, political and social problems. Emissions from burning fossil fuels are adding to changes such as global warming (the green house effect) and ozone depletion, which are expected to have significant long term effects on the climate globally [1 - 3]. Another problem is created by the finite nature of fossil fuel resources. Therefore, it is imperative to look for sustainable energy sources that may solve the above mentioned problems. For several decades, (inter)national governments have made plans to reduce the economy's dependency on fossil fuels by the substitution of alternative energy sources such as renewable energy sources [4, 5].

Renewable energy sources are defined as any energy resource, naturally regenerated over a short time scale and derived either directly from the sun (such as thermal, photochemical and photovoltaic), indirectly from the sun (such as wind, hydropower and photosynthetic energy stored in biomass), or from other natural movements and mechanisms of the environment (such as geothermal and tidal energy) [6]. A photovoltaic (PV) energy technology is among the renewable energy technologies. It can contribute to environmentally friendly, renewable energy production, and the reduction of the carbon dioxide emission associated with the non-renewable and expensive fossil fuels and biomass [7, 8]. The most common photovoltaic energy technology is based on inorganic materials. An alternative to PV technologies based on inorganic semiconductors is polymer based photovoltaic energy technology.

Generally, photovoltaic devices are made of semiconductors materials (either inorganic or organic) sandwiched between two metallic electrodes, of which one is transparent. Organic materials have technological advantages over inorganic semiconductor materials. These are just few advantages: light weight, compatibility with flexible substrate and the possibility of easy integration into different large area flexible devices with different architecture, reduction of production costs by large scale manufacturing and the possibility of solution processing technologies (such as spin coating, printing, spray coating etc.) [9 - 17]. Currently the power conversion efficiency of polymer solar cells (PSCs) exceed to

12% [16 - 21]. However, short device working lifetime of polymer solar cells remains an obstacle. To make polymer solar cells competent with their counter inorganic solar cells their short device working lifetime needs to be improved.

The number of publications in the area of polymer solar cells shows that most attention by the researchers in the field is given for improvement of power conversion efficiency (PCE) of polymer solar cells rather than improving device stability [22]. Even if device stability problem is given relatively little consideration, it is very crucial issue [23]. For example, Figure 1.1 shows the number of peer reviewed scientific reports as a function of year of publication within the field of organic and polymer solar cells. As the data on the figure shows little attention has been given for the research in degradation of organic and polymer solar cells. According to the authors [23], the number of publications related to degradation accounts less than 5% of the published work in organic and polymer solar cells.

By different researchers it is found out that, when the polymer solar cells are exposed to high temperature, light, oxygen and water under an ambient environment, their performance declines because of the degradation of the nanoscale morphology, photo and thermooxidation of the donor polymer, oxidation of the electrodes etc. [24 - 29]. If the fabricated device has short working lifetime, then it is meaningless to fabricate a device with surprisingly high efficiency. Thus, to fabricate economically competent polymer solar cells, the research in improving PCE should go vis-à-vis device stability.

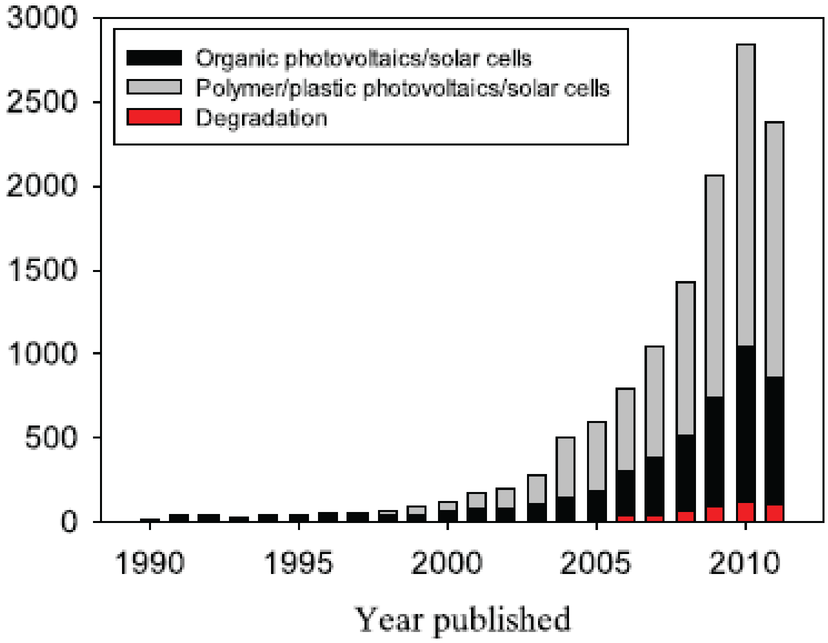

Figure 1.1: The number of peer reviewed scientific reports (on the y-axis) as a function of the year (on the x-axis) within the field of organic and polymer solar cells [23].

Despite the advantages of polymer solar cells, their device lifetime is still short to be commercialized. In the past it was the lower power conversion efficiency, which was the main problem but due to rapid development of conjugated donor materials and fullerenes the power conversion efficiency of polymer solar cells is approaching economically competent level [20, 30, 31]. To be commercialized, high-efficiency polymer solar cells should have economically acceptable device lifetime. For realization of polymer solar cells as a solution for the different problems associated with non-renewable energy sources, it is very important to improve their device working lifetime. Therefore, the main aim of this thesis work is to increase the knowledge in the area of stability and photovoltaic performance of polymer solar cells.

1.2. Objective of the study

General objective of this work is to study the stability and photovoltaic performance of bulk heterojunction polymer solar cells under ambient conditions by using electrical and spectroscopic techniques and provide better understanding of the factors contributing for degradation of PSCs.

Specific objectives of this work are:

- to study the effect of different electron affinity fullerene acceptors on photostability and performance of P3HT based polymer solar cells
- to identify the role of TiO_x interfacial layer on photostability and photovoltaic performance of P3HT:ICBA solar cells
- to investigate the impact of fullerene acceptors with similar electron affinity on photostability and photovoltaic performance of P3HT based polymer solar cells
- to explore the effect of different acceptor and their mixtures on photostability and performance of PCDTBT based polymer solar cells
- to study the influence of additive on photostability and performance of PCDTBT:$PC_{71}BM$ based polymer solar cells
- to show the effect of nanopatterning of PEDOT:PSS on photovoltaic response of P3HT:ICBA solar cells

1.3. Organization of the thesis

The organization of the thesis is as follows:

Chapter 1 is an introductory chapter presenting the general motivation of this thesis.

Chapter 2 introduces PSCs in general and the fundamental theoretical background for the understanding of the entire work.

Chapter 3 presents detailed experimental procedures, materials and methods used for fabrication and characterization of PSCs.

Chapter 4 presents experimental results and discussions.

- The first section (4.1) presents investigation on photodegradation of polymer solar cells where P3HT is blended with ICBA and $PC_{61}BM$.
- The second section (4.2) presents the effect of TiO_x interfacial layer on the photostability and photovoltaic performance of P3HT:ICBA solar cells
- The third section (4.3) describes the study of effects of similar electron affinity fullerene acceptors on device photostability of P3HT-based bulkheterojunction solar cells under illumination.
- The fourth section (4.4) describes the work on investigation on the effects of $PC_{61}BM$, $PC_{71}BM$ and their mixture on photostability and photovoltaic performance of PCDTBT:Fullerene solar cells
- The fifth section (4.5) presents the work on the effect of additive on the photostability and photovoltaic performance of PCDTBT:$PC_{71}BM$ based solar cells
- The sixth section (4.6) describes the results of the study on polymer solar cells fabricated using nanopatterned PEDOT:PSS.

Reference section lists the references cited in the thesis.

2. Polymer Solar Cells

2.1. Background

Polymers are large molecules or macromolecules, produced by joining together of many (10^2 - 10^6) small repeating units called monomers. Typical properties of polymeric materials include their strength, flexibility, elasticity, stability, mouldability, ease of handling etc. [32 - 34]. Traditionally polymers were seen as good electrical insulators and most of their applications had relied on their insulating properties [35]. Polymers have been extensively used by the electrical and electronic industry because of their insulating property. They were utilized as inactive packaging and insulating material.

In 1962 Pople et al. [36] predicted conducting polymer before their experimental discovery. The authors suggested that mobile defects if charged could be responsible for high electrical conductivity in polymers. In 1963 Weiss et al. [37] reported high conductivity in iodine oxidized polypyrrole. In 1973 Walatka et al. [38] showed that the inorganic polymer polysulfur nitride (PSN) is a metal. In 1977 Gill et al. [39] observed that the room temperature conductivity of PSN can be enhanced by an order of magnitude following exposure to bromine and similar oxidizing agents.

In 1977 major breakthrough in the area of conducting polymers happened when Shirakawa together with MacDiarmid and Heeger [40, 41] applied to polyacetylene (PA), an intrinsically insulating organic polymer the same redox chemistry used by Weiss et al [37] and Gill et al. [39]. They discovered that the conductivity of insulating PA, which had conductivity lower than 10^{-5} S/cm, can be increased up to10^3 S/cm at room temperature by exposing to oxidizing or reducing agent. This process of oxidation or reduction reactions which induce high conductivity are termed "doping" by analogy with the doping of inorganic semiconductors. However, the process of doping in conducting polymers is different from that of inorganic semiconductors. Therefore, through simple modification (doping) conjugated polymers can be conductive as good as metals. Conducting polymers combine the electrical properties of metals with the advantage of polymers such as lighter weight, resistance to corrosion and chemical attack, lower cost etc. [42, 43]. High conductivity of PA upon doping helped to launch the field of organic conducting polymers. In 2000 recognizing their breakthrough discovery of high conductivity in PA, A. J. Heeger,

A. G. MacDiarmid and H. Shirakawa jointly awarded the Nobel Prize in Chemistry [44], a well-deserved honor.

Due to their electrical, optical, mechanical and chemical properties conducting polymer were studied for their possible technological applications in many fields. Their potential application area includes, such as thin film transistors [45], polymer light emitting diodes [46], corrosion resistance [47], electromagnetic shielding [48], sensor technology [49, 50], molecular electronics [51], supercapacitors [52], and electrochromic devices [53]. Since the detailed survey of the applications of conducting polymer is beyond the scope of the present discussion, in the following section the application of conducting polymers in polymer solar cells will be highlighted.

Based on the current progress in PSCs research it is expected that PSCs will become a real competent to silicon solar cells because of two reasons. Silicon solar cells are currently costly and the device is not flexible. Because of simple device fabrication process, PSCs could be lower in price. PSCs can be fabricated on flexible substrate; therefore, they can be an ideal device where flexible solar cells are required [54].

The first thin film organic solar cell with efficiency about 1%, was reported by Tang in 1986 [55]. Despite the current intense research in PSCs, they have a lower power conversion efficiency (PCE) and shorter working lifetime compared to conventional photovoltaic systems. The laboratory based PCE of PSCs are improved from ~3% in 2001 to 12% [15, 17, 56 - 60]. However, commercially available crystalline silicon solar cell's PCE can reach over 25% [61, 62]. The difference in PCE of silicon solar cells in comparison with PSCs clearly demonstrates that, to be economically competent, a lot has to be done in the area of PSCs. One of the advantages of PSCs is that there are a number of conjugated polymers that could be used as potential photoactive layers [23, 63]. In the last 30 years, by engineering of the properties of conjugated polymers such as their bandgap and charge carrier mobility, a trend of PCE incremental has been observed. If the trend in PCE continues, in the future, there will be a hope that PSC can beat silicon based device.

The power conversion efficiency of PSCs has rapidly risen to surpass 12% [16, 17, 19 - 21, 64, 65]. However, the device stability under ambient working conditions is a major limitation. Generally, commercial crystalline silicon solar cells have a warranty of 25 years working lifetime [58, 66] which is much greater than the working lifetime of PSCs. To be commercialized, PSCs must have economically reasonable working lifetime. The main cause for degradation of PSCs is their sensitivity to oxygen, moisture and light [23, 24, 28, 67 - 71]. It is possible to protect the devices through cell encapsulation and device packaging, however, it is not economically acceptable solution because it will increase the overall production costs of the device and compromise the major advantage of PSCs, which is their expected lower cost. Thus, the best optimal solution is to search for stable conjugated polymers and fullerenes less sensitive to oxygen, moisture and light. In order to produce commercial PSCs, the PCE and working lifetime must be in the economically feasible level and this will require great attention from government (can formulate energy policies that favour research in PSCs), academia and industries working in the area of solar energy technologies.

2.2. Basic working principles of polymer solar cells

Conversion of light energy into electrical energy by PSCs can be described by the following steps (Figure 2.1) [17, 72, 73]: (1) a photon is absorbed by the active layer and an exciton (bound electron-hole pair) is formed, (2) the exciton then diffuses into a region where it dissociates into an electron and a hole, (3) the separated charges are transported to their respective electrodes, i.e. electrons to cathode and holes to anode.

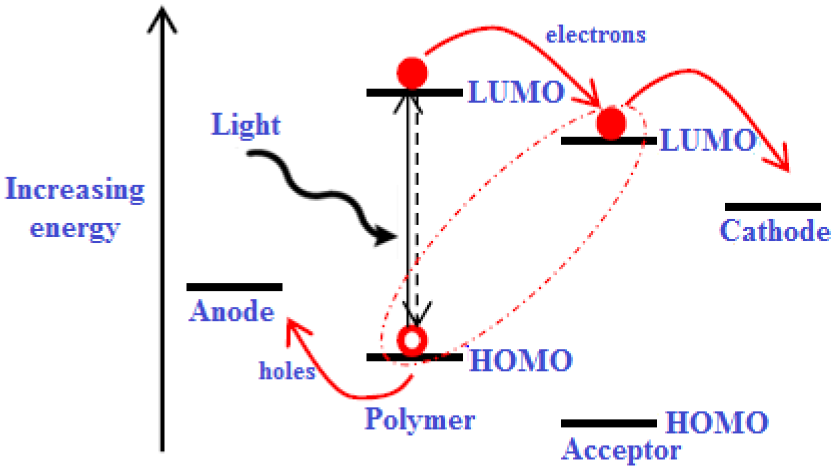

Figure 2.1: Working principle of a polymer solar cell.

Conversion of light energy into electrical energy by PSCs is not simple process as mentioned above. Rather it is complex. The complex process can be described as follows. From excitons, free charge carriers are generated by electron transfer from the LUMO of the electron donor (conjugated polymer) to the LUMO of the electron acceptor throughout the volume of the active layer [17, 74]. For efficient charge generation, an exciton photogenerated anywhere in the blend has to reach donor-acceptor interface within its lifetime; therefore, the magnitude of the maximum allowed phase separation is determined by the parameter called exciton diffusion length.

For efficient photovoltaic devices efficient charge generation is not the only condition. There are many more. The created charge carriers need to be transported to the corresponding electrodes within their lifetime, which will be a strong function of charge carrier mobility of the materials. The ability of transporting both charges in a blend of donor and acceptor materials will be also a strong function of morphology, i.e. creating interpenetrating, bi-continuous network of both materials. As a last step, charge carriers are extracted from the device through two selective contacts. A transparent indium tin oxide (ITO) coated glass matching the HOMO level of the conjugated polymer (hole contact) is used for extraction of holes and evaporated thin (80 - 100 nm) aluminum metal contact matching the LUMO of the electron acceptor (electron contact) is used for extracting electrons. Figure 2.2 shows the complete device structure of PSC.

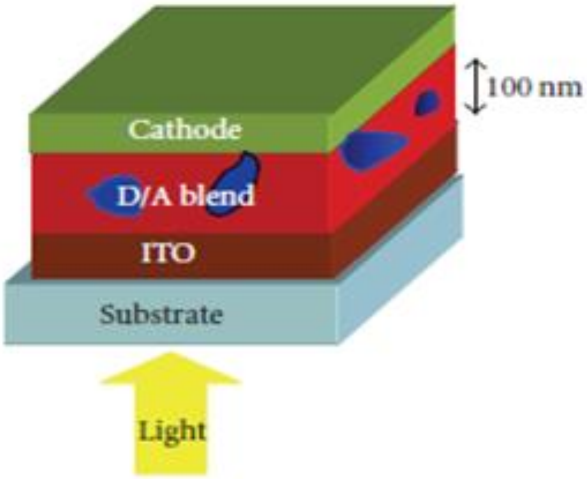

Figure 2.2: Diagram of the layered structure of a bulk heterojunction polymer solar cell.

2.3. Bulk Heterojunction Device Structure

Due to the low relative dielectric constant (mostly it is between 3 - 4) [75, 77] of organic semiconductors, photoexcitation leads to the formation of tightly bound electron-hole pairs, excitons, with binding energy of ~0.1 - 0.5 eV [77 - 80] significantly above the average thermal energy at room temperature (~0.025 eV) [17]. Because of low relative dielectric constant of organic semiconductors an energetic offset at the donor-acceptor (D-A) interface is needed to dissociate the excitons. Bulk heterojunction (BHJ) structure is introduced as a solution to the problem. Bulk heterojunction structure consists of active layers comprising blended donor polymer and acceptor fullerenes. Within a bulk heterojunction system, the energetic off-set between donor and acceptor materials provides the driving force for dissociate of the excitons [81].

BHJ is the most common and efficient system currently employed in the active layer of PSCs. It is a winner over flat structure. In a BHJ PSC, the active layer is a complex diffusive interface between the conjugated polymer and acceptor materials in the form of a 'bi-continuous interpenetrating network' to maximize the available interface area for efficient exciton dissociation (Figure 2.3). Using BHJ active layer architecture, best single or tandem PSC devices have been fabricated. From the absorbing sites the diffusion length of exciton is < ~ 10 nm [82 - 85]. BHJ structure has a nanoscale interpenetrating network with donor-acceptor phase separation in a length scale of 10 - 20 nm, which means each interface is within a distance accessible by excitons before their recombination. The introduction of BHJ PSCs leads to an enhancement of short circuit current due to an increased interface area which improved charge separation.

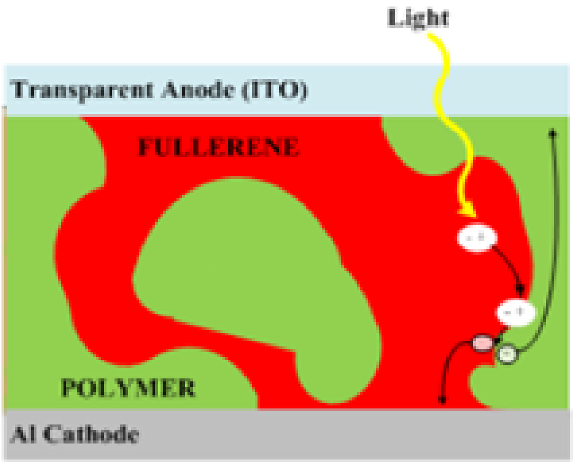

Figure 2.3: Interfacial exciton dissociation in a BHJ PSC [58].

2.4. Model for current-voltage characteristics of polymer solar cells

When a polymer solar cell made from a conjugated polymer with a bandgap, E_g, is irradiated by light, only photons with energy, $h\nu$, $> E_g$ contribute to the photocurrent and the output power. The equivalent circuit of PSC is shown in Figure 2.4(a). Photocurrent (I_{ph}) is the current due to generation of excess carriers by the absorption of the light. Current-voltage (I-V) characteristic under illumination (Figure 2.4(b)) is given by Equation (1) [86]:

$$I = I_o\left(exp\left(\frac{qV}{kT}\right) - 1\right) - I_{ph} \tag{1}$$

where I_o is the reverse saturation current of the diode, q is the elementary charge (1.6 x 10^{-19} C), k is the Boltzmann constant (1.38 x 10^{-23} J/K), T is the temperature in Kelvin and V is the applied voltage. Figure 2.4(b) shows a typical I-V characteristic of PSC in the dark and under illumination.

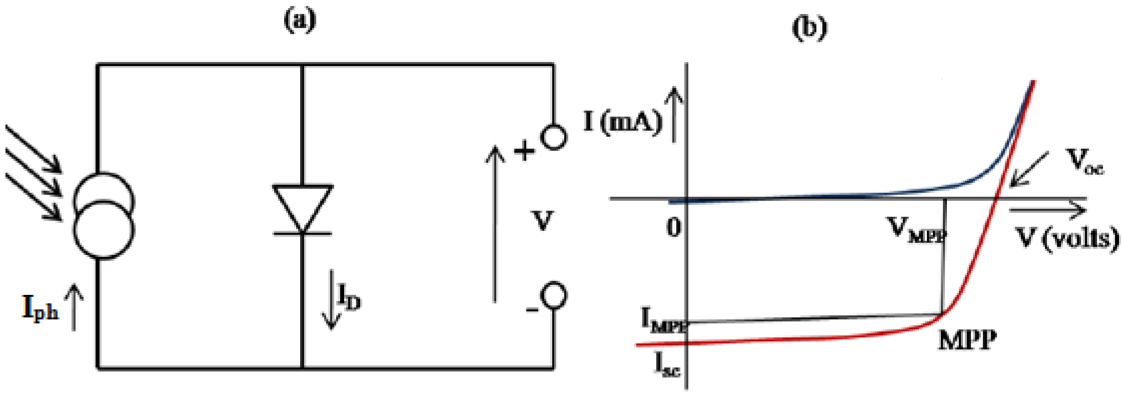

Figure 2.4: (a) Equivalent circuit of PSC. (b) *I-V* curve for PSC in the dark (blue) and under illumination (red) [58].

2.5. Current-voltage characteristics of polymer solar cells

When illuminated, PSC generates photocurrent and this photocurrent is plotted against voltage. As shown in Figure 2.4(b) the current-voltage curve of a solar cell can give the specific characteristic of the device. Four different parameters as described in this section can be extracted from *I*-*V* curve and used for device evaluation and for comparison with different polymer solar cells.

2.5.1. Short-circuit current density

Short-circuit current (I_{sc}) is the maximum current the solar cell can generate under a given illumination power when no voltage is applied across the device. That is, short-circuit current is the maximum current that flows under short circuit conditions. Short circuit current density (J_{sc}) is defined as I_{sc} per unit area. The photocurrent that is extracted from the solar cell can be affected by several factors. For example, absorption of light, degree of interpenetration of donor acceptor network, non-geminate recombination at the interface and charge carrier mobility in the individual donor acceptor phases determines short-circuit current of PSCs [82].

2.5.2. Open-circuit voltage

Open-circuit voltage (V_{oc}) is the voltage at which the photocurrent generated is zero or in other words the voltage across the open terminals of PSC. As shown in Figure 2.5 the maximum value of open-circuit voltage of polymer solar cells is related to the difference between the HOMO of donor and the LUMO of acceptor [87]. Under illumination and at the open-circuit condition, the V_{oc} equals the difference between the quasi-Fermi levels within the polymer and fullerene phase separated domains [64, 88]:

$$V_{oc} = \frac{1}{q}\left(E_{LUMO}^{fullerene} - E_{HOMO}^{polymer} - \Delta\right) - \frac{kT}{q} ln\left(\frac{n_e n_h}{N_c N_v}\right) \qquad (2)$$

where $E_{LUMO}^{Fullerene}$ is the LUMO energy level of fullerene derivatives; $E_{HOMO}^{Polymer}$ is the HOMO energy level of donor polymers, $N_{c(v)}$ is the density of conduction states at the band edge of the polymer and fullerene, k is the Boltzmann constant, Δ is the energy shift originating from disorder within the solution cast and phase separation, T is the absolute temperature.

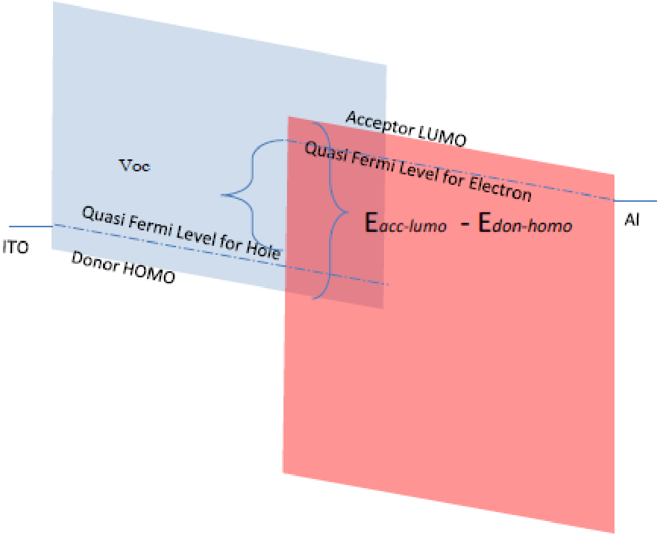

Figure 2.5: Origin of open-circuit voltage (V_{oc}).

V_{oc} can be affected by several terms, included in Equation (2). As it is evident from Equation (2), reduction in V_{oc} is observed in either of the two cases. The first case is when the effective bandgap of the polymer-fullerene blend decreases. Effective bandgap decreases when there is increase in the polymer chain packing leading to enhanced crystallinity, which in turn leads to increase in number of states in the HOMO (upward addition of states) and LUMO (downward addition of states) bands. Depending on the processing condition, the crystallinity of the polymer changes and those changes results in the change in bandgap [89 - 91]. The second case is when there are additional shunt pathways for charge carriers to travel to the opposite electrodes. If the photogenerated charge carrier finds an alternate low resistive path bypassing the junction of the bulk heterojunction, then it can reduce the amount of separation of both quasi fermi levels splitting due to the reduction in charge carrier density in the HOMO and LUMO bands and resulting in lower V_{oc}.

2.5.3. Fill factor

Fill factor (*FF*) is given by the ratio between the maximum obtainable power and the product of J_{sc} and V_{oc}. Fill Factor is the measure of the squareness of the *J-V* curve of the solar cell under light irradiation. It is indicator of the quality of the *J-V* characteristic of the solar cell [92]. Fill factor of a device is calculated as [82]:

$$FF = \frac{V_{MPP}}{V_{oc}} * \frac{J_{MPP}}{J_{sc}} \qquad (3)$$

FF is a very important parameter affecting the power conversion efficiency and it is affected by several factors such as shunt and series resistances, mismatching in charge carrier mobility (hole and electron) and charge carrier collection due to interface state recombination etc. [93]. High charge carrier mobilities lead to high *FF* values but any mismatch in charge mobilities would lower the *FF*. This is because lowering of mobility of one type of charge carrier leads to accumulation of charge carrier in either fullerene or polymer domain that would decrease built-in potential affecting the charge collection. Both mobility mismatch and trap assisted recombination are responsible for the inefficient charge carriers collection and hence reduction in *FF*.

2.5.4. Solar cell efficiency

The power conversion efficiency (PCE) denoted as η is the ratio of maximum output power (P_{max}) to the light power incident (P_{in}) on the active area of the device. The PCE of a solar cell can be expressed as follows [82]:

$$\eta = \frac{P_{max}}{P_{in}} = \frac{FF*V_{OC}*J_{SC}}{P_{in}} \tag{4}$$

P_{in} is the incident power density which is standardized at 1000 W/m^2 with a spectral intensity matching that of the sun on the earth's surface at an incident angle of 48.19° (AM 1.5) [94].

2.5.5. External quantum efficiency

Finally, a last important parameter experimentally accessible is the variation of J_{sc} with the wavelength (λ) of incident light. This value, called the external quantum efficiency (EQE) gives the ratio of collected charge carriers per incident photons:

$$EQE = \frac{1240*J_{SC}}{\lambda*P_{in}} \tag{5}$$

where λ is expressed in nanometers, J_{sc} in amperes per meter squared and P_{in} in watts per meter squared.

Generally, in polymer solar cells, the loss of EQE manifest itself when i) photons not absorbed in the photoactive layer (either reflected from the device or absorbed in a non-photoconductive layer), ii) singlet excitons recombine before reaching donor-acceptor interface, or at, the donor-acceptor interface, and/or iii) free electrons/holes recombine with holes/electrons within the photoactive layer.

2.6. Current-voltage characteristics of a ’real’ polymer solar cell

I-V characteristic of real PSC is affected by series resistance (R_s) and parallel (shunt) resistance (R_{sh}). The series resistance arises from the neutral region of the bulk of PSC material and the contacts, where as shunt resistance is due to current leakage e.g. due to surface conduction between the contacts. The equivalent circuit for PSC when series and parallel resistances are included is shown in Figure 2.6. Thus, the *I-V* characteristic taking into account the effects of the two resistances is [95]:

$$I = I_0\left(exp\left(\frac{q(V-I.R_S)}{nkT}\right)\right) + \frac{V-I.R_S}{R_{sh}} - I_{ph} \tag{6}$$

where n is the diode ideality factor.

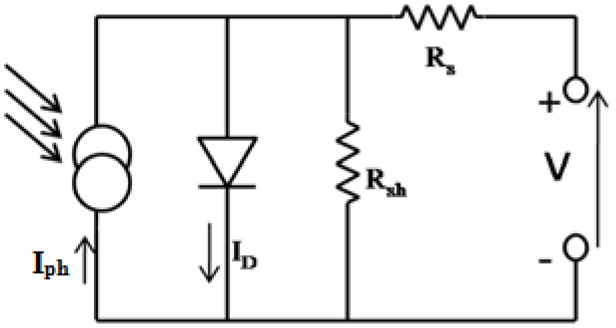

Figure 2.6: Equivalent circuit of PSC with R_s and R_{sh}.

2.6.1. Current-voltage measurements in dark for diode characteristics

From current voltage measurements of a p-n junction diode in dark under forward and reverse bias a lot of information can be extracted about the fundamental electronic processes occurring in the bulk and at the junction of the diode. From semilog plot of dark current *versus* voltage, information about transport mechanism and nature of recombination for different voltages can be evaluated. For example, from semilog plot of dark current *versus* voltage curve we can calculate both series and shunt resistance for a given solar cell as shown in Figure 2.7.

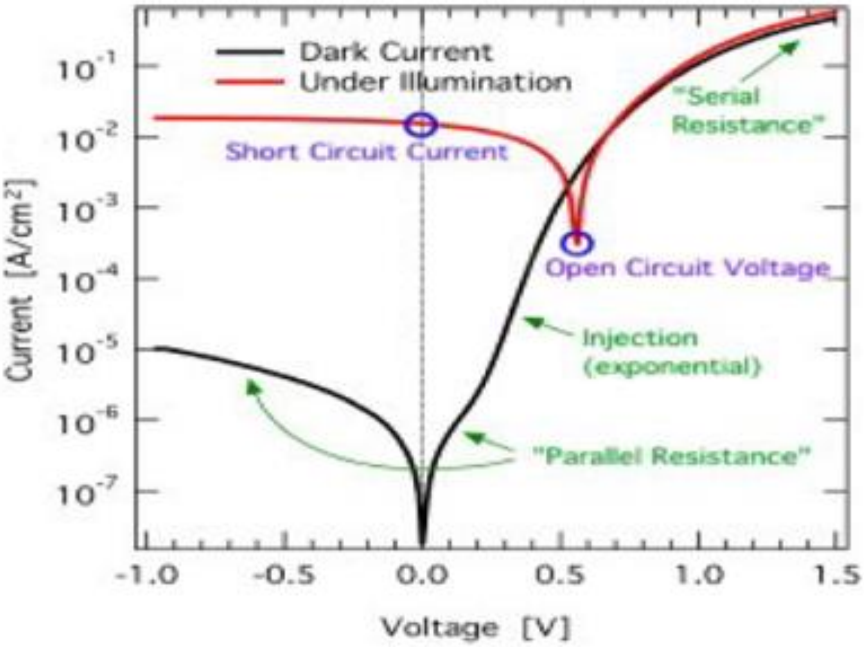

Figure 2.7: Comparision between dark current (black) with photocurrent (red).

2.6.1.1. Series resistance

Variations in series resistance (R_s) on the *I-V* characteristic influence the I_{sc} and the *FF*. Three different curves are presented in Figure 2.8: the red curve has the highest R_s whereas the black curve corresponds to the smallest R_s condition. As shown in Figure 2.8, for high R_s, *FF* and I_s are reduced. As shown in Figure 2.8, the slope in the 1st quadrant is reduced for higher values of R_s. The other thing we observe in Figure 2.8 is that, the V_{oc} remains unchanged for higher R_s. The reason is, at V_{oc} the current flow through R_s is zero.

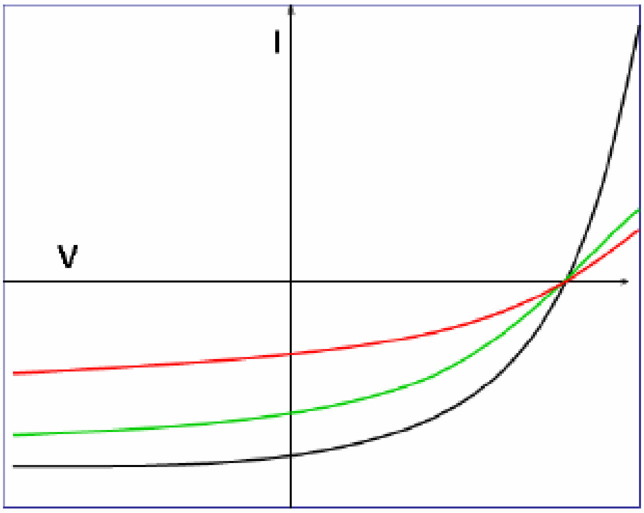

Figure 2.8: Effect of the series resistor on the *I-V* characteristic. The graph shows *I-V* curves for a low (black), medium (green), and high (red) value of R_s [96].

2.6.1.2. Shunt resistance

Figure 2.9 demonstrates the effect of R_{sh} on the *I-V* curve of solar cells. In Figure 2.9, three different curves are shown with different values of R_{sh}. The red line has the smallest R_{sh} while the dark curve corresponds to the highest R_{sh} situation. As it is exposed in Figure 2.9, a lower R_{sh} mean a reduction of the open-circuit voltage (V_{oc}) and *FF* of the device. However, short-circuit current of the solar cell is not affected by the value of R_{sh}.

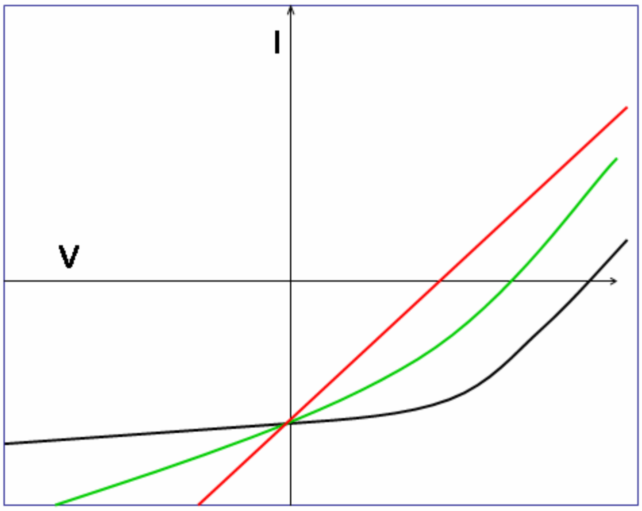

Figure 2.9: Effect of the shunt resistor on the *I-V* characteristic. The graph shows *I-V* curves for high (black), medium (green), and low (red) values of R_{sh} [96].

2.7. Stability of polymer solar cells

Stability of PSCs is very important for production of marketable device. In PSC, all layers undergo degradation either chemically or physically [23]. The short summary of the degradation mechanisms of different components of PSCs are discussed below.

2.7.1. Photooxidation of the donor material

Conjugated conducting polymers have an alternating single-double bond structure. The alternating single-double bond structure is responsible for the formation of a highly delocalized π-electron system with large electronic polarizability [92]. The active layer of polymer solar cells are generally constructed with conjugated polymeric compound, in which π-electrons are highly delocalized and therefore afford electro-optical properties such as photon absorption and charge carrier transport for device operation. Charge transport occurs along the short, undisrupted fragments of the polymeric chain by thermally-induced hopping [92, 97, 98]. When the π-conjugation in conjugated polymeric materials is disrupted by different factors such as chemical reactions, the optical absorption and charge transport properties of the conjugated materials are diminished, and as a result, the device performance of solar cells is deteriorated [22]. For polymers UV-visible absorbance is dependent on the length of π-conjugation and ordering of the polymer chains. Therefore, any chemical reaction that affect the degree of conjugation (disruption of the π-conjugation) and/or ordering of the polymer chains (e.g. due to chain scission) contribute to the solar cell PCE degradation.

P3HT is the most used polymer for PSCs. P3HT is known to have relatively higher stability than PPV derivatives, however it has poor stability and undergo photo-degradation under ambient conditions. It has been shown that in solution photooxidation and thermo-oxidation of P3HT originates from singlet oxygen photosensitization [99]. According to the proposed mechanism once singlet oxygen is formed, it reacts with thienyl unit of P3HT *via* 1, 4 Diels-Alder cycloaddition ultimately forming an unstable endo-peroxide that decomposes into sulfine and ketone and the final effect is disruption of the π-conjugation of the polymer [25, 99]. However, in the solid state the photooxidative degradation of P3HT is initiated from oxidation of the alkyl side chain instead of direct attack to the thiophene rings by singlet oxygen [25, 100 - 102]. According to currently accepted mechanism, degradation of P3HT involves the radical oxidation of the *n*-hexyl side chains and the subsequent degradation of the thiophene rings. Consequently the breaking of polymer backbone resulted in a loss of π-conjugation, provoking the bleaching of the sample. In UV-visible spectrum the loss of π-conjugation become visible in the form of decrease of optical absorption of the polymer.

By studying the degradation products of P3HT by IR and UV spectroscopy before and after exposure to UV-visible irradiation and thermal aging Manceau et al. [25, 101] identified carbonyl- and sulfur moieties in the degradation products. According to the authors, carbonyl moieties come from the degradation of the side chains (α-carbon atom of the hexyl group of P3HT which is the chemically weakest C-H bond) and sulfur moieties comes from the backbone (S-ring) of the polymer. Thus, the degradation products can be classified into two main families: carbonyl and sulfur-containing moieties. Thus, based on IR and UV spectroscopy identification of degradation products, Manceau et al. [25, 101]

proposed two mechanisms for the oxidation P3HT, which is the oxidation of side-chain and backbone of P3HT.

First let us see the first mechanism, that is, oxidation of side-chain of P3HT. In P3HT there exists unsaturation in the α-position to a methylene group. According to Manceau et al. [25, 101] the existence of unsaturation in the α-position to a methylene group reduces the C-H bond energy of the methylene and increased oxidizability of the carbon atom in the α-position to the unsaturation. The increased oxidizability of this carbon atom makes it the preferential site for a radical attack. Due to hydrogen abstraction on the carbon atom in the α-position to the thiophene ring there is formation of a macroalkyl radical. On the macroalkyl radical, successive oxygen fixation and hydrogen abstraction results in formation of α-unsaturated hydroperoxides. As shown in Figure 2.10 the photochemical and thermal decomposition of hydroperoxides yields alkoxy and hydroxy radicals. According to the proposal of Manceau et al. [25] based on IR studies, alkoxy radicals may react through three main pathways (Figure 2.10). The three degradation paths are: (i) Hydrogen abstraction reaction of alkoxy radicals leading to the formation of an α-unsaturated alcohol, (ii) the cage reaction of alkoxy radicals with $HO^{\cdot}$ leading to the formation of an aromatic ketone, (iii) β-scission leading to the formation of an aromatic aldehyde that rapidly oxidizes into carboxylic acids. The second mechanism is the oxidation of the sulfur atom present in the backbone of the thiophene ring first into sulfoxides then to sulfones (Figure 2.11).

The effect of the above mentioned reaction is a loss of π-conjugation, provoking the bleaching of the sample that leads to reduction of photon absoprption [103]. Decrease of photon absoprption is among the factors responsible for the reduction of J_{sc}. The other effect of photodegradation is chain scission that results in hole mobility reduction. The products of photodegradation also act as charge trapping centers. All the above mentioned effects of photodegradation result in reduction of power conversion efficiency and device working lifetime.

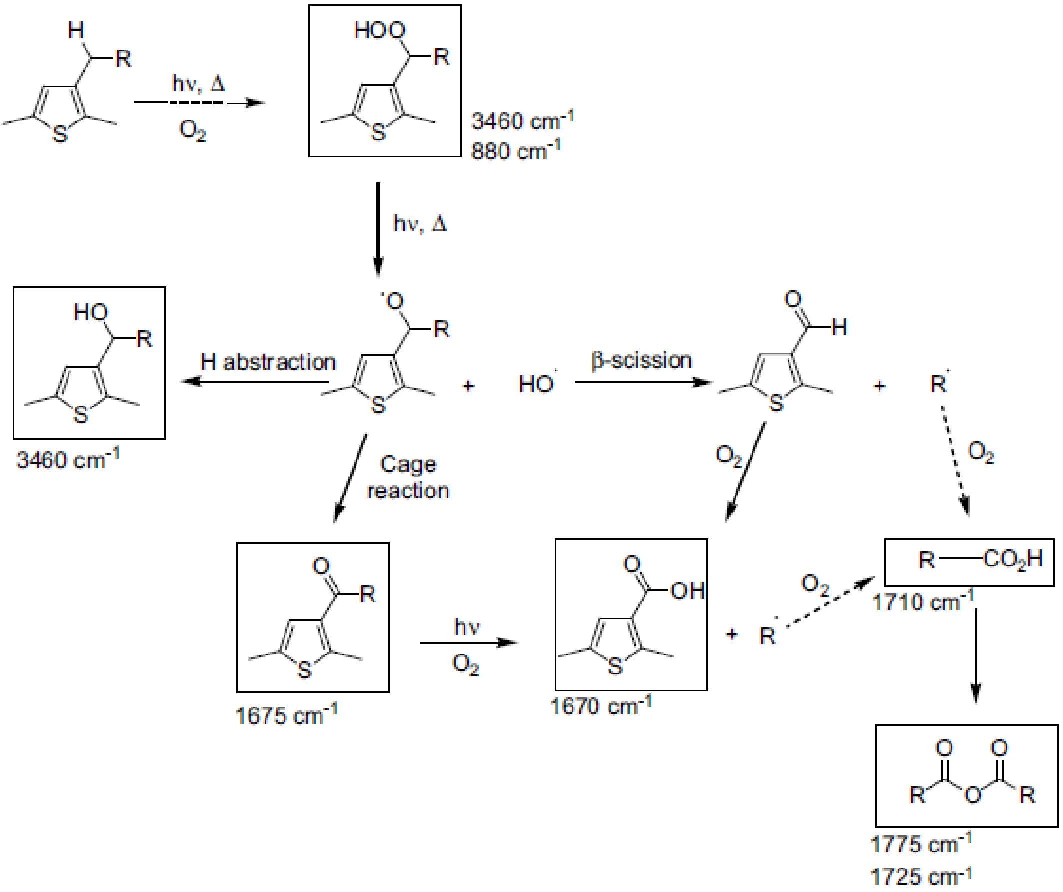

Figure 2.10: Oxidation mechanism of the P3HT alkyl side chain [25].

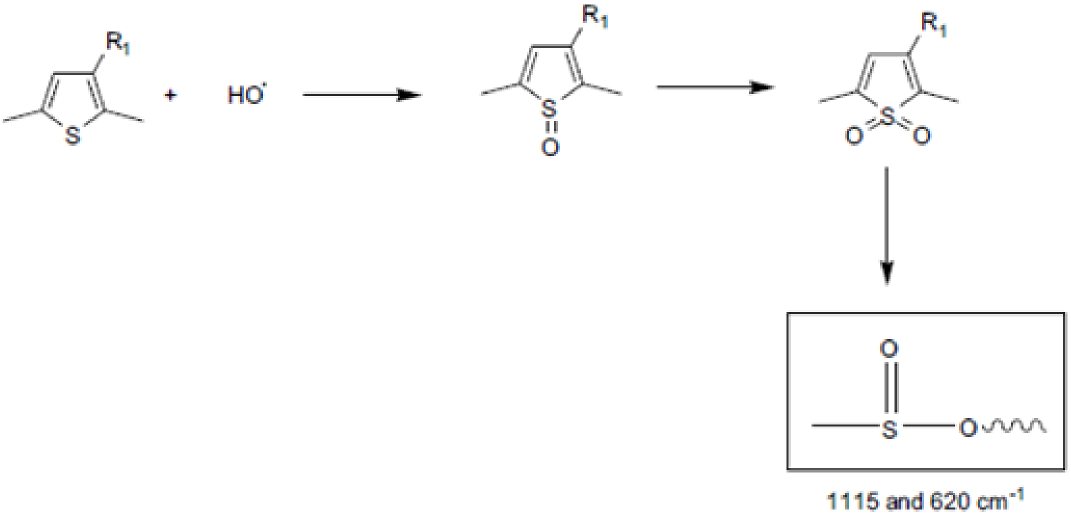

Figure 2.11: Oxidation mechanism of the sulfur atom of the thiophene ring [25].

Systematic study of the influence of environmental factors, namely oxygen, light and moisture, on the photodegradation of neat P3HT film showed that limited, short-term exposure of the P3HT to only one of the degradation activators only causes small irreversible damage of the polymer [104]. In contrast, exposure of P3HT to both UV and oxygen was found to lead to accelerated photooxidation of P3HT structure and consequently significant deterioration of its optical properties.

Nowadays, low bandgap polymers have been considered as the most promising candidates for highly efficient PSCs because their absorption ranges can be extended to longer wavelengths. PSCs based on low bandgap polymers have relatively high PCE. However, the photooxidative degradation and stability issues of low bandgap polymers based solar cells are a problem. PCDTBT is low bandgap polymer with high PCE. Tournebize et al. [105] studied the impact of UV-visible light on the morphology and photochemical behavior of PCDTBT and proposed mechanism for photooxidation process. Based on their experiment, they found out that the photooxidation of PCDTBT involves two phases and they proposed degradation mechanism that accounts for the correlations between the modifications of the chemical structure, the loss of absorbance and the evolution of the nanomechanical properties of PCDTBT under light exposure.

According to the authors, the two successive phases can be described as follows. The first phase (1) is depicted in Figure 2.12. The first phase consists of: (i) Absorption of light by PCDTBT lead to photochemical dissociation of the C-N bond, resulting in formation of polycarbazolyl radical on the main chain and an alkyl radical. (ii) After hydrogen abstraction on the C_{tert} atom, oxidation of the pendant alkyl substituent. (iii) Formation of carbonyl photoproducts. Carbonyl photoproducts are susceptible to migration into the gas phase, and recombination with the polycarbazolyl radical, ending up in cross-linking of the backbone. On the second phase (2) the radicals formed along the oxidation of the alkyl side chains and chain scissions of the backbone leads to oxidation of the thiophene rings of the backbone.

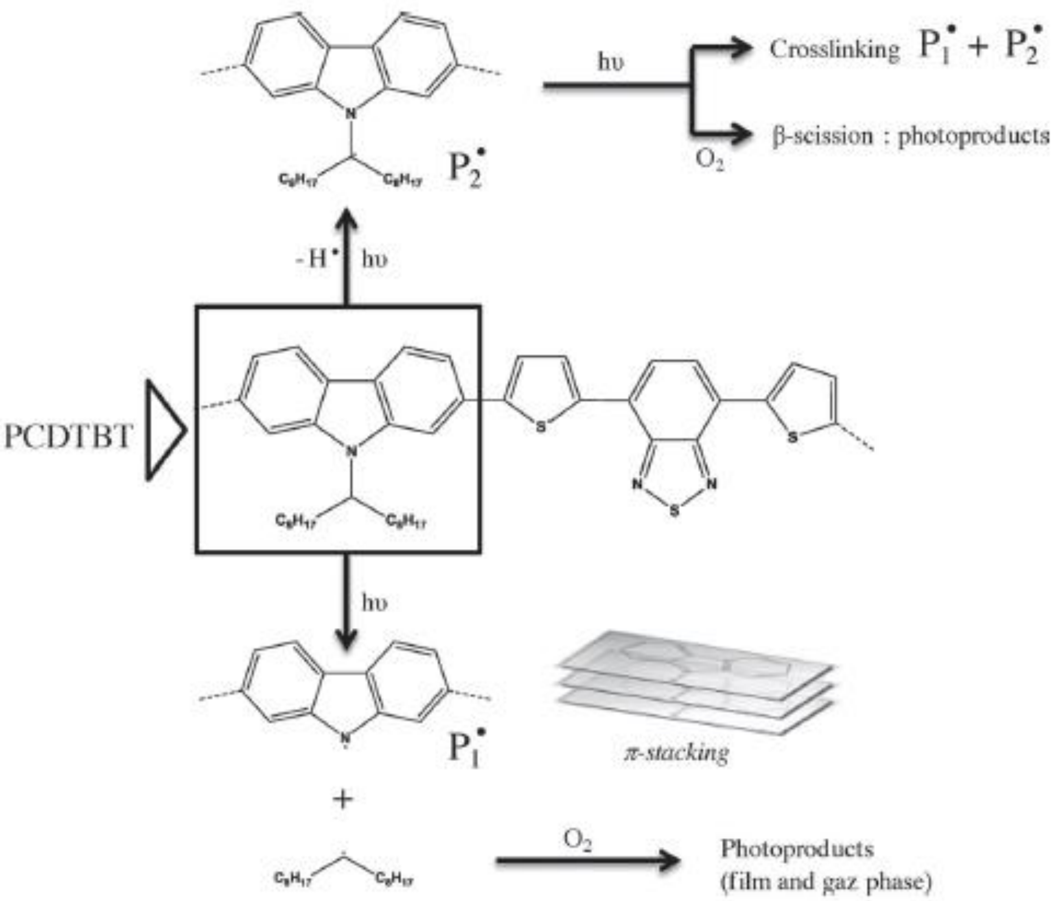

Figure 2.12: Photochemical reactions of the 2, 7 carbazole unit in PCDTBT upon irradiation at λ > 300 nm in ambient air [105].

The results from Tournebize et al. [105] reveals the close relationship between the effects of UV-visible light irradiation on the chemical structure of PCDTBT and the reduction in its π-conjugation length. Based on their experimental results they concluded that the instability of the tertiary carbon atom bearing the alkyl chains is the source of failure of the entire PCDTBT backbone. The authors recommended the replacement of tertiary carbon atom by a quaternary carbon atom. For example, substitution of the hydrogen atom by a methyl group may result in a considerable improvement in the stability of PCDTBT film under irradiation in the presence of oxygen.

2.7.2. Degradation of acceptor

Fullerene is the most commonly used acceptor material in PSCs. Its stability significantly affects the performance and stability of PSCs. Therefore, it is good to study and know the degree of stability of different fullerenes at different environmental conditions. According to TGA measurements performed in inert atmosphere and in air, in inert atmosphere, fullerene and fullerene derivatives are expected to be thermally stable at the operating temperature of the PSC, i.e. about 80°C [92, 106, 107]. However, fullerene can be degraded in the presence of oxygen [108]. Experimentally, it was found out that when fullerene is exposed to oxygen, the conductivity of fullerene films lowers. The reason is that upon oxygen uptake, the electron mobility is reduced by several orders of magnitude because the intercalated oxygen acts as an electron trapping site [109].

Exposure of fullerene to (UV) light enhances oxygen diffusion through the interstitial voids in the fullerene lattice, as well as formation of C-O and/or inter-fullerene C-C bonds [110 - 112]. Longer light exposure of fullerene results in oxidation of the molecule. For instance, when $PC_{61}BM$ is exposed to light in the ambient environment for 1000 hr, the oxidation products of $PC_{61}BM$ are generated [113, 114]. The result from MALDI-TOF experiment shows that the mass difference between oxidation products and $PC_{61}BM$ is n x 16 (where n = 1 to 8) m/z. Based on the result from MALDI-TOF, the sound conclusion is that PCBM is oxidized successively by addition of one oxygen atom at each step. The deleterious consequence is that the traps formed by oxidized PCBM reduce the charge carrier mobility in the $PC_{61}BM$ domain [109, 115]. The reduced charge carrier mobility creates space charge effect and reduces fill factor.

2.7.3. ITO electrode

ITO electrode is sensitive to acidic compounds and when it comes into contact with acidic media it will be etched and released indium atoms which diffuse into other layers [116]. ITO is a brittle material. It is susceptible to cracks upon bending of the flexible substrate onto which it is deposited. The formation of crack and its propagation in the ITO layer makes obstacle for charge transport and increases the sheet resistivity [117]. Some of the alternatives of ITO are doped metal oxides, organic polymers, metal grids, carbon nanotubes and graphene [118 - 121].

2.7.4. PEDOT:PSS

Due to its excellent thermal stability, transparency, conductivity and its ease-of-processing, PEDOT:PSS is widely used as a buffer layer between the ITO and the photoactive layer (PAL) of PSC devices. PEDOT:PSS is hygroscopic and its degradation depends on humidity. Mainly due to its hygroscopic nature PEDOT:PSS is at the heart of PSC degradation [122]. Because of absorption of water by PEDOT:PSS there will be formation of spatially inhomogeneously distributed insulating areas at the interface between the PEDOT:PSS and photoactive layer. This invites a reduction of the photoactive layer:electrode interface area with proportional decrease in the device J_{sc} and FF [123].

According to experimental results obtained from Rutherford back scattering spectrometry, the ITO/PEDOT:PSS interface can be unstable. When ITO comes in contact with PEDOT:PSS, due to acidic nature of PSS there is ITO etching [116]. Because of etched ITO the released indium ions may diffuse through the PEDOT:PSS to the photoactive layer. Generally, degradation of the quality of the ITO/PEDOT:PSS interface considerably affects the overall power conversion efficiency of the polymer solar cell.

2.7.5. Metal electrode

Because of the possibility to deposit metals as electrically conductive film they are widely used as electrodes for PSC. The cathode is generally a lower work function metal deposited on top as the last layer on the PSC. When exposed to ambient air the main problem of low work function metal electrode is its easy oxidation leading to formation of oxidized metal complex which changes the work function of the cathode. The most commonly used metal for the electrode of PSCs is aluminum (Al). For example, Al is highly reactive with oxygen or water due to its low workfunction and result in formation of electrically insulating metal oxide. Due to formed metal oxide, series resistance of the solar cell increases and the effeciency of electron collection reduced which resulting in poor performance and shorter device working lifetime [22, 23].

2.8. Electrical properties of semiconducting polymer-metal contacts

The current density-voltage (*J*-*V*) properties of Schottky barrier device with rectifying *J*-*V* behavior are usually assumed to follow the standard thermionic emission theory for conduction across the junction [86]. According to this theory the current is assumed to be controlled by the transfer of carriers across the interface of metal/semiconductor. The forward current-voltage characteristics of an ideal Schottky barrier diode was first explained by Bethe's thermionic equation as [86, 124]:

$$J = J_o[exp(\frac{qV}{kT}) - 1] \tag{7}$$

where J = total current-density, J_o= reverse saturation current-density, q = charge of electron (1.6 x 10^{-19} C), k = Boltzmann constant (1.38 x 10^{-23} J.K^{-1}), T = absolute temperature in degree Kelvin, V = applied forward voltage.

Most practical Schottky diodes show deviations from ideal thermionic emission behavior because of the introduction of imperfection at the junction during the time of fabrication. Therefore, a dimensionless parameter called the ideality factor, n, is usually included in the *J*-*V* relationship to take into account non-ideal behaviors [86]:

$$J = J_o[exp(\frac{qV}{nkT}) - 1] \tag{8}$$

For ideal Schottky diodes $n = 1$. However, n has usually a value greater than unity.The case where $n > 1$ have been ascribed to several effects [125, 126]: (1) interface states as a thin oxide between the metal and the semiconductor [127], (2) tunneling currents in highly doped semiconductors [128], (3) generation/recombination currents within the space-charge region [86].

The reverse saturation current density is given by the Richardson equation [86]:

$$J_o = A^*T^2exp(-q\Phi_b/kT) \tag{9}$$

where A^* is the Richardson constant for free electron and usually assumed as 120 A/cm^{2}K^2 for a Schotttky diode with p-type organic semiconductor in a barrier hight (Φ_b) claculation [129, 130].

From Equation (8), with $qV >> kT$, lnJ *versus* V is expected to be linear, in the vicinity of the turn on voltage, with an intercept corresponding to J_o. When J_o is very small compared with the current density of experimental interest, the contact will effectively block current flow for one sign of the applied voltage (reverse bias). This type of device will also display an exponentially increasing current when the bias voltage is of the opposite polarity (forward bias). When all other factors are held constant, very low value of J_o corresponds to a better rectification property. For such a low value of the reverse saturation current density, J_o, the barrier height is considered high. Rectifying contacts are desirable for photovoltaic cells, photon detectors, field effect transistors, chemical sensors and numerous other applications [131, 132]. The value of diode ideality factor (n) is determined from the slope of the linear region of the forward bias lnJ-V characteristics.

The value of the barrier height, Φ_b, can be calculated from Equation (9) and it is given by:

$$\Phi_b = (kT/q)ln(A^*T^2/J_o) \tag{10}$$

For metal/semiconductor contacts, the series resistance is an important parameter affecting the electrical characteristics of the Schottky diodes. The Schottky diode parameters such as the barrier height, the ideality factor and the series resistance can also be obtained by using a method developed by Cheung et al. [133]. According to Cheung et al. [133] the forward bias J-V characteristics due to the thermionic emission of a Schottky diode with series resistance can be expressed as:

$$J = J_o[exp(q(V-JR_s)/nkT) -1] \tag{11}$$

where the term JR_s is the voltage drop across series resistance of the device. The value of the series resistance can be determined from the following functions using Equation (11):

$$dV/d(lnJ) = (nkT/q) + JR_s \tag{12}$$

$$H(J) = V - (nkT/q)ln(J/A^*T^2) \tag{13}$$

And $H(I)$, Cheung function, is given as follows:

$$H(J) = n\Phi_b + JR_s \tag{14}$$

From Equation (12) the plot of $dV/d(lnJ)$ *versus* J will be linear and gives R_s as the slope and nkT/q as the y-axis intercept. Therefore, from Equation (12) the values of n and R_s can be calculated. Using the value of n obtained from Equation (12), the value of Φ_b and R_s can be obtained from the plot of the function $H(J)$ *versus* J as given by Equation (14).

2.9. Space charge limited current

The study of injection currents is a viable way for obtaining information about charge carrier transport and defect states in the forbidden gap in semiconductor materials. Localized defect states in diodes or solar cells have a strong influence on the injected current in response to an applied voltage. Not only the magnitude of the current, but the actual form of the current-voltage characteristics is influenced by the interaction of the injected charge carriers with such defect states. From the resulting form of current-voltage characteristic a number of information can be extracted about the material under study. Figure 2.13 shows the ideal current-voltage characteristics for single-carrier injection into a material with a single discrete trapping level [134, 135]. Single injection is defined by one-carrier flow and is a unipolar analysis. For solids with single trapping center the detail of current-voltage characteristics is discussed by M. A. Lampert and P. Mark et al. [134, 136] and here the short review is given.

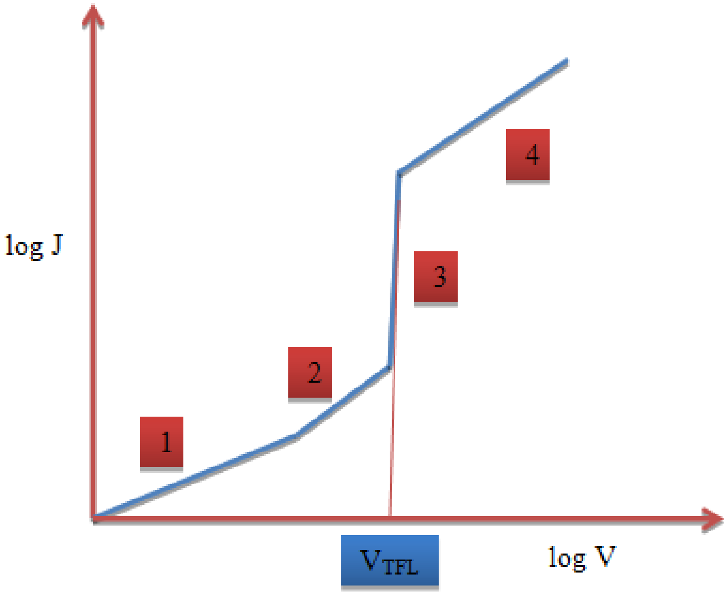

Figure 2.13: Ideal *logJ-logV* plot for single carrier injection into a material with a single discrete trapping level. The plot shows four different regions: 1. ohmic region, 2. Trap limited regions, 3. Trap limited region transition and 4. Trap free region.

At low voltage (region 1), Ohm's law dominates the current-voltage characteristics due to the presence of thermal equilibrium free carriers. The current-density (J) within the ohmic region is described by the following equation [137 - 139]:

$$J = (qn_o\mu V)/d \tag{15}$$

where V is applied voltage, q is the electronic charge, d is the gap between the electrodes, μ is the charge carrier mobility and n_o is the free charge carrier density.

When the voltage becomes large enough, the space charge limited current (SCLC) starts to be noticeable and enters the trapping field region (region 2). In the presence of traps the space charge limited current is then given by [140, 141]:

$$J = (9\varepsilon_s\varepsilon_o\theta\mu V^2)/8d^3 \tag{16}$$

where ε_s is the relative dielectric constant of the semiconductor, ε_o is the permittivity of vacuum, θ is the trap factor, it is the ratio of free to total charge ($\theta = 1$ for a trap free semiconductor).

The trap factor, θ, is given by:

$$\theta = n_o/(n_o + n_t) \tag{17}$$

where n_o is the free carrier density and n_t is the trapped carrier density.

In region 3, as the voltage increases further, more charges are injected and eventually, these injected charges fill all the trapping sites and reduce the concentration of empty traps resulting in an increase in the carrier mobility and as a result an increase in current in a power law, $J \sim V^m$. At the trap-filling-limit, the entire population of traps will be filled and the current rises nearly vertically (region 3) [135]. At high applied voltage, when all the traps are filled, the injected charges will be free to move and the current follows $J \sim V^2$ relation. The current densty-voltage relationship is characterized by the trap-free-square law (region 4) as follows:

$$J = (9\varepsilon_s\varepsilon_o\mu V^2)/8d^3 \tag{18}$$

Equation (18) is known as the Mott-Gurney square law and Childs law for solids [141, 142]. This square law is the reason why space charge limited current characteristics are typically shown on a *log-log* plot.

The transition voltage between the trap charge limited and trap free limited for shallow traps confined in discrete levels is given by [135, 142 - 144]:

$$V_{TFL} = (qN_t d^2)/2\varepsilon_s\varepsilon_o \qquad (19)$$

where N_t is the trap density. The effective carrier concentration n_o in the active region is given by the expression [99]:

$$J(2V_{TFL})/J(V_{TFL}) \approx N_t/n_o \qquad (20)$$

where $J(V_{TFL})$ is the current density at V_{TFL} and $J(2V_{TFL})$ is the current density at a voltage twice of the V_{TFL}.

2.10. Capacitance-voltage characteristics

For Schottky barrier diode, capacitance-voltage (C-V) measurement is very important to analyze interlayer states. On reverse bias voltage case, the dependence of capacitance on voltage can give some diode parameters such as the dopant concentration and built-in potential. Mott-Schottky relationship is used to determine the dopant concentration as given below [145 - 147]:

$$C = [(A^2\varepsilon_s\varepsilon_o qN_a)/2(V_{bi} - V)]^{1/2} \qquad (21)$$

$$C^2 = [(A^2\varepsilon_s\varepsilon_o qN_a)/2(V_{bi} - V)] \qquad (22)$$

$$1/C^2 = 2(V_{bi} - V)/(A^2\varepsilon_s\varepsilon_o qN_a) \qquad (23)$$

where, C is the capacitance, V_{bi} is the built-in potential, V is the applied voltage in the reverse direction, A is the device area, q is the elementary charge, ε_s is the relative dielectric constant of the semiconductor, ε_o is the permittivity of free space and N_a is doping concentration in the semiconductor. From Equation (23), it is clear that by plotting C^{-2} *versus* V, a straight line can be obtained and the intercept (at $C^{-2} = 0$) gives the built-in potential (V_{bi}). The dopant concentration in the semiconductor (N_a) is given by:

$$N_a = (2/(q\varepsilon_s\varepsilon_0 A^2))(dV/dC^{-2}) \qquad (24)$$

For semiconductor with uniform dopant concentration by substitution of Equation (21) into the relation $\varepsilon_s\varepsilon_o/W = C/A$, the depletion width, W, of the Schottky junction can be obtained as:

$$W = [2\varepsilon_s\varepsilon_o(V_{bi} - V)/qN_a]^{1/2} \qquad (25)$$

2.11. Impedance spectroscopy

Impedance spectroscopy (IS) is a very useful technique for characterization of the electrical properties of polymer solar cells [148 - 153]. In IS the sample under investigation is subject to a small voltage signal $v(t) = V_m(t)*\sin(\omega t)$ with angular frequency, $\omega = 2\pi f$ and the complex impedance is measured by means of the induced current, $i(t) = I_m(t)*\sin(\omega t + \theta)$, where θ is the phase difference between the voltage and the current. Thus, impedance, $Z(\omega)$ is defined as:

$$Z(\omega) = \frac{v(t)}{i(t)} \tag{26}$$

The parallel *RC* circuit is an equivalent circuit model for a junction between a metal and a semiconductor. Let us consider a parallel *RC* circuit whose complex impedance is given by:

$$Z = \frac{R}{1+j\omega RC} \tag{27}$$

and $Re(Z) = \frac{R}{1+\ \omega^2\tau^2}$, $-Im(Z) = \frac{R\omega\tau}{1+\ \omega^2\tau^2}$ where $\tau = RC$

The impedance is broken down into its real and imaginary components to distinguish between resistive and capacitive components, and then fitted to a representative model circuit where the number, arrangement, and magnitude of the elements are chosen to reproduce the impedance spectrum of the device. Cole-Cole analysis shows that the complex impedance $Z = Z' + jZ''$, where $j = \sqrt{-1}$, may be plotted in a complex plane with its real part in the x-axis and the imaginary part in the y-axis. In the plot of imaginary part of impedance *verses* its real part, the diameter of the semicircle corresponds to resistance (*R*). A metal insulator semiconductor (MIS) device can be modeled using an equivalent circuit shown in Figure 2.14.

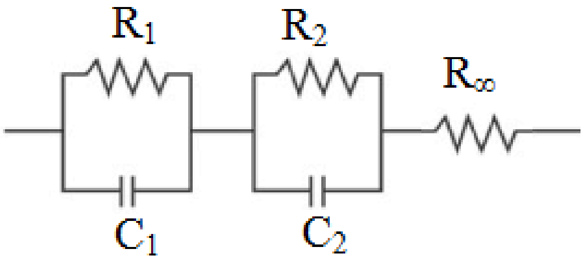

Figure 2.14: An equivalent circuit as model for an MIS device.

The complex impedance of the equivalent circuit is given by $Z = R_\infty + \frac{R_1}{1+j\omega R_1 C_1} + \frac{R_2}{1+j\omega R_2 C_2}$. In the case of ITO/PEDOT:PSS/polymer:fullerene/Al solar cell, R_∞ represents the resistance of Al, ITO and PEDOT:PSS. R_1 and C_1 corresponds to the resistance and capacitance of the interface between PEDOT:PSS/polymer:fullerene and polymer:fullerene/Al. R_2 and C_2 corresponds to the resistance and capacitance of polymer:fullerene active layer respectively.

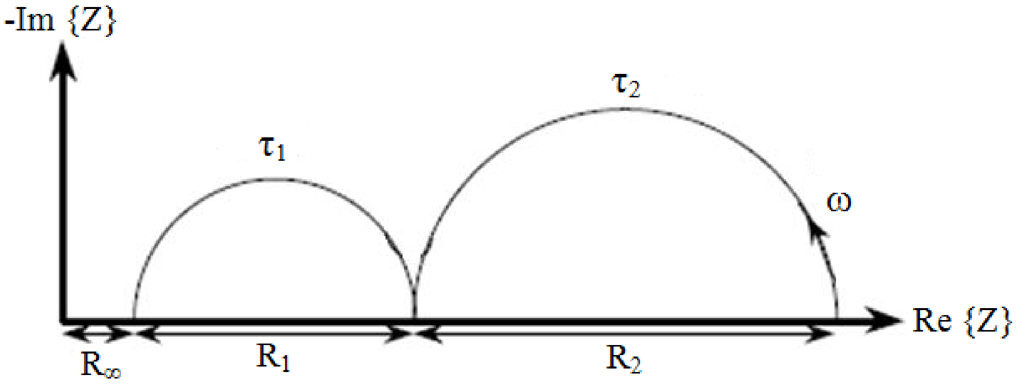

Figure 2.15: Idealized Cole-Cole plot for the circuit shown in Figure 2.14.

3. Experimental details

3.1. Materials and solutions

Regioregular poly(3-hexylthiophene) (P3HT) polymer used in this work was obtained from Rieke Specialty Polymers, Rieke Metals Inc.. The fullerene acceptors, [6,6]-phenyl-C_{61}-butyric acid methyl ester ($PC_{61}BM$) > 99.5% purity was obtained from Sigma-Aldrich, indene-C_{60} bisadduct (ICBA) from Lumtec Luminescence Technology Corp and [6,6]-Phenyl-C_{71}-butyric acid methyl ester ($PC_{71}BM$) M114, 99% purity from Ossila. All chemicals were used as received. The hole transporting polymer PEDOT:PSS was obtained from Abs. H. C. Starck. 1, 2-dichlorobenzene (Sigma-Aldrich 99 %) was used as a solvent.

The donor polymer poly[N-9'-hepta-decanyl-2,7-carbazole-alt-5,5-(4',7'-di-2-thienyl-2',1',3'-benzothiadiazole)] (PCDTBT) (average Mw 2.0×10^4 - 1.0×10^5) used in this work was obtained from Sigma-Aldrich. For experiment on PCDTBT, the fullerene acceptors, [6,6]-phenyl-C_{61}-butyric acid methyl ester ($PC_{61}BM$), > 99 % purity and [6,6]-Phenyl-C_{71}-butyric acid methyl ester ($PC_{71}BM$) > 99 %, mixture of isomers purity were obtained from Sigma-Aldrich. All chemicals were used as received. For devices fabricated at Addis Ababa University, Chemistry department laboratory, the hole transporting polymer PEDOT:PSS was obtained from Sigma-Aldrich. 1, 2-dichlorobenzene (Riedel-de Haen) was used as a solvent. The molecular structure of P3HT and PCDTBT is shown in Figure 3.1 whereas the molecular structure of acceptor fullerene derivatives ICBA, $PC_{61}BM$ and $PC_{71}BM$ is shown in Figure 3.2.

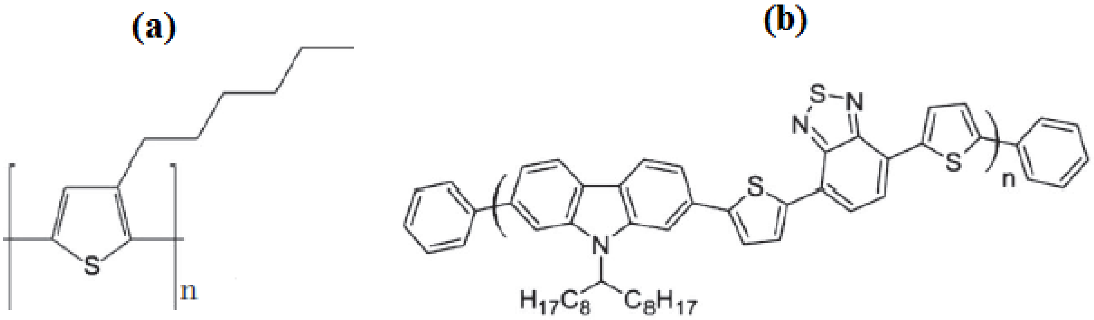

Figure 3.1: The chemical structure of donor polymers used in this work (a) P3HT, (b) PCDTBT.

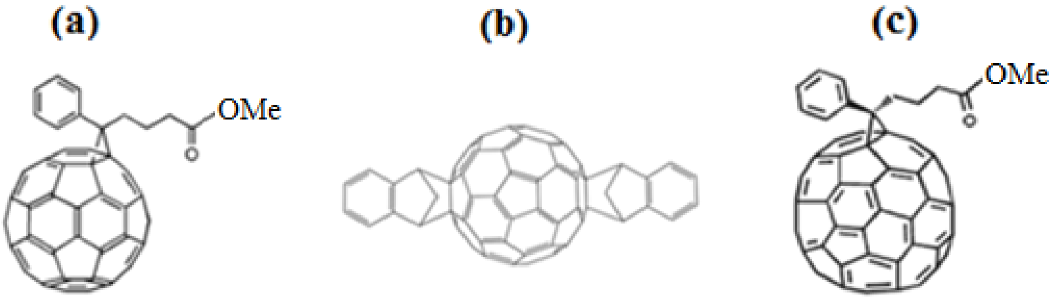

Figure 3.2: The chemical structure of fullerene derivatives used in this work (a) $PC_{61}BM$ (b) ICBA and (c) $PC_{71}BM$.

3.2. Device fabrication

Figure 3.3 below shows the general conventional geometry device structure of polymer-fullerene based solar cells.

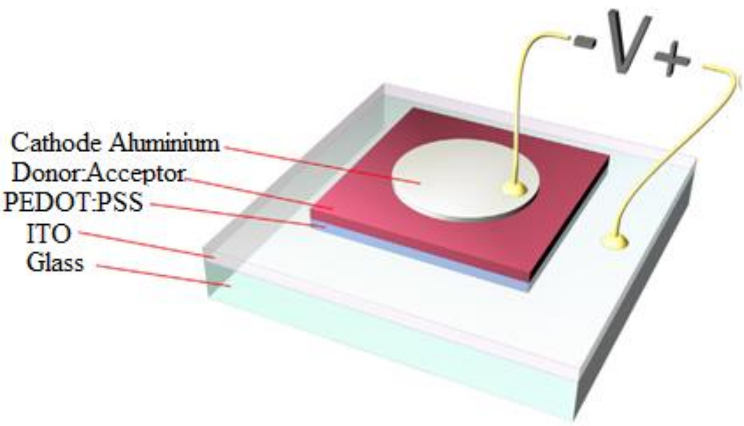

Figure 3.3: Device structure of ITO/PEDOT:PSS/Polymer:Fullerene/Al solar cell.

3.2.1. ITO cleaning

The devices were fabricated on indium tin oxide (ITO) coated glass substrate with a sheet resistance of 15 Ω/cm^2. ITO (2.5 mm x 2.5 mm) was partly protected with photoresist and the exposed ITO was etched with a mixture of HCl + HNO_3 + H_2O, 48:4:48 by volume. The etched portion of the ITO/glass provides a convenient region for the aluminum contact pads subsequently deposited. The photoresist was removed using acetone and then the surface was cleaned using a standard cleaning procedure consisting of a sequence of four ultrasonication steps in detergent, distilled water, acetone and isopropanol for 15 min each. After rinsing in deionized water and blowing them dry with nitrogen, the ITO coated substrates were treated by oxygen plasma for 3 min. However, for the devices fabricated in Addis Ababa University, Chemistry Department laboratory oxygen plasma treatments were not used.

3.2.2. PEDOT:PSS spin coating

The aqueous PEDOT:PSS dispersion was spin-coated onto the cleaned ITO coated substrates at 3000 rpm for 40 s to produce a film thickness of around 30 nm. The PEDOT:PSS coated substrates were dried on a hotplate at 150^{o}C for 15 min to remove water residues. Then the samples were directly transferred into the glove-box system, for spin-coating films of P3HT blends with different fullerene. However, for the devices fabricated in Addis Ababa University, Chemistry department laboratory spin-coated PEDOT:PSS film were kept on air until spin coating of the active layer.

3.2.3. Fabrication of P3HT:Fullerene solar cells

Prior to device fabrication, a solution consisting of P3HT:Fullerene in blend ratio of 1:1 (w/w%) and blend concentration of 30 mg/mL in 1, 2-dichlorobenzene (DCB) was stirred at 40^{o}C for 36 hr inside glove-box. P3HT:Fullerene solution spin-casted onto a PEDOT:PSS coated substrate at 800 rpm for 50 seconds inside glove-box. Finally through shadow mask 100 nm thick aluminum contacts were vacuum evaporated at a pressure of approximately 2 x 10^{-6} Torr. After aluminum evaporation the devices were annealed at 140^{o}C for 30 min inside glove-box. The sandwich structure ITO/PEDOT:PSS/P3HT:Fullerene/Al provides a means for current-voltage measurements. The structure of the device used in this work is shown in Figure 3.3.

3.2.4. Fabrication of P3HT:Fullerene/TiO$_x$ based solar cells

To study the effect of sol-gel processed TiO$_x$ interfacial layer on the performance and stability of P3HT:ICBA solar cells over a period of time under light irradiation, P3HT:ICBA solar cells is fabricated with a structure of ITO/PEDOT:PSS/P3HT:ICBA/TiO$_x$/Al according to the following procedure. The weight ratio for an active solution of P3HT:ICBA is 1:1 (wt/wt%) with a blend concentration of 30 mg/mL in DCB. The blend of P3HT:ICBA was spin-casted on top of the PEDOT:PSS layer at 800 rpm for 50 s. Then, the TiO_x precursor solution (diluted 1:200 in isopropyl alcohol) was spin-casted in air on top of the P3HT:ICBA film and heated at 80°C for 10 min in air. During this process the precursor converted to a solid TiO_x layer by hydrolysis. Then, 100 nm thick Al electrode was deposited by thermal evaporation in a vacuum of about ~2 x 10^{-6} Torr. The deposited Al electrode area defined the active area of the devices as 26 mm^2. Thermal annealing of the completed device without TiO_x layer was carried out by directly placing the completed devices on a hot plate at 140°C for 30 min in a glove-box filled with nitrogen gas.

3.2.5. Fabrication of PCDTBT:Fullerene solar cells

Prior to device fabrication, a solution consisting of PCDTBT:Fullerene in blend ratio of 1:4 (w/w%) and blend concentration of 22.5 mg/mL in 1, 2-dichlorobenzene was stirred for 36 hr. For mixture of $PC_{61}BM$ and $PC_{71}BM$ 1:1 (w/w%) ratio is used. PCDTBT:Fullerene solution spin-casted onto a PEDOT:PSS coated substrate at 1400 rpm for 54 s. Finally through shadow mask 100 nm thick Al electrod were vacuum evaporated using thermal evaporator (EDWARDs 306) at a pressure of approximately 4 x 10^{-6} Torr.

3.3. Device characterization

3.3.1. Device characterization of P3HT:Fullerene solar cells

The thickness of PEDOT:PSS and P3HT:Fullerene film were measured using Alpha-Step 500 Surface Profiler. To characterize the polymer solar cell, the current-voltage characteristics were measured by using Agilent Technologies B1550A Semiconductor Device analyzer. The set-up was controlled by the easyExpert software package. *J-V* characteristics of the P3HT:Fullerene based polymer solar cell were obtained in ambient air and room temperature under dark and white light illumination at 100 mW/cm^2 using AM1.5G ABET TECHNOLOGIES Sun 2000 Solar Simulator immediately after removing the sample from the glove-box. For degradation measurements in ambient air, the samples were kept in an open sample holder, exposed to simulated AM1.5G irradiation from a Solar Simulator of intensity 100 mW/cm^2. The photovoltaic cell characteristics: the power conversion efficiency (PCE), short-circuit current density (J_{sc}), open-circuit voltage (V_{oc}) and fill factor (*FF*) were measured at different irradiation time. The laboratory relative humidity during the *J-V* measurement was between 30% and 40%. All devices were not sealed. UV-visible absorption spectra were measured by Perkin Elmer Lambda 35 UV/Vis spectrometer. For this measurement blends were spin-coated onto glass substrates using the same conditions as those of the devices.

FTIR spectra of P3HT, PCBM, ICBA and their blends were recorded in transmission mode at the SISSI beamline of Elettra-Sincrotrone Trieste with a Bruker Vertex70 interferometer using a deuterium tryglycine sulfate (DTGS) detector. Spectra were obtained averaging 512 scans with 4 cm^{-1} spectral resolution. Samples were prepared by spin coating the test materials onto 1mm thick CaF_2 IR windows, having a very thin nanometric layer of sputterd silicon layer on the top. The silicon layer does not affect the IR transparency of the IR substrate while improves the wettability by the solution and the adhesion of the polymer and the blends on it. The samples have been measured immediately after preparation; the photodegradation test was made by exposure to simulated AM1.5G irradiation from a solar simulator of intensity 100 mW/cm^2 for 2 hr and by further exposure for 16 hr.

3.3.2. Device characterization of PCDTBT:Fullerene solar cells

To characterize the polymer solar cell, the current-voltage characteristics were measured by using an electrochemical analyzer (Model CHI600A) under white light illumination of 100 mW⁄cm^2 from a 150 W xenon lamp of Oriel type light source (Model 68830). All device preparation and characterization processes were done in open air.

For degradation measurements in ambient air, the samples were kept in an open sample holder, exposed to white light illumination of intensity 100 mW/cm^2. The photovoltaic cell characteristics: PCE, J_{sc}, V_{oc} and FF were measured at different irradiation time. All devices were not sealed. UV-visible absorption spectra were measured by UV-Vis Spectrometer Perkin Elmer Lambda 950 UV/VIS/NIR spectrometer from the 300 to 900 nm wavelength range. For UV-visible measurement blends were spin-coated onto glass substrates using the same conditions as those of the devices.

4. Results and Discussions

4.1. Investigation of Photodegradation in Polymer Solar Cells blended with different Fullerenes Derivatives

4.1.1. Background

Bulk heterojunction (BHJ) polymer solar cells having active layers comprising blended organic semiconducting polymers and fullerenes offer the advantage of low fabrication cost, lightness, simple solution-based device fabrication process and flexibility [10, 64, 154]. For polymer solar cells, over 12% power conversion efficiencies (PCEs) [31, 64, 65, 88, 155] have been reported and in the near future polymer solar cells fulfilling some of the requirements of commercial applications can be envisaged. Despite the growing efficiency of polymer based solar cells, their short working lifetime remains an obstacle to their practical use owing to chemical and physical degradation mechanisms when the device is exposed to oxygen, moisture, light and high temperature [23, 24, 29, 67 - 71]. In order to realize polymer based solar cells for practical use, it is imperative to investigate the stability of the polymer and polymer based solar cells under different working conditions.

In many papers it is reported that polymer BHJ films can be easily degraded and destroyed through various pathways of physical and chemical degradation [28, 29, 69 - 71]. On the other hand, Hoke et al. [100] based on their experiments concluded that the fullerene acceptors donate photogenerated electrons to oxygen molecule and result in the formation of superoxide radical anion O_2^-, which degrades the polymer. According to the authors, the fullerenes with low electron affinity are prone to easily donate photoexcited electrons to oxygen molecule.

In this study, the goal is to elucidate the effect of fullerene with different electron affinity on the air stability of P3HT based polymer solar cells. The fullerenes used as electron acceptor are ICBA and PCBM. ICBA has lower electron affinity than PCBM. Both acceptors are widely used for the fabrication of polymer solar cells. To compare the air stability of the active layer and solar cell fabricated from P3HT and the two fullerene acceptors, we used spectroscopic and electrical measurement techniques.

4.1.2. UV-visible absorbance measurement

Figure 4.1.1 (a) shows the time profile of UV-visible absorbance of P3HT film when irradiated with 100 mW/cm^2 light intensity at ambient air. Pure P3HT film shows a broad absorption band indicative of an extensive π-electron delocalization. The film shows a peak at 517 nm and two shoulders at 550 nm and 600 nm. The UV-visible absorbance has contributions from both inter-chain and intra-chain states, with the lowest energy feature in the π-π∗ region of the absorption spectrum at about 600 nm being associated with an inter-chain absorption of the regioregular P3HT film [156, 157]. When P3HT film is exposed to the irradiating light at ambient air the intensity of the peak at 517 nm and the two shoulders decreases continuously, which is indicative of photodegradation of the polymer due to exposure to air and light. Tromholt et al. [158] showed that UV-visible absorbance measurement at different time give valuable information on the stability of polymers.

In order to identify the effect of different fullerenes on the photobleaching of P3HT, films of P3HT:ICBA and P3HT:PCBM were aged by light illumination at 100 mW/cm^2 at ambient air and their absorption spectra were measured at different time. Figure 4.1.1 (b) and (c) show the time evolution of P3HT:ICBA and P3HT:PCBM film absorption when the film is irradiated at different time in ambient air condition. Absorbance of P3HT:ICBA and P3HT:PCBM film decreases with irradiation time at ambient air and this indicates the poor light stability of P3HT even in the presence of the fullerene. However, the comparison of Figure 4.1.1 (a) with Figure 4.1.1 (b) and (c) reveals that fullerenes stabilizes the P3HT slowing down its photodegradation. This effect is more pronounced in the case of PCBM rather than ICBA blended to P3HT.

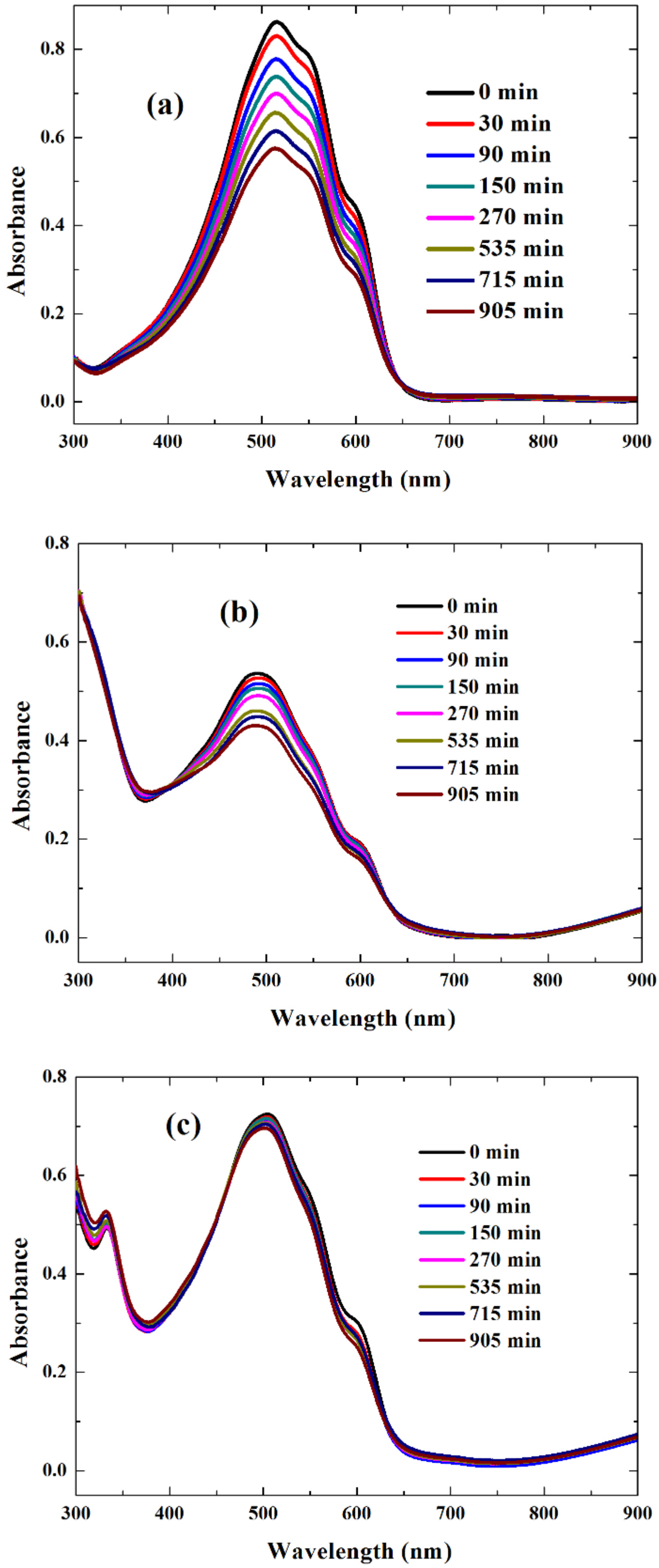

Figure 4.1.1: Change in the UV-visible absorbance of (a) P3HT, (b) P3HT:ICBA and (c) P3HT:PCBM film when irradiated at ambient air with 100 mW/cm^2 light at different time.

Figure 4.1.2 shows the absorbance of P3HT, P3HT:ICBA and P3HT:PCBM film normalized to their initial value as a function of irradiation time in ambient air. As shown in Figure 4.1.2, the intensity of the absorption band at 517 nm of P3HT film decreases continuously. For P3HT mixed with either ICBA or PCBM, the intensity of the absorption band at 490 nm for P3HT:ICBA and 505 nm for P3HT:PCBM films decrease more slowly compared to pure P3HT film. Simple inspection of Figure 4.1.2 shows that P3HT mixed with ICBA or PCBM has improved air stability relative to the pure film of P3HT.

Studying the P3HT products of photodegradation in ambient air by IR and UV spectroscopy, Manceau et al. [25] clearly demonstrated that P3HT oxidation involves the radical oxidation of the hexyl side chains and the subsequent degradation of the thiophene rings. As stated by the authors carbon atom at α-position to the thiophene ring is the preferential site for a radical attack. Breaking of thiophene ring results in a loss of π-conjugation and bleaching of P3HT film with the lowering of UV-visible absorbance.

Hoke et al. [100] experimentally showed that photoexcited electrons on the polymer and fullerene have contribution for the photodegradation of polymer. According to the proposed mechanism, photogenerated electrons on the polymer or fullerene can be transferred to diatomic oxygen forming the superoxide radical anion, O_2^-, which initiates the degradation of the polymer. Hoke et al. [100] also found out that in addition to the direct transfer of electrons from polymer to molecular oxygen, fullerene derivatives with low electron affinity are susceptible to transfer the photogenerated electrons to molecular oxygen, leading to the formation of the superoxide radical anion, which degrades the polymer.

The results of time dependent UV-visible absorbance study of the different films obviously indicate that mixing of P3HT with both ICBA and PCBM reduces the rate of P3HT photodegradation/oxidation. It has been suggested that photodegradation of the P3HT is initiated by the excited state of P3HT and the inclusion of PCBM stabilizes P3HT by quenching the reactive excited states of P3HT on sub-ps time scales and by this means slows the photodegradation of P3HT [100, 159 - 161]. Polymer exciton quenching by electron transfer to PCBM reduces the lifetime of the excited singlet state and thus reduces the population of all reaction inducing states that are populated *via* the singlet manifold [162]. Experimentally Distler et al. [162] has shown that in P3HT:PCBM blends, PCBM is expected to stabilize P3HT by screening it from the incident light. The optical screening effect of PCBM in the blend (the “inner filter effect”) seems to contribute < 30% to the observed reduction of the degradation rate of P3HT. In addition, radical scavenging properties of fullerene could contribute to the stability of P3HT [114, 163].

Figure 4.1.2 reveals that the photodegradation of P3HT has different rate depending on the type of fullerene blended with the polymer. The P3HT:ICBA blend has the highest photodegradation rate compared to P3HT:PCBM blend when irradiated at ambient air. The result is also in agreement with the finding of Hoke et al. [100], where low electron affinity fullerene derivatives contribute less to polymer stability. Superoxide radical anions have been shown to form by electron transfer from fullerene anions to molecular oxygen [164]. The increasing degradation rate of a series of polymers in blends with fullerenes of decreasing electron affinity has been interpreted as a result of enhanced formation of superoxide anions *via* the fullerene anions [100]. ICBA has lower electron affinity than PCBM. Based on our results we can conclude that in comparison with PCBM, ICBA is less efficient at quenching excited stated of P3HT or scavenging radical species, or is responsible for the opening of new degradation mechanisms. The observations from UV-visible studies show that care has to be taken when we choose different fullerenes as acceptor materials in P3HT based solar cells. The obtained result is very essential in the attempt to fabricate air stable polymer solar cells in general, and P3HT based solar cells in particular.

The better stabilization of P3HT polymer by PCBM has an essential role in increasing the lifetime of solar cells made from P3HT and PCBM. In order to test the stability of P3HT when blended with fullerenes, solar cell were fabricated from the blend of P3HT:ICBA and P3HT:PCBM and their stability in air under irradiation in terms of photovoltaic performance were compared.

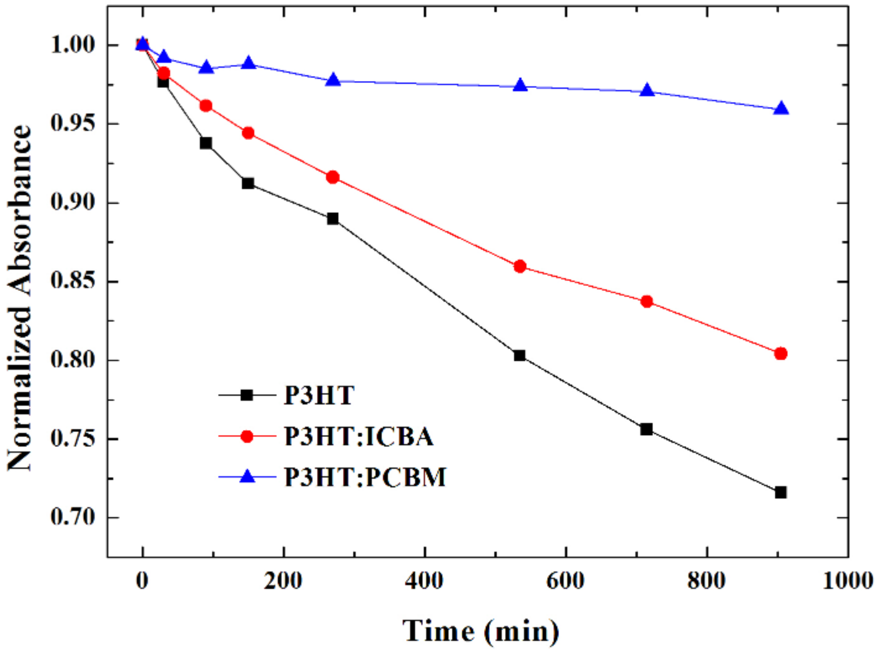

Figure 4.1.2: Normalized UV-visible absorbance of P3HT (at 517 nm), P3HT:ICBA (at 490 nm) and P3HT:PCBM (at 505 nm) film as a function of irradiation (100 mW/cm^2 light) time at ambient air.

4.1.3. Fourier transform infrared (FTIR) spectroscopy

In order to evaluate the chemical modifications induced by solar irradiation (AM 1.5 G, 100 mW/cm^2) on P3HT blended with both PCBM and ICBA, FTIR spectroscopy of blends and their pure constituents at different irradiation time has been performed in the range from 3100 to 800 cm^{-1}. The FTIR spectrum of P3HT shows the typical vibrational bands of P3HT polymer, as well as spectral modification related to photodegradation in air according to data reported in the literature [25, 102, 165].

In the 3100 - 2700 cm^{-1} spectral region (Figure 4.1.3A) methyl and methylene stretching bands from the hexyl side chain of the thiophene ring can be seen, centred at 2954 cm^{-1} (asym), 2871 cm^{-1} (sym) and 2925 cm^{-1} (asym), 2856 cm^{-1} (sym) while the thiophene ring C$_\beta$-H stretching vibration is at 3054 cm^{-1}. Thiophene ring, C-H in-plane bending were detected at 820 cm^{-1}. The absorption peak around 1376 cm^{-1} was contributed by the methyl deformation. Upon 18 hr of exposure to sun simulator light, a decrease in the intensities of the aliphatic C-H stretching bands can be seen, while intensity variations were barely detectable for the heteroaromatic C-H moiety. The involvement of =C-H group in the polymer degradation process can be better appreciated from the decrease of the in-plane bending mode centered at 820 cm^{-1} (Figure 4.1.3D). According to what previously highlighted, the intensity of the methyl symmetrical bending centered at 1376 cm^{-1} also decreases after 18 hr irradiation (Figure 4.1.3D). In the 1600 - 1400 cm^{-1} (Figure 4.1.3C), ring stretching modes of thiophene are detected at 1562 cm^{-1}, 1509 cm^{-1} and 1454 cm^{-1}, the latter one overlapped with deformation modes of methyl and methylene groups. The intensity of all these bands drops upon irradiation, while a shoulder at 1415 cm^{-1} appears, possibly related to changes in the ring substitution.

Table 4.1.1: Assignments of the main IR positions of pristine P3HT thin film [25, 166].

Wave number [cm^{-1}]	Assignment
3054	Thiophene ring C-H stretching
2954	Asym. side chain CH_3 stretching
2925	Asym. side chain CH_2 stretching
2871	Sym. side chain CH_3 stretching
2856	Sym. side chain CH_2 stretching
1562	C=C ring stretching
1509	Thiophene ring, asym. C=C stretching
1454	Thiophene ring, sym. C=C stretching
1376	CH_3 symmetrical bending
820	Thiophene ring, C-H in-plane bending

The most relevant spectral features of P3HT photodegradation products can be seen in the spectral regions 1900 - 1600 and 1400 - 800 cm^{-1} (Figs. 4.1.3B and 4.1.3D, respectively). Spectral bands related to carbonyl functions, such as ester, anhydrides, aliphatic and aromatic ketons can be seen in the Figure 4.1.3B, which show a marked increase of intensity as a function of irradiation time. Since hydroxyl stretching modes were not detected between 3700 - 3500 cm^{-1} (data not shown) carboxylic end-products can be excluded at this degradation stage. Vibrational modes related to oxidized sulphur species are below 1400 cm^{-1}, and several rising bands can be seen in the 1400 - 800 cm^{-1} spectral region after 2 and 18 hr of 100 mW/cm^2 light irradiation.

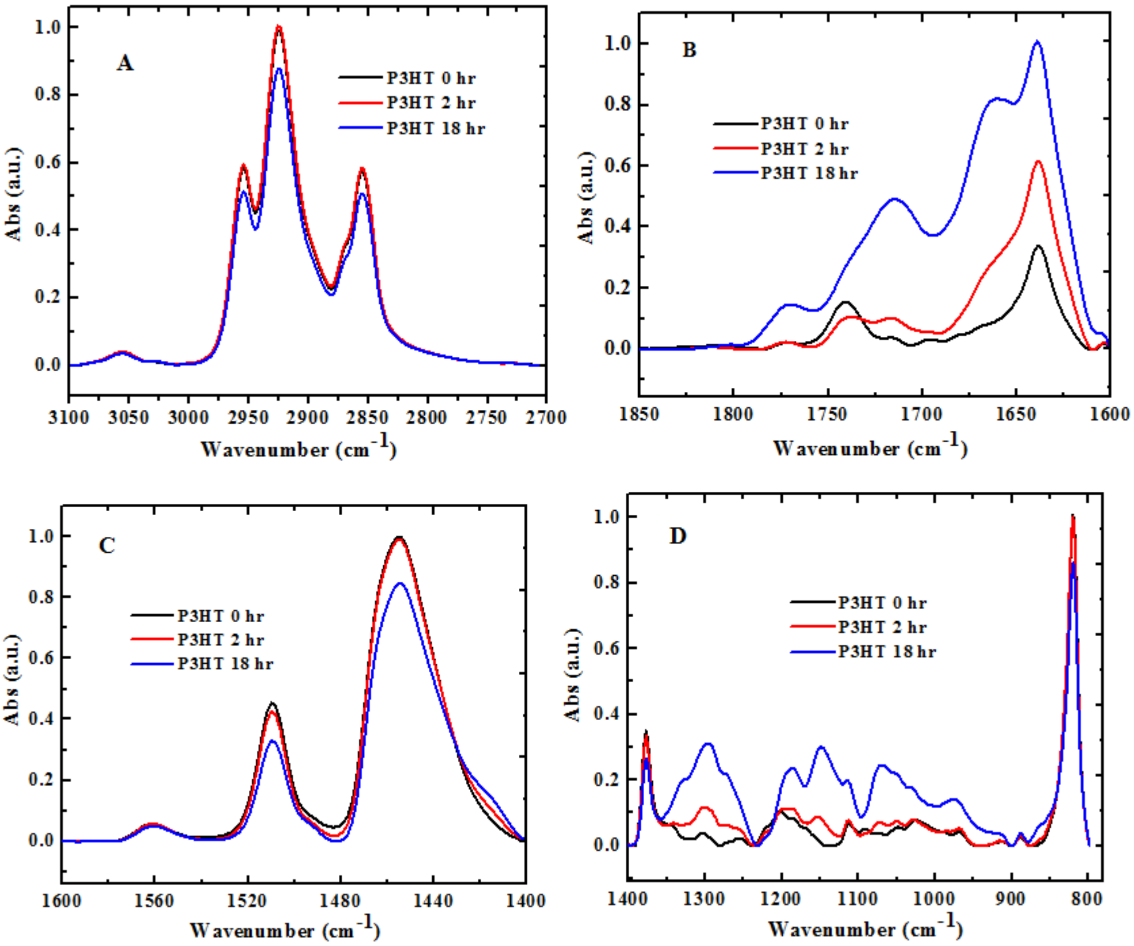

Figure 4.1.3: FTIR spectroscopy of the pristine and irradiated P3HT in different spectral regions exhibiting the signature of photodegradation mechanisms.

In Figure 4.1.4A and 4.1.4B, extensive photodegradation of ICBA can be detected by FTIR spectroscopy. Stretching bands of –C-H moieties of indene-C_{60} bis-adduct decrease upon irradiation (AM 1.5 G, 100 mW/cm^2 light) in the 3100 - 2700 cm^{-1} spectral region, revealing an implication of the functional groups of fullerene cage in ICBA degradation (Figure 4.1.4A). In accordance with data reported by Chambon et al. [114], we found that irradiation induced the appearance of two well-resolved spectral bands centered at 1782 and 1745 cm^{-1} within the first two exposure hours, related to the oxidation of the C_{60} cage (Figure 4.1.4B).

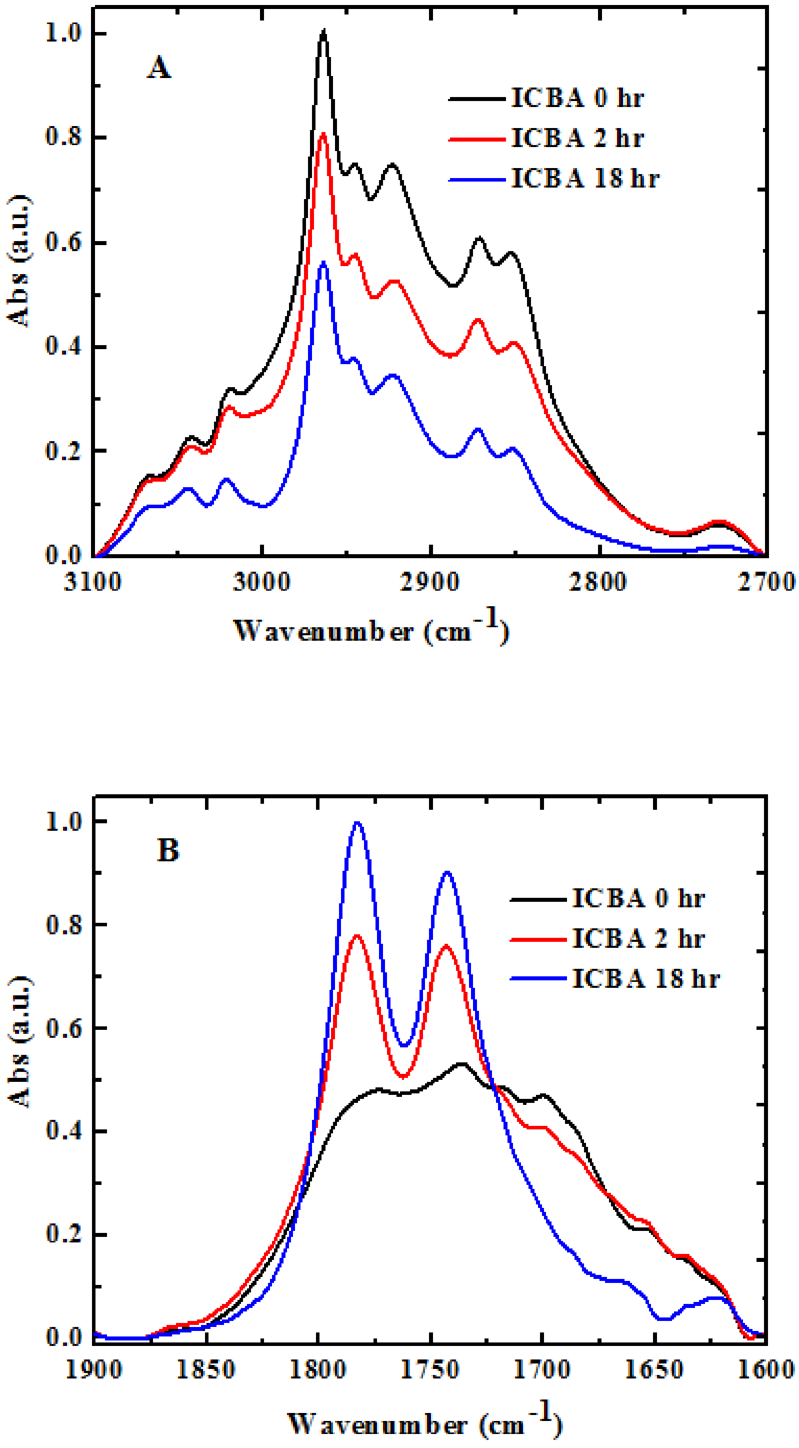

Figure 4.1.4: FTIR spectroscopy of the pristine and irradiated ICBA in different spectral regions.

Figure 4.1.5 shows the FTIR spectra of the pristine and irradiated PCBM in different spectral regions. Unlike that of ICBA, PCBM spectra do not show detectable signatures of photodegradation after 18 hr of light irradiation. The result obtained reveals the photostability of PCBM after 18 hr of light irradiation in ambient air. The obtained result is interesting because photostability of acceptor material is among the factors which affect device performance and stability of polymer solar cells.

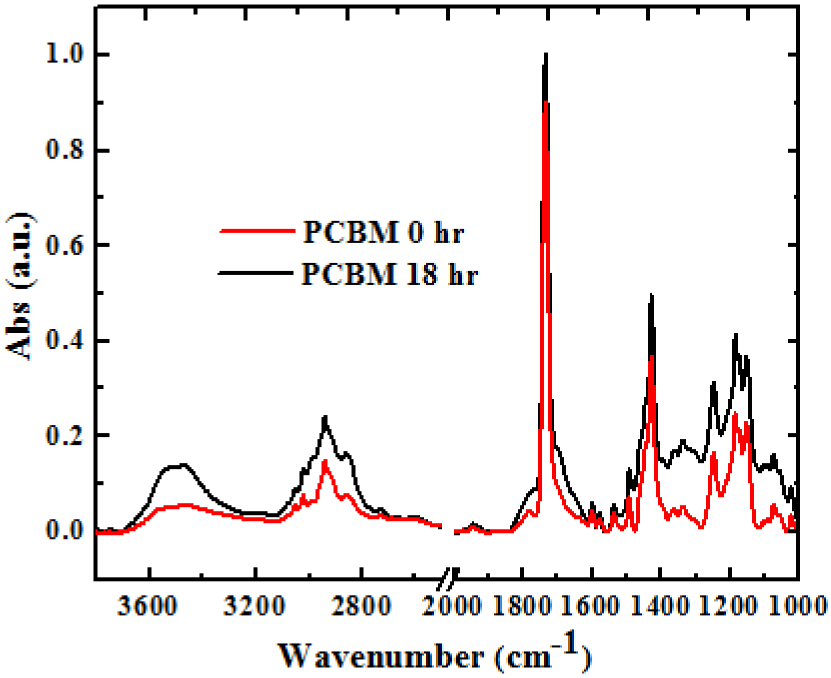

Figure 4.1.5: FTIR spectroscopy of the pristine and irradiated PCBM in different spectral regions.

FTIR spectroscopy reveals also remarkable spectral changes of the P3HT:ICBA blend, related to oxidation of both donor and acceptor. In the region 3100 - 2700 cm^{-1}, the intensity variations of C-H stretching bands characteristic of P3HT can be seen (Figure 4.1.6A), while the carbonyl stretching spectral interval between 1900 and 1600 cm^{-1} shows a complex pattern of spectral bands possibly related to both P3HT and ICBA degradation products (Figure 4.1.6B). In the spectral regions 1600 - 1400 cm^{-1} and 1400 - 1000 cm^{-1}, the spectroscopic features related to the modifications of the thiophene ring and the generation of oxidized sulphur species can be recognized (Figure 4.1.6C and 4.1.6D).

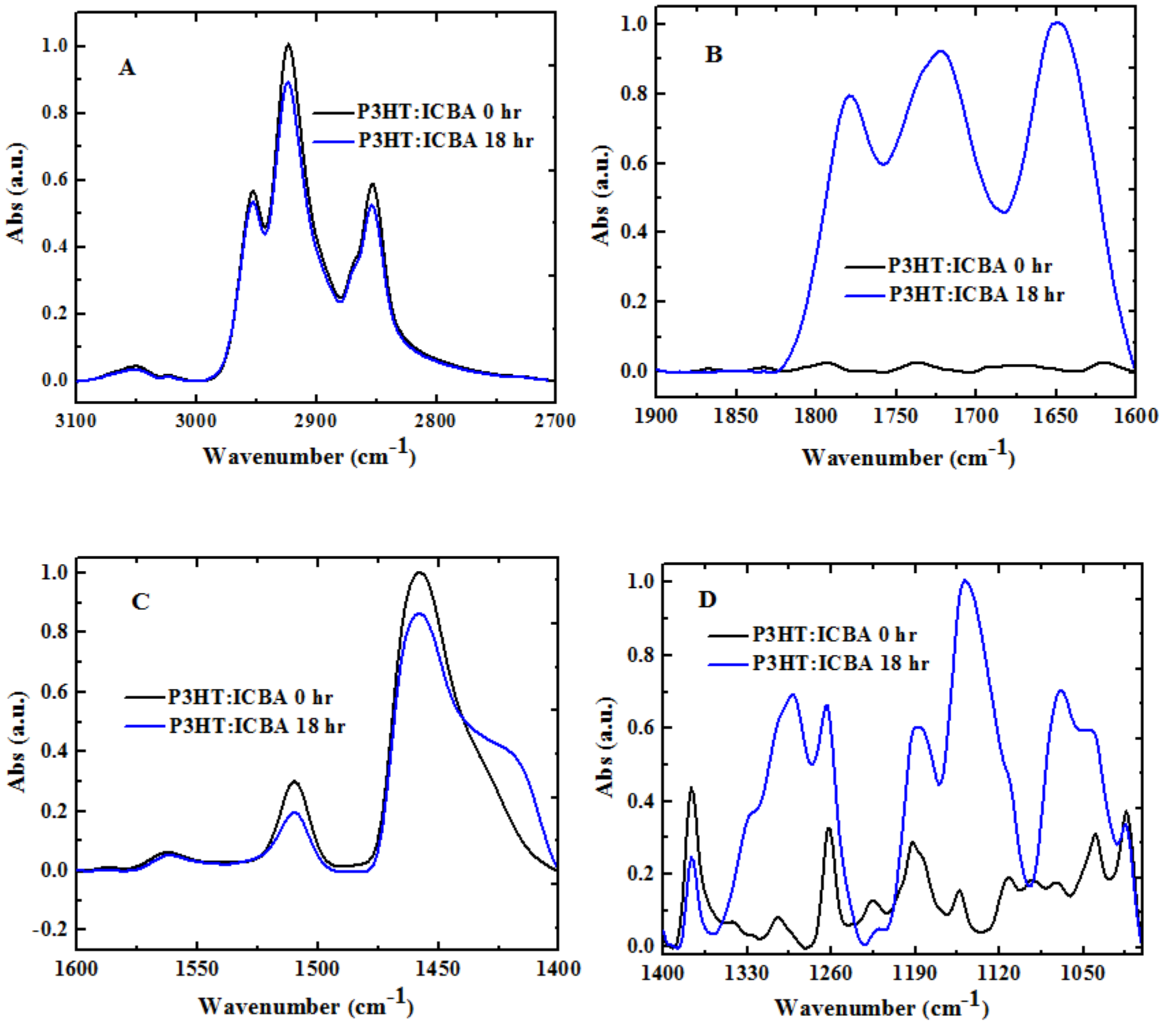

Figure 4.1.6: FTIR spectroscopy of the pristine and irradiated blend P3HT:ICBA in different spectral regions exhibiting the signature of photodegradation mechanisms.

In Figure 4.1.7 the spectra of P3HT:PCBM blend does not show detectable signatures of photodegradation after 18 hr of irradiation of the film with 100 mW/cm^2 light intensity at ambient air. Interestingly, the P3HT:PCBM blend does not show spectroscopic changes, neither related to PCBM degradation, nor to P3HT, revealing that PCBM confers major stability to the P3HT, accordingly to UV-visible absorbance data.

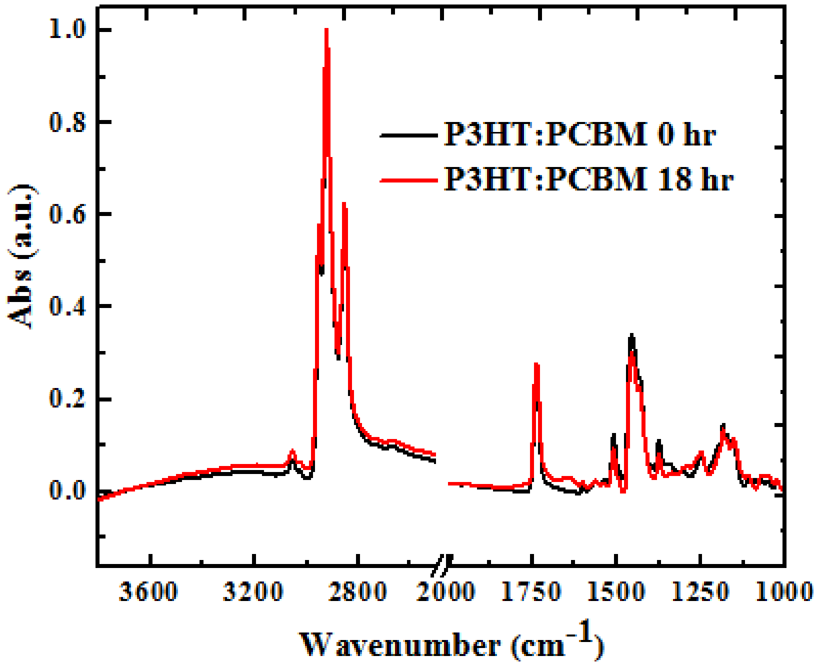

Figure 4.1.7: FTIR spectroscopy of the pristine and irradiated blend P3HT:PCBM in different spectral regions.

4.1.4. Current-voltage characteristics in the dark

Under forward bias, the diode dark current is mainly shaped by recombination. Real diodes have limited charge injection efficiency due to charge trapping and recombination effects. The slope of the dark *J*-*V* characteristic above the turn-on voltage depends on two parameters: the diode ideality factor (n) and the reverse saturation current [88, 167]. As shown in Figure 4.1.8 with increasing ageing time the exponentiality of the diode dark current decreased, indicating that the formation of the trap state reduced the “quality” of P3HT:ICBA and P3HT:PCBM diode. However, in comparison the decrease of exponentiality of the diode dark current is higher for P3HT:ICBA diode. For P3HT:ICBA diode n = 1.8, whereas for P3HT:PCBM diode it is 1.5. The diode ideality factor is higher for P3HT:ICBA device. Higher values of the diode ideality factor have been associated with increased recombination loss or increased disorder in the electronic states [168 - 170]. Recombination through surface or interface states can lead to deviations of the ‘ideal’ ideality factor from n = 1 to the non-ideal case (n > 1) [171]. Thus, the higher diode ideality factor can be attributed to an increase in interfacial trap-assisted trapping and recombination due to the formation of recombination centers as a result of photodegradation of P3HT and fullerene or increased electronic disorder in the BHJ [168, 169, 172].

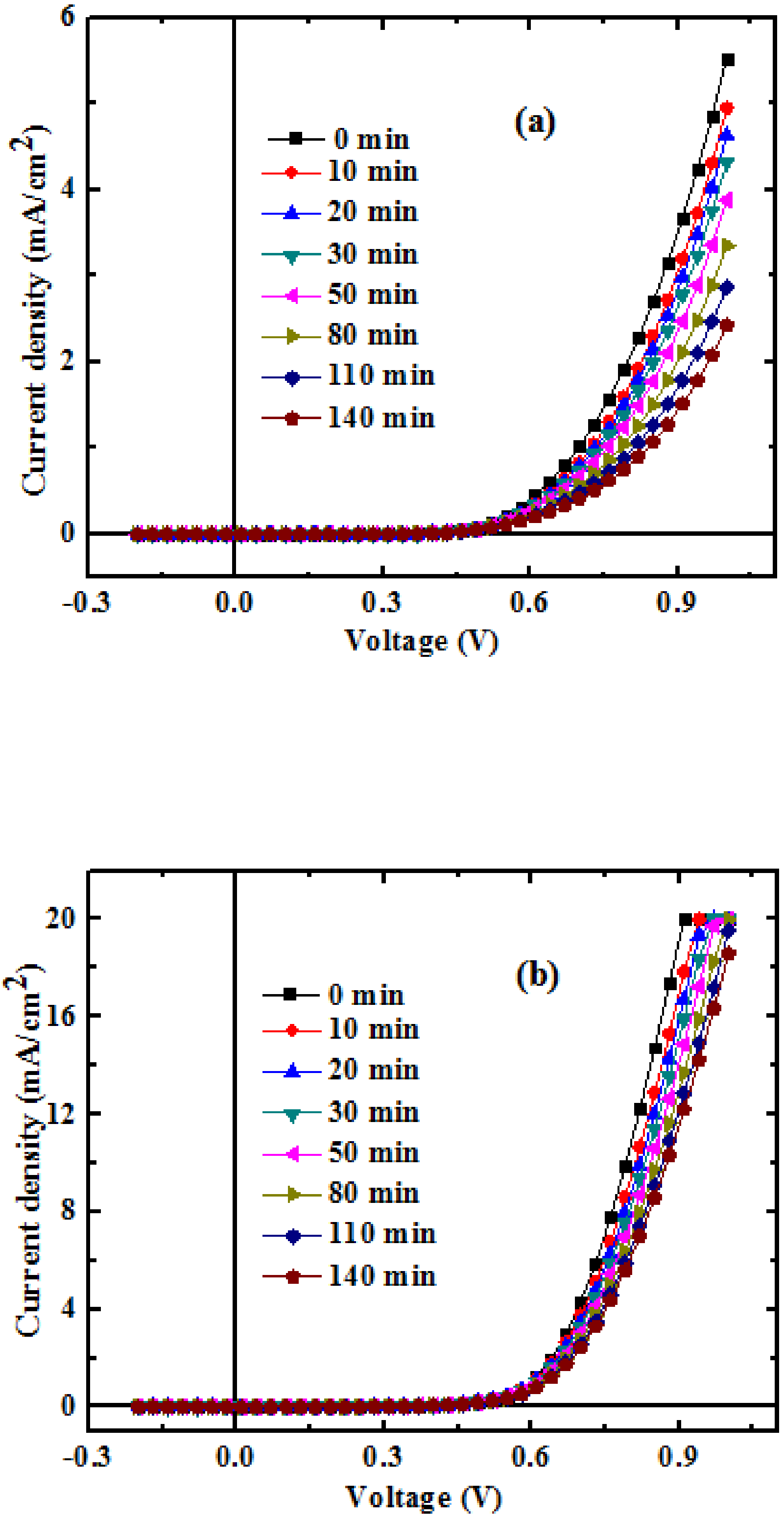

Figure 4.1.8: Dark current density *versus* voltage in the dark for (a) P3HT:ICBA and (b) P3HT:PCBM BHJ solar cell devices aged at ambient air with irradiation of 100 mW/cm^2 light.

Figure 4.1.9 below shows the variation of normalized series resistances (R_s) of P3HT:ICBA and P3HT:PCBM solar cells as a function of irradiation (100 mW/cm^2 light) time at ambient air. From Figure 4.1.9 it is obvious that with increasing irradiation time, the series resistance of the device based on P3HT:ICBA blend increased continuously, however the value for the device based on P3HT:PCBM active layer is relatively constant.

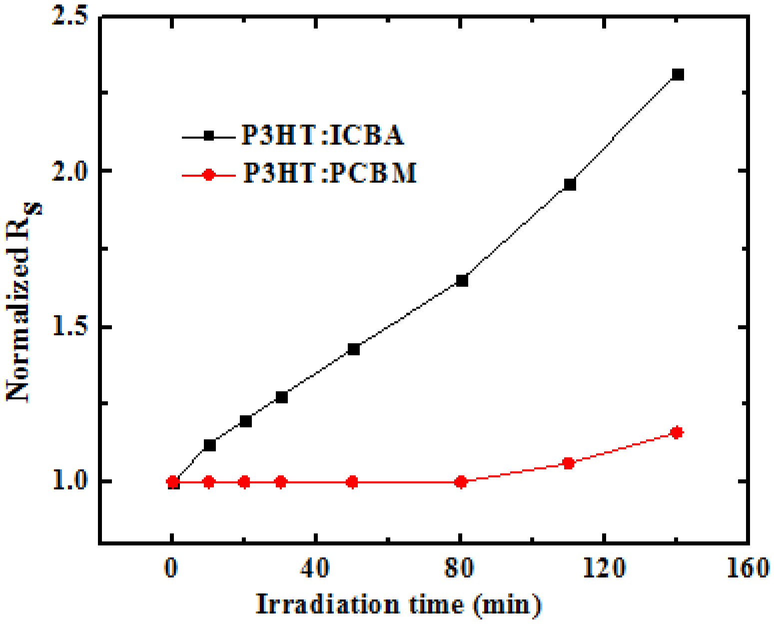

Figure 4.1.9: Normalized series resistances (R_s) of P3HT:ICBA and P3HT:PCBM solar cells as a function of irradiation (100 mW/cm^2 light) time at ambient air.

4.1.5. Photovoltaic measurement

Measurement of current-voltage characteristics of a solar cell allows the calculation of its photovoltaic performance and electrical response. The ambient air stability of the solar cells made from P3HT and different fullerene derivatives acceptors were conducted at room temperature by irradiating the device with 100 mW/cm^2 light for a total time of 140 min. Figure 4.1.10 (a) and (b) show the current density-voltage (J-V) curves of non encapsulated bulk heterojunction solar cell made from P3HT:ICBA and P3HT:PCBM and aged at ambient air under device irradiation. The protocol used in the characterization of the photodegradation of PSCs complies with the test protocol ISOS-L-2, with the single exception that the measurements in our case were carried out at room temperature and not in the range 65 - 85°C as from the prescription [173].

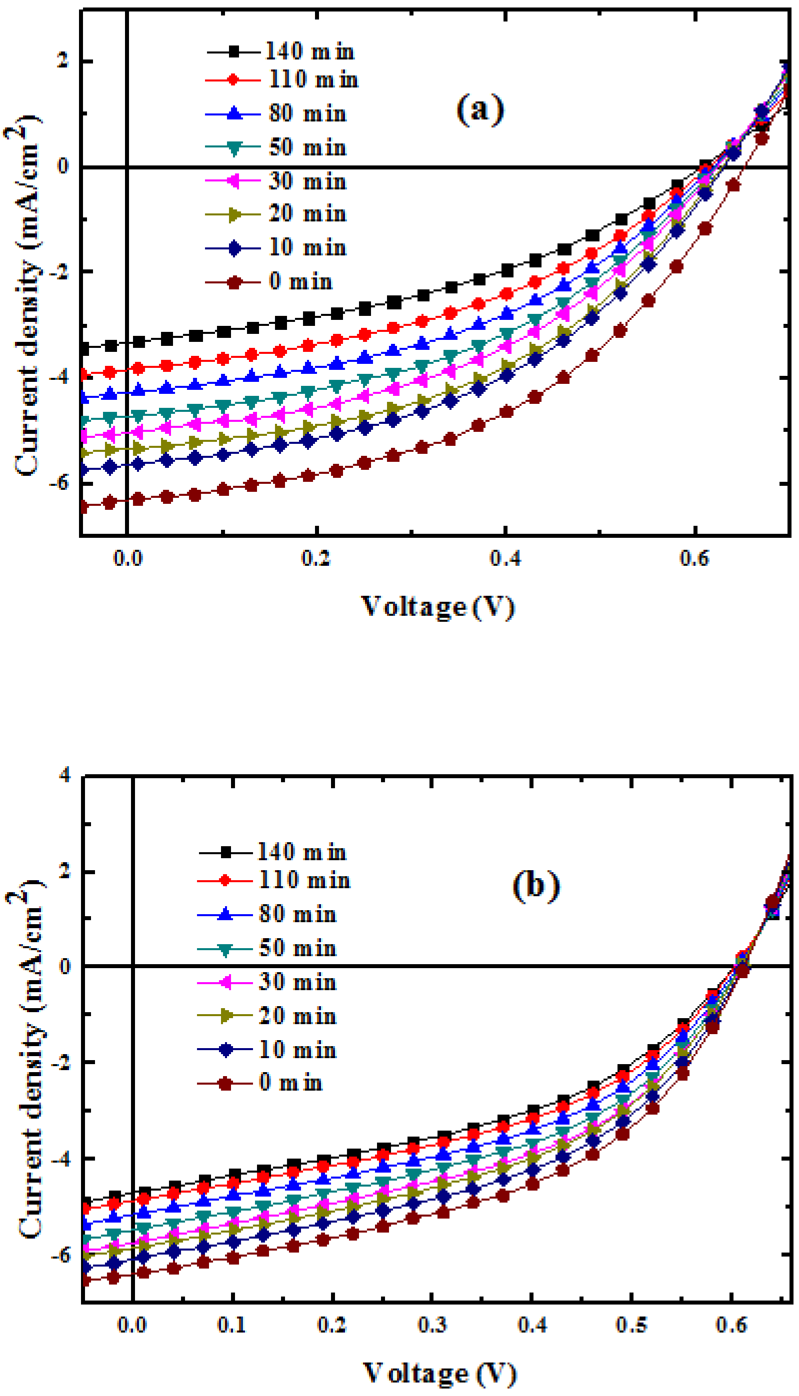

Figure 4.1.10: Current density-voltage (*J*-*V*) curves of bulk heterojunction solar cell made from (a) P3HT:ICBA and (b) P3HT:PCBM and aged at ambient air with irradiation of 100 mW/cm^2 light.

Figure 4.1.11 shows the decay of normalized efficiency and short-circuit current of devices with a P3HT:ICBA and P3HT:PCBM as a function of time during irradiation with 100 mW/cm^2 light at ambient air and Figure 4.1.12 shows the concomitant decay of normalized open-circuit voltage and fill factor in the same devices. Normalization was done relative to their initial values.

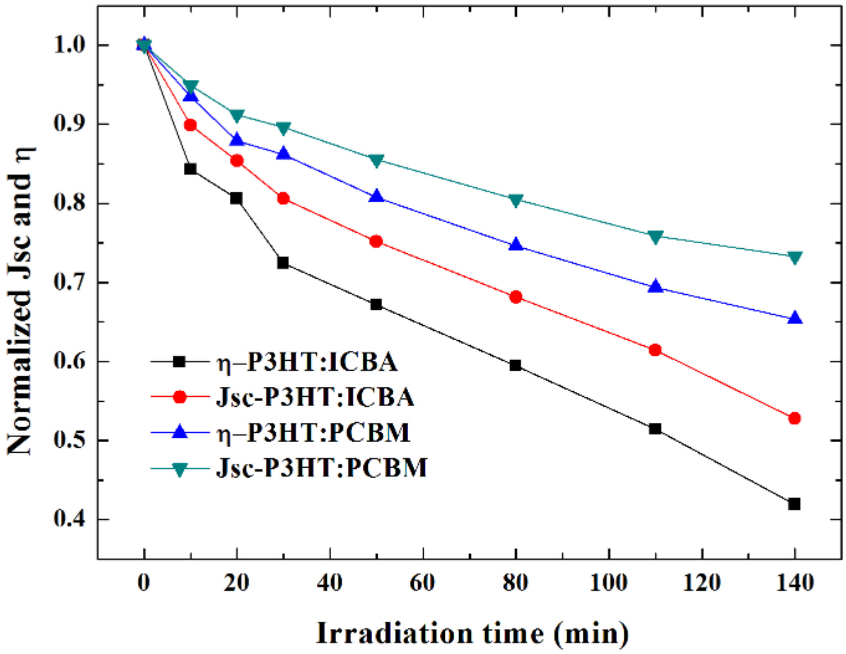

Figure 4.1.11: Normalized efficiency (*η*) and short circuit current-density (J_{sc}) of P3HT:ICBA and P3HT:PCBM solar cell as a function of irradiation (100 mW/cm^2) time at ambient air.

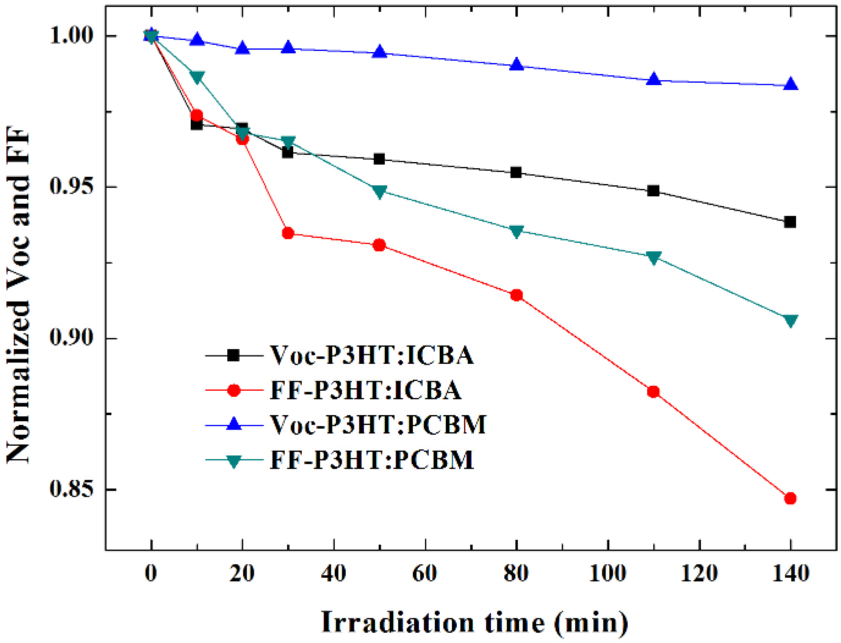

Figure 4.1.12: Normalized open-circuit voltage (V_{oc}) and fill factor (*FF*) of P3HT:ICBA and P3HT:PCBM solar cell as a function of irradiation (100 mW/cm^2 light) time at ambient air.

In identifying and studying degradation mechanisms taking place in organic solar cells, valuable information can be extracted by monitoring efficiency (η), short-circuit current density (J_{sc}), open-circuit voltage (V_{oc}) and fill factor (*FF*) as a function of time under accelerated aging conditions. Accelerated aging was done by exposure of the solar cell to light (100 mW/cm^2) for pre-determined time at ambient air with no device encapsulation.

After 140 min of device irradiation, the P3HT:ICBA based bulk heterojunction solar cell showed a 58.3% relative decrease in efficiency and, in absolute from 1.87% to 0.78%. On the other hand, P3HT:PCBM based solar cell displayed a 34.8% relative decrease in efficiency, from 1.81% to 1.18%. The obtained results show that a stronger decrease in efficiency was seen for solar cells with ICBA as acceptor. Since both devices were fabricated and characterized in the same conditions, the only reason for the different degradation rate of the two devices consisted in the type of fullerene used as acceptor. In literatures, it is reported that mixing of P3HT with different fullerene derivatives slows down the photobleaching of P3HT and in conjugated polymers in general [174 - 176]. Our experimental results show that there is variation among fullerene derivatives in their contribution to the P3HT stability under the described aging conditions. By UV-visible and FTIR absorbance measurements we showed that by mixing of P3HT with fullerene derivatives the photodegradation of P3HT is slowed down. Nevertheless, UV-visible, FTIR and J-V characterization prove consistently that ICBA has inferior stabilizing effect on P3HT against degradation compared to PCBM.

Figure 4.1.11 and Figure 4.1.12 indicate that reduced J_{sc} and *FF* of P3HT:ICBA and P3HT:PCBM BHJ devices are mainly responsible for the decrease in the device efficiency. The P3HT:ICBA BHJ device short-circuit current density sharply decreased after 140 min of the air stability test from 6.3 to 3.3 mA/cm^2 which is greater than the corresponding decrease for the P3HT:PCBM BHJ device, namely from 6.4 to 4.7 mA/cm^2. Generally, a decrease of the current density collected at the electrodes can be ascribed to different causes, namely, a decrease in photon absorption, charge dissociation, charge transport to the electrodes and charge collection [92].

In our particular experiment on P3HT:ICBA and P3HT:PCBM the main cause for the decline of short circuit current density is related to the bleaching of the photoactive layer, due to the rupture of the thiophene rings, as evidenced by UV-visible and FTIR characterization in section 4.1.2 and 4.1.3 respectively. The physical degradation of the active layer leads to the formation of additional trap levels that enhance charge carriers recombination and ultimately results in lower values of J_{sc} and *FF* [177]. Both blends exhibit a reduction under aging conditions of J_{sc} and *FF*. However, in P3HT:PCBM device, the J_{sc} reduces at less than half rate in P3HT:ICBA.

Measurement of *FF* as a function of irradiation time provides information about the evolution of the interfaces between the active layer and the electrodes, charge transport through the active layer and charge extraction in organic solar cell [92]. In the P3HT:ICBA BHJ device *FF* decreased from 46.27 to 39.2% (i.e. 15.3% relative decrease), which exceeds the corresponding decreases for the P3HT:PCBM BHJ device, from 46.32 to 42.0%, (i.e. 9.3% relative decrease). Therefore, by comparing the *FF* of the two devices, it appears that oxidative degradation by exposure to light in ambient air causes more damage to photovoltaic devices made from P3HT:ICBA blend.

The open-circuit voltage of organic solar cells is determined by the energy difference between the highest occupied molecular orbital (HOMO) of the electron donor and the lowest unoccupied molecular orbital (LUMO) of electron acceptor material. Therefore, any change in the HOMO level of the donor and/or LUMO level of the acceptor reflects into a change of V_{oc}. As shown in Figure 4.1.12, for the P3HT:PCBM device, V_{oc} remained almost constant during the aging experiment (ΔV_{oc} = -9.93 mV after 140 min), while that of P3HT:ICBA device exhibited a fast reduction of V_{oc} at the beginning of the aging (ΔV_{oc} = -24.89 mV in the first 30 min), followed by a slow decline (ΔV_{oc} = -14.82 mV in the next 110 min).

Therefore, the question is, how could we explain the reduction of V_{oc} with aging? In fact the value of V_{oc} is linked to the energy levels in the material and not to the transport properties. In addition to oxidation of polymer, a possible mechanism explaining the decrease of V_{oc} can be found in the oxidation of the fullerene cage. In fact by matrix-assisted laser desorption/ionization time-of-flight mass spectroscopy (MALDI-TOF), Reese et al. [159] provided a clear evidence, based on the detection of a series peaks equally spaced by 16 atomic units, that PCBM in a P3HT:PCBM blend aged in ambient conditions undergoes multiple oxidations, with up to eight oxygen atoms binding to each fullerene molecule. By Quantum chemical calculation the same authors found that the LUMO levels of PCBM oxids progressively goes down in energy as a function of the number of bound oxygen atoms. This is a sizable effect with a shift ΔE LUMO ~ -50 mV of the LUMO level per each oxygen atom binding to the fullerene cage. Therefore, by the effect of oxidation the fullerene component of the blend become heterogeneous, with fullerenes of different oxidation states and different LUMO levels.

As known from other studies [178], in ternary blends (polymer:fullerene A:fullerene B) it is known that V_{oc} exhibits a continuous dependence on the relative composition of the different fullerene species present in the active layer. In other words, in ternary blends V_{oc} is not necessarily pinned to the smallest V_{oc} of the corresponding binary polymer:fullerene blends. Analogously, in the present case where the fullerene component becomes heterogeneous due to its progressive oxidation, the presence of fullerenes with decreasing LUMO levels as a function of the aging time can explain the observed continuous decrease of V_{oc}. The fact that the change of V_{oc} is significantly higher for P3HT:ICBA than P3HT:PCBM, is related to the fact that ICBA easier to oxidize than PCBM [100]. In relative sense PCBM acceptor has better stable LUMO energy level.

Figure 4.1.13 shows the comparison of external quantum efficiency (EQE) of fresh and aged P3HT:ICBA and P3HT:PCBM solar cells. The devices were aged at ambient and indoor light for 30 days. Generally, the decrease of EQE is an indicative of the presence of degradation in solar cells [179]. For P3HT:ICBA the EQE of aged device significantly decreased over the entire wavelength range measured and the maximum EQE dropped from 66% at 500 nm to14.5% (78% relative reduction). The decrease in EQE between 300 and 700 nm can be assigned to the degradation of the P3HT:ICBA layer. In contrast, for P3HT:PCBM aged device shows change of EQE from 69% to 51% at 510 nm (26.4% relative reduction).

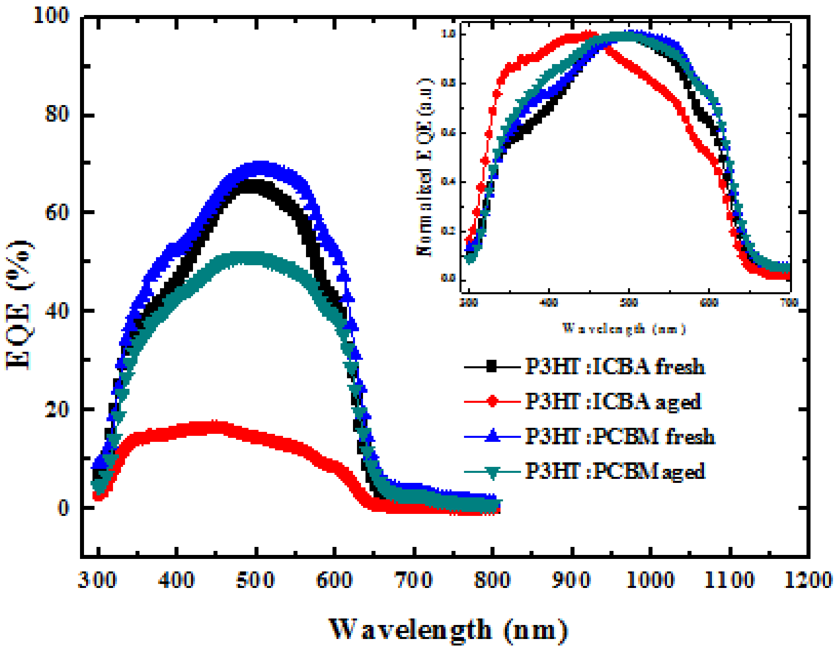

Figure 4.1.13: External quantum efficiency (EQE) measurement of fresh and aged devices. The devices were aged at ambient and indoor light for 30 days. The inset shows the normalized EQE for fresh and aged devices.

In the inset the same spectra are shown after being rescaled by a normalization factor, to fix the maximum EQE to 1 for each curve. The normalization of the aged P3HT:ICBA device EQE clearly shows that there is a considerable change in shape of spectrum especially in the 300 nm to 600 nm wavelength range. For P3HT:PCBM aged device there is insignificant change in shape of EQE spectrum in the wavelength range between 350 nm and 450 nm. Comparing the change in the shape of the EQE spectrum for P3HT:ICBA and P3HT:PCBM, reveals that there is significant change in case of P3HT:ICBA. The change in the shape of the EQE curve can be ascribed to the different degradation rate of the polymer and the fullerene components. In the case of the P3HT:ICBA solar cell, where the reduction of the overall cell efficiency was about three times larger than in the case of P3HT:PCBM, the faster degradation of the polymer leads to an increased relative weight of the fullerene contribution to the external quantum efficiency, concentrated in the 300 - 450 nm wavelength window.

4.1.6. Space charge limited current hole mobility measurement

Charge mobility is among the factors that significantly determine the performance of solar cell especially polymer solar cells. When polymer solar cell is exposed to air and light, the active layer undergoes photooxidation and the mobility of charges is affected. Thus, it is essential to determine the role of fullerene derivatives on charge mobility when the active layer is exposed to air and light. From the different methods available to measure charge carrier mobility, space-charge limited current (SCLC) from the analysis of current density-voltage (*J-V*) characteristics in the dark is easy and cost effective technique. A basic requirement for the observation of dark SCLC in a solid is a contact, which represents an infinite reservoir of carriers that can enter freely the solid (Ohmic contact) [140]. For single carrier SCLC measurement only one contact needs to be Ohmic [141, 180].

To quantify the effect of photodegradation on hole mobility in P3HT:ICBA and P3HT:PCBM solar cells, we used hole only devices with the following structures: ITO/PEDOT:PSS/P3HT:ICBA/Au and ITO/PEDOT:PSS/P3HT:PCBM/Au. The ITO/PEDOT:PSS anode forms Ohmic contact with HOMO level of P3HT. Since the work function of gold is 5.0 eV, it effectively prevents the injection of electrons into the film of P3HT:ICBA or P3HT:PCBM and the current transport is dominated by holes injection from ITO/PEDOT:PSS ohmic contact.

According to the theory of SCLC, at high applied voltage, when all traps are filled the injected charges are free to move and the current follows $J \sim V^2$ relation. The current density-voltage relationship is characterized by the trap-free-square law and it is given by Equation (18) in section 2.9. So, from Equation (18), by plotting *J versus* V^2, the value of hole mobility in P3HT:ICBA or P3HT:PCBM can be calculated. For both active layers, $\varepsilon_s = 4$ [77, 181], $\varepsilon_o = 8.854 \times 10^{-12}$ F/m, $d = 170$ nm were used and substituting these values in Equation (18) and a linear fit of *J versus* V^2 gives the value of hole mobility (μ).

The calculated hole mobility for as prepared P3HT:ICBA was about 1.54×10^{-4} cm^2/Vs which decreased to 1.24×10^{-4} cm^2/Vs upon 140 min ambient air illumination, corresponding to a 20% relative decrease in mobility. The hole mobility for as prepared P3HT:PCBM is 4.38×10^{-4} cm^2/Vs and after 140 min light irradiation is becomes 3.76 x

10^{-4} cm^2/Vs. For P3HT:PCBM, the hole mobility reduced by 14%. These results reveal that the ambient air light illumination reduces the hole mobility of P3HT in both active layers. The lower hole mobility could arise from chain stacking conformation of P3HT from high crystallinity to a lower crystallinity and also due to photo-induced degradation reaction on P3HT, where the product of photodegradation acts as charge trapping center [182]. However, the reduction of hole mobility is more visible in case of the active layer formed from P3HT:ICBA and this is possibly due to the higher photodegradation of P3HT in P3HT:ICBA active layer due to lower stabilizing effect of ICBA.

4.1.7. Conclusions

Two fullerene derivatives were used to fabricate polymer solar cell based on P3HT. The air stability of the solar cell fabricated from P3HT and the two fullerenes were characterized by spectroscopic and electrical measurement methods. Using UV-visible, FTIR and *J-V* measurement we have showed that the P3HT:PCBM film and solar cells fabricated from a P3HT:PCBM as active layer have much better air stability than those made from P3HT:ICBA as active layer. From spectroscopic and electrical measurements, we conclude that polymer solar cells with a P3HT:ICBA BHJ have much less air stability than polymer solar cells with P3HT:PCBM BHJ due to the accelerated physical and chemical degradation of the active layer. The photodegradation of P3HT results in reduced light absorption, increased series resistance and lower hole mobility. The consistency between the two independent spectroscopic and electrical measurements shows the validity of the photodegradation results. Therefore, to produce polymer solar cells with better air stability, PCBM as acceptor is more promising than ICBA. The advantage of the former is due to its more stabilizing ability of P3HT film, but the mechanism of better stabilization by PCBM needs further investigation.

4.2. Stability and Photovoltaic Performance Improvement of P3HT:ICBA Solar Cells Using TiO_x Interfacial Layer

4.2.1. Background

Many research has been carried out and still going on the use of P3HT:PCBM as active material in polymer solar cells [59]. However, PCBM is not an ideal acceptor material because of its low absorption coefficient in the visible regions [183] and relatively large offset of the energy levels with most donor materials [184]. Due to higher electron affinity, PCBM limits the open-circuit voltage of the P3HT-based polymer solar cell to about 600 mV [59, 183, 185]. There are two ways to improve V_{oc} of PSC. One approach is design and synthesis of low-band gap polymers and the other method is development of new electron acceptor materials with high lying LUMO level. ICBA has been developed with the aim of improving acceptor materials for polymer solar cells. Based on the accepted equation of open-circuit voltage, electron acceptors with lower electron affinity is expected to improve the V_{oc} because of the larger energy offset achievable between the donor HOMO and the acceptor LUMO energy level. ICBA has lower electron affinity than $PC_{61}BM$ [154, 183]. Compare to $PC_{61}BM$, ICBA has better absorbance and easily synthesized from C_{60} and indene [183, 186]. Because of its high power conversion efficiency due to higher open-circuit voltage, polymer solar cell made from P3HT and ICBA has attracted considerable research attention.

As experimentally known in section 4.1, despite the comparatively higher PCE, the lifetime of P3HT:ICBA solar cell is much lower compared to P3HT:$PC_{61}BM$ based solar cells. In P3HT:ICBA solar cells, the photodegradation of the active layer is clearly related to exposure to oxygen, moisture and light [26, 27]. As we have seen in section 4.1.3, in addition to P3HT, ICBA is also contributing for the photodegradation of the device unlike that of $PC_{61}BM$. ICBA has both advantages and limitations to be used as acceptor material in polymer solar cells. Therefore, to make useable the better performance of P3HT:ICBA solar cells, there has to be some mechanism to improve the stability of the active layer based on P3HT and ICBA.

To fabricate polymer solar cells with stable working lifetime, either the development of improved barrier materials for packing or the development of devices with less air sensitivity is required. For example, Lee et al. [187] fabricated air stable PSCs by inserting a solution based titanium sub-oxide (TiO_x) interfacial layer between the active layer and the Al electrode. According to their finding and explanation, TiO_x layer served as an effective barrier for oxygen and water penetration and improved device lifetime in an ambient atmosphere. Many experimental findings show that TiO_x interfacial layer effectively minimize physical and chemical damages of the active layer and improves the device working lifetime [59, 188 - 193]. In this study, we synthesized TiO_x using sol-gel procedure and fabricated PSCs composed of P3HT:ICBA with the TiO_x layer and performed a stability test by aging the device with irradiation under ambient air. For synthesis of TiO_x using sol-gel process, the procedure used by Lee et al. [187] was followed.

4.2.2. UV-visible absorbance measurement

Figure 4.2.1 shows the UV-visible absorption spectra measured for P3HT:ICBA, P3HT and ICBA film. The UV-visible absorption spectra of pure P3HT show three peaks in the visible ranges of 520, 550 and 600 nm. These values were similar to the ones that have been reported earlier for regioregular P3HT [156, 157, 194]. The higher energy absorption bands at 550 and 520 nm have been considered to arise from the 0-0 transition and the 0-1 transition of an intra-chain exciton [195]. ICBA film exhibits absorption in both UV and visible regions (with maximum visible region absorption around 475 nm) and it is advantageous to enhance light harvesting and power conversion efficiency of solar cells made of ICBA as acceptor. With addition of ICBA the absorption of the P3HT film blue-shifted and the absorption maximum was at 490 nm. The shoulder at 550 nm disappeared and the other shoulder at 600 nm remained not affected. The interesting point about the shoulder at 600 nm is that its position is not affected by ICBA addition. While the maximum absorption peak is blue-shifted and the other shoulder is disappeared, the one at 600 nm does not appear to blue-shifted at all. This is a clear indication that the shoulder at 600 nm has a different physical origin than the other absorption shoulder and absorption maximum.

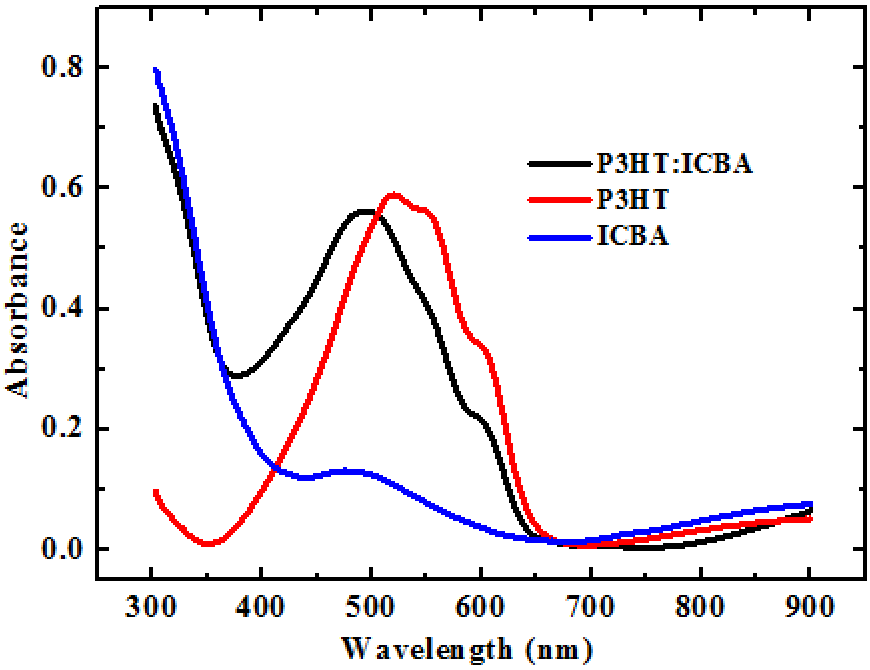

Figure 4.2.1: UV-visible absorption spectra of P3HT:ICBA, P3HT and ICBA films.

Figure 4.2.2 shows the UV-visible absorbance spectra of P3HT and P3HT:ICBA at room temperature (RT) and film of P3HT:ICBA annealed at 140°C for 20 min. At room temperature P3HT shows shoulder around 550 and 600 nm while at room temperature film of P3HT:ICBA has no shoulder which suggests no well-defined ordering of the P3HT due to the existence of ICBA molecule. Similar effects were seen for P3HT blended with $PC_{61}BM$ [89]. However, after annealing at 140°C for 20 min P3HT:ICBA showed a shoulder at 600 nm and the corresponding UV-visible spectrum shows a radical modification related to significant improvement of the P3HT:ICBA blend morphology. The shift of λ_{max} (from 464 to 490 nm), the increase of the absorbance (10% at λ_{max}) clearly indicates higher ordering of the P3HT packing.

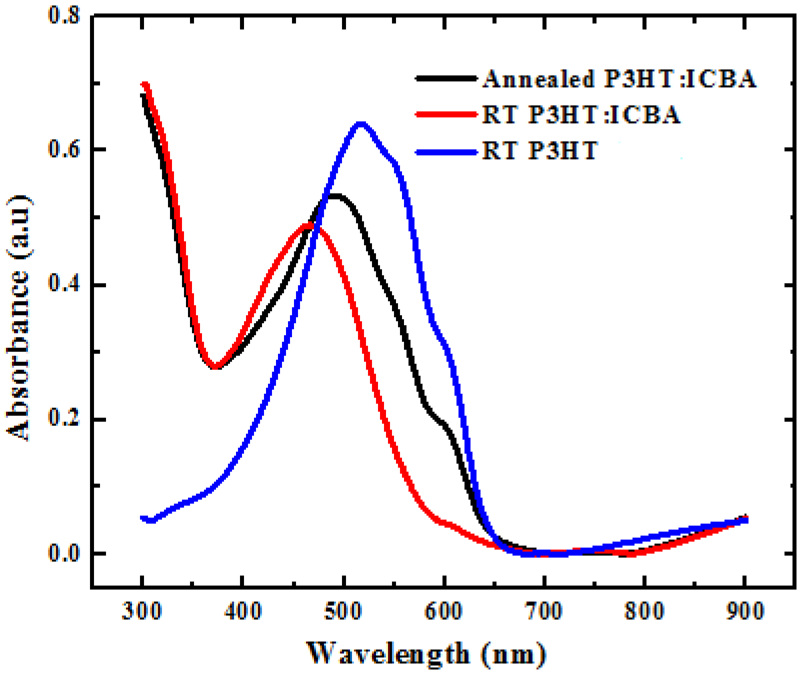

Figure 4.2.2: UV-visible absorption spectra of P3HT (RT), P3HT:ICBA (RT) and P3HT:ICBA annealed at 140°C for 20 min.

In polymer solar cells, TiO_x has been used as the optical spacer to optimize absorption within the active layer by redistributing the light intensity within the BHJ by changing the optical interference between the incident light and the light reflected from the metal electrode [189, 190, 196 - 198]. To investigate the effect of TiO_x interfacial layer on improving light absorption of P3HT:ICBA film, TiO_x solutions was spin-casted on top of P3HT:ICBA photoactive layer at different spin speeds of 1000 rpm, 2000 rpm, 3000 rpm, and 4000 rpm. The thicknesses of TiO_x layer prepared by spin speeds of 1000 rpm, 2000 rpm, 3000 rpm, and 4000 rpm were measured by Alpha-Step 500 Surface Profiler and their values were 30, 20, 12 and 4 nm, respectively. The spining speed that gave 12 nm TiO_x layer was selected for further study [59].

In order to investigate the effect of TiO_x layer on the photostability of P3HT:ICBA film we have measured UV-visible absorbance of P3HT:ICBA film at different time by aging the film with 100 mW/cm^2 light irradiation at ambient air. Figure 4.2.3 indicates that the photodegradation of P3HT:ICBA film has different rate with and without TiO_x layer. When irradiated at ambient air P3HT:ICBA film without TiO_x layer has the highest photodegradation rate compared to P3HT:ICBA film coated with TiO_x layer. The obtained evidence from UV-visible measurement shows that significant protection of P3HT:ICBA film from ambient air photodegradation is provided by the TiO_x layer coated on top of the film. The photobleaching of the active layer is attributed to photooxidation of P3HT:ICBA by oxygen and moisture present in the ambient air. The obtained result demonstrated the excellent air stability of P3HT:ICBA film coated with TiO_x layer.

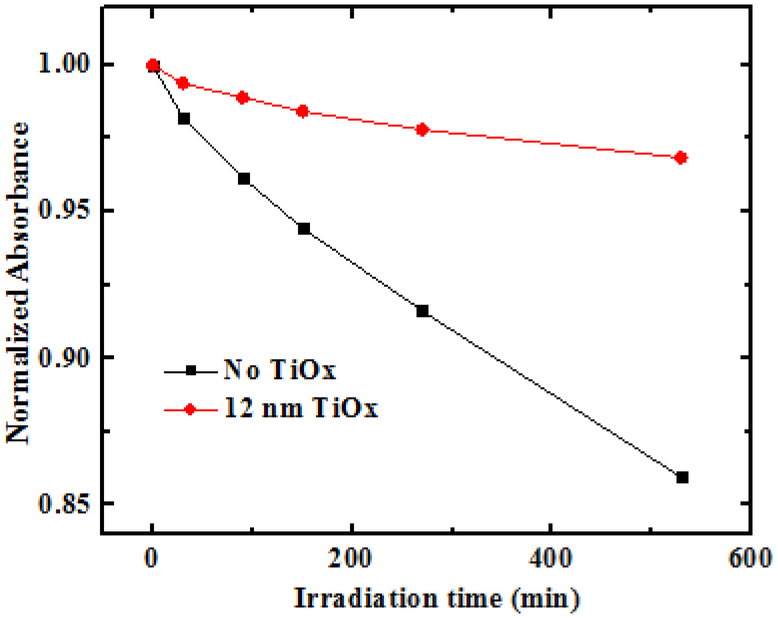

Figure 4.2.3: Normalized UV-visible absorbance of P3HT:ICBA (at 490 nm) without and with 12 nm TiO_x layer as a function of irradiation (100 mW/cm^2 light) time at ambient air.

Usually photodegradation of active layer is caused by the combination of light and atmospheric agents, with major roles of oxygen and water [26, 27, 92, 192, 199]. The damaging effects of oxygen and water under light irradiation is that electron transfer could occur from the photoexcited P3HT and ICBA to molecular oxygen, generating the superoxide radical anion, O_2^-, which is a very reactive anionic radical that attack P3HT and cause photooxidation and break P3HT conjugation and reduce the light absorption power of the polymer [159, 191, 200]. On its own water has a small effect on the photodegradation of active layer, however, it can accelerate the rate of photodegradation when oxygen is present. The reason is as follows. When there is water, oxygen becomes hydrated and hydrated forms of molecular oxygen are easier to reduce, because their electron affinity becomes larger and as a result the electron transfer from the photoexcited P3HT to molecular oxygen will be easier and faster [199, 201].

According to our result from UV-visible absorbance and FTIR measurements in section 4.1, both P3HT and ICBA are susceptible to photodegradation due to oxygen, moisture and light. Better air stability of P3HT:ICBA film coated with TiO_x layer shows that TiO_x layer acts as a shielding and scavenging layer which prevents the intrusion of oxygen and humidity into the electronically active P3HT:ICBA film. Oxygen/water vapor protection and scavenging capability of the TiO_x layer originates from the combination of photocatalysis and inherent oxygen deficiency [187]. Based on our UV-visible absorbance result the coating of TiO_x layer into the P3HT:ICBA film would seem to be a wise approach to lower the sensitivity of P3HT:ICBA active layer toward oxygen and water vapor. Therefore, TiO_x layer is expected to improve the lifetime of unpackaged P3HT:ICBA based polymer solar cells exposed to light at ambient air. In order to test the stability of P3HT:ICBA coated with TiO_x layer, solar cells were fabricated from the blend of P3HT:ICBA with and without TiO_x layer and their stability in air under 100 mW/cm^2 light irradiation were compared in terms of photovoltaic performance.

4.2.3. Photovoltaic measurement

In order to elucidate the function of the TiO_x layer on photovoltaic performance of P3HT:ICBA based solar cells, the real devices with and without the TiO_x layer have been fabricated using exactly the same procedures and under exactly the same conditions, except for the TiO_x interfacial layer deposition, thus the conclusions drawn on the effect of TiO_x interfacial layer are valid. Figure 4.2.4 compares the *J-V* characteristics of the P3HT:ICBA solar cell without and with 12 nm TiO_x layer obtained under simulated AM1.5G illumination from a Solar Simulator with irradiation intensity of 100 mW/cm^2. The device fabricated with a TiO_x layer obviously shows improved photovoltaic performance. The obtained result shows that the introduction of TiO_x between the active layer and cathode is a viable means for improving the performance of P3HT:ICBA solar cells. Generally, the use of TiO_x interfacial layer for improving performance of PSCs is reported in many literatures [189, 191, 202 - 205] and our result is consistent with them.

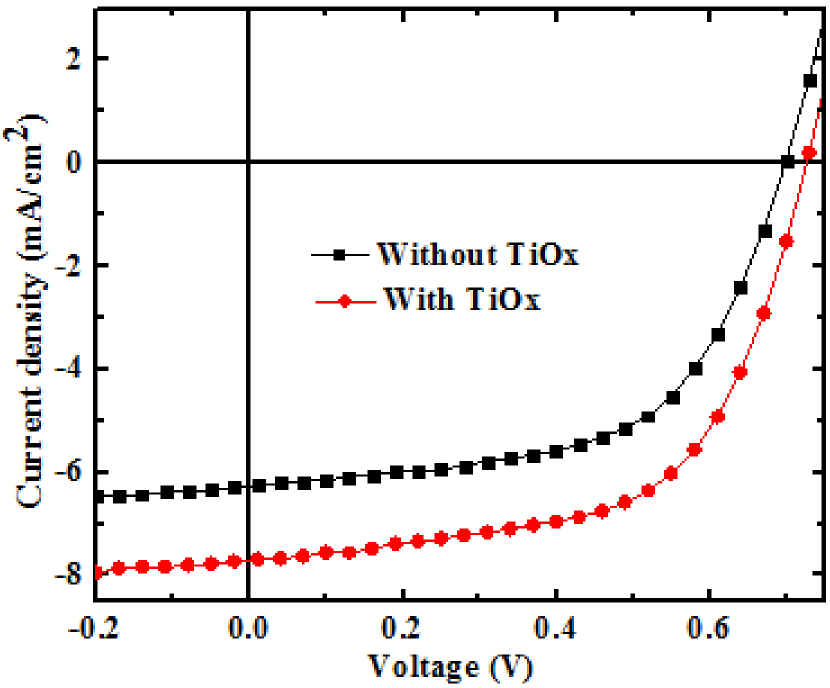

Figure 4.2.4: The current density-voltage (*J-V*) characteristics of the P3HT:ICBA based solar cells with and without TiO_x layer.

P3HT:ICBA solar cell without the TiO_x layer gave the following results: J_{sc} = 6.25 mA/cm^2, V_{oc} = 694 mV, *FF* = 49% and η = 2.12%. On the other hand, for P3HT:ICBA solar cell with the TiO_x layer the obtained results are: J_{sc} = 7.63 mA/cm^2, V_{oc} = 719 mV, and *FF* = 57% and η = 3.1%. For P3HT:ICBA solar cell with the TiO_x layer, the results show considerably improved photovoltaic performance compare to device without TiO_x layer. The increase in J_{sc} (22.1%) and *FF* (16.3%) is primarily responsible for the increase in the power conversion efficiency of TiO_x coated device.

The function of TiO_x as optical spacer has contribution for the higher J_{sc} for the device with TiO_x layer [189]. Because of its optical spacer effect TiO_x interfacial layer can redistribute the light intensity in the P3HT:ICBA film and as a result it enhanced the photon harvesting by P3HT:ICBA film. Open-circuit voltage is related with charge carrier recombination in the active layer [206]. Generally, interfacial layers form a barrier for carriers of one sort, and pass by the carriers of the opposite sort. Interfacial layers which act as an exciton blocking layer should have a bandgap higher that of the donor or acceptor of the active layer depending on the type of charge carrier we want to block. The transfer of excitons through the interfacial layer is not possible without a supply of additional energy. Therefore, an interfacial layer can act as an exciton blocking layer [207, 208]. In our case, due to large bandgap of 3.7 eV, TiO_x layer [189] enables or facilitates extraction of electrons, but blocks holes and excitons efficiently. TiO_x layer form selective contacts and prevent excitons and carriers created in the entire active layer from recombining at the electrodes. The function of TiO_x layer as electron transport layer (ETL) and hole blocking layer (HBL) can be explained based on the energy level diagram shown in Figure 4.2.5. Since the lowest unoccupied molecular orbital (LUMO) level of TiO_x (4.4 eV) is close to Fermi level of electron collecting Al electrode (4.3 eV) it could facilitate the electron transfer from ICBA (LUMO level: 3.67 eV) to Al. In contrast, the highest occupied molecular orbital (HOMO) level (8.1 eV) of TiO_x is larger than that of P3HT (5.2 eV), resulting in the prevention of the hole accumulation at the active layer-cathode (Al) interface, which leads to a more reduced interfacial charge recombination. As a result of reduced charge carrier recombination, open-circuit voltage is higher in a device where TiO_x layer was used.

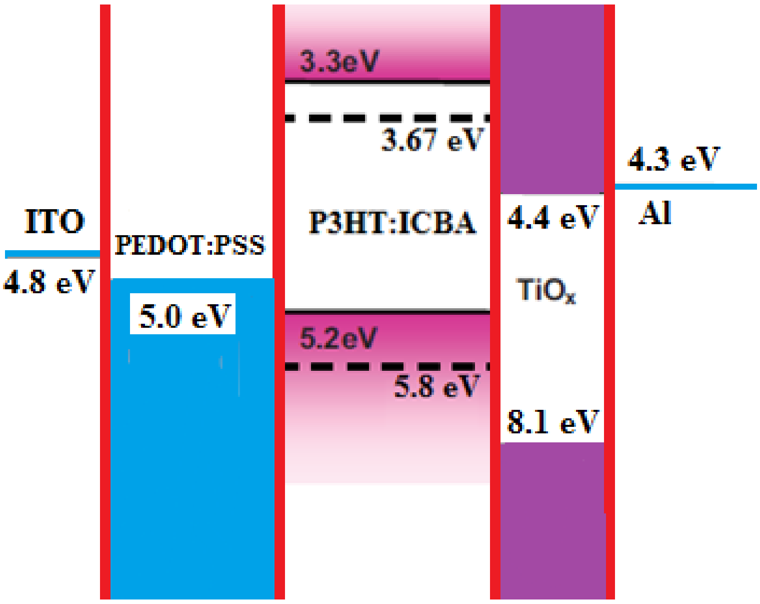

Figure 4.2.5: Energy levels of the ITO/PEDOT:PSS/P3HT:ICBA/TiO_x/Al solar cell.

The function of TiO_x interfacial layer as ETL and HBL is responsible for the improvement in *FF* compared to the reference device without TiO_x layer. As shown in Figure 4.2.5 TiO_x layer with lower HOMO energy level provides higher energy barrier for holes extraction from P3HT HOMO to Al electrode but enhance electron extraction from ICBA LUMO to

Al electrode, and therefore moderating the charge extraction process and leading to higher *FF*.

The other use of TiO_x layer is for protection of P3HT:ICBA film from physical damage by high kinetic energy Al atom during Al evaporation. The mechanism of protection can be explained as follows. During thermal evaporation of Al electrode, the Al atoms with high kinetic energy flux can diffuse into polymer to form a thick interfacial layer. For example, around 5 nm thick interfacial layer between the P3HT:PCBM active layer and the Al contact was formed and resulted in barrier formation for electron extraction [209]. Two hypothesis were suggested to explain the resulting product when polymer comes in contact with high kinetic energy Al atoms. The first is the theoretical work by Logdlund et al. [210, 211]. They proposed a direct reaction for the formation of Al-C bond due to high reductive power of Al. An alternative explanation to Al-C was single-electron transfer with the creation of anion radicals on the polymer [69, 210 - 212]. Both organo-aluminum compounds and anion radicals are highly reactive species that can react with any proton donors present, such as water or oxygen. By the same token, thick organic-Al interfacial layer between P3HT:ICBA active layer and the Al contact caused by the evaporated Al is expected to form and result in barrier formation for electron extraction when unpackaged device is exposed to air. However, when P3HT:ICBA active layer is coated with TiO_x layer, there will be no contact between active layer and Al and the formation of organic-aluminum compounds or the creation of anion radicals on the polymer caused by the evaporation of Al can effectively be avoided or minimized. The absence or minimized thick interfacial layer can improve the charge extraction and device performance.

The calculated values of series resistance (R_s) and shunt resistance (R_{sh}) for both P3HT:ICBA solar cells with and without TiO_x layer are as follows. For device without TiO_x, R_s = 43 Ω.cm^2 and R_{sh} = 6.6 M Ω.cm^2 where as for the device with TiO_x, R_s = 39 Ω.cm^2 and R_{sh} = 10.2 M Ω.cm^2. The introduction of TiO_x layer reduced series resistance by 10%. Low series resistance with the use of TiO_x layer is an evidence for improved ohmic contact at the interface with Al electrode. The reduction in R_s correlates well with the enhancement in J_{sc}. The use of TiO_x layer increased R_{sh} by 54%. The increase of R_{sh} is responsible for the improvement of V_{oc} in P3HT:ICBA/TiO_x device. The higher R_{sh} for P3HT:ICBA/TiO_x device gives clue that TiO_x serves as hole blocking layer.

For better photovoltaic performance the donor polymer, P3HT should be in contact with ITO through PEDOT:PSS and the acceptor material, ICBA in contact with Al electrode [213]. But, due to the bulk heterojunction structure of the active layer, P3HT can also be in contact with Al electrode. The contact of P3HT with Al electrode leads to hole leakage from P3HT to Al electrode and this results in recombination of electrons and holes. Charge carrier recombination leads to lower shunt resistance. However, when TiO_x interfacial layer is used, P3HT will not have access to make contact with Al electrode. TiO_x layer transports mostly electrons due to its LUMO energy level (4.4 eV) match with Al electrode work function. Thus, for the device with TiO_x interfacial layer, P3HT is prevented from making contact with Al electrode. The higher R_{sh} mean that charge carrier recombination is suppressed by the use of TiO_x layer.

The results from electrical measurements show that TiO_x optical spacer contributes for the increase of the device power conversion efficiency. To study the effect of TiO_x layer on photostability of P3HT:ICBA solar cells under light irradiation, TiO_x layer with thickness of 12 nm were used. P3HT:ICBA solar cells without TiO_x layer were used as reference. For all devices, no extra package or encapsulation was used. To investigate the effect of TiO_x layer on the degradation of P3HT:ICBA solar cells, we evaluated normalized values of η, J_{sc}, V_{oc} and FF as a function of the light irradiation time. Figure 4.2.6 - Figure 4.2.9 show the normalized values of η, J_{sc}, V_{oc} and FF of P3HT:ICBA/TiO_x solar cell as a function of light irradiation time in ambient air. In Figure 4.2.6 the normalized η of P3HT:ICBA solar cells fabricated with and without TiO_x layer as a function of light irradiation time gives information on the pattern of solar cell degradation.

Simple comparison of the patterns of decrease in normalized values of η in Figure 4.2.6 reveals that the solar cell based on P3HT:ICBA/TiO_x has relative superior stability under light irradiation in ambient air compared to the reference device. The obtained data indicate the combined effect of oxygen and light irradiation on the change in solar cell efficiency of P3HT:ICBA solar cells. After 300 min of light irradiation, the device without TiO_x interfacial layer showed PCE dropped by 52%. The reference device suffers very rapid photodegradation as indicated by high loss in PCE. For the devices without the TiO_x

interfacial layer aged by irradiation at ambient air, significant decreases in PCE after 300 min of light exposure is mainly caused by the loss of J_{sc} and *FF*. For the device with TiO_x interfacial layer nearly 79% of the initial PCE still remained after 300 min of light exposure. Based on our experimental results, it is reasonable to conclude that the TiO_x interfacial layer plays a key role in retarding photodegradation of P3HT:ICBA active layer.

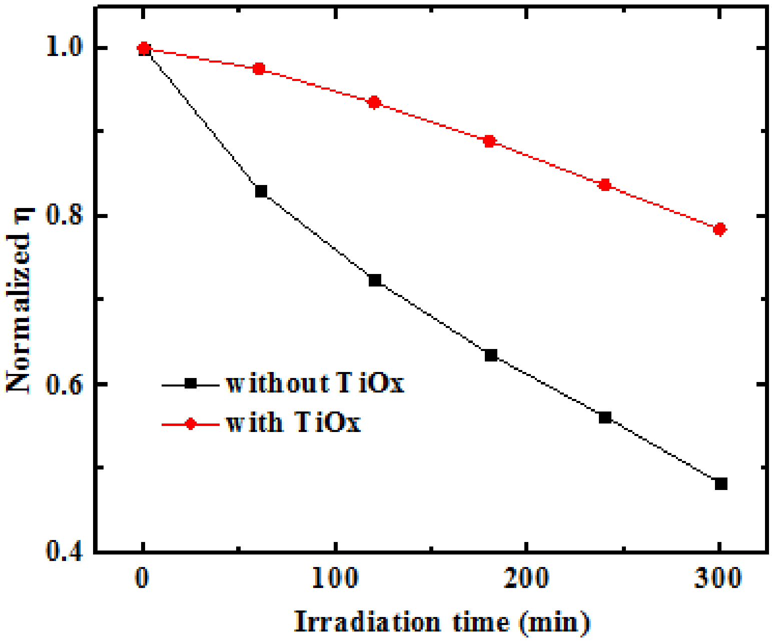

Figure 4.2.6: Normalized η of a P3HT:ICBA devices with and without TiO_x interlayer as a function of light irradiation time in ambient air.

In P3HT:ICBA solar cells, the degradation of the active layer is clearly related to exposure of the active layer to oxygen, moisture and light. However, for the device with TiO_x layer under ambient air and light irradiation the rate of degradation is minimized compared to device without TiO_x interfacial layer. As suggested by Lee et al. [187] and others [191, 202, 203] TiO_x interfacial layer function as a robust diffusion barrier against oxygen and water into active layer because of its scavenging effects due to photocatalysis and oxygen deficiency. The reason for the improved stability of P3HT:ICBA/TiO_x device is that P3HT:ICBA film was protected from oxygen and moisture in the ambient air due to oxygen and moisture scavenging property of TiO_x.

Figure 4.2.7 shows normalized J_{sc} of a P3HT:ICBA devices with and without TiO_x interlayer as a function of light irradiation time in ambient air. Short-circuit current density is affected by light absorption power of the photoactive layer. As the active layer undergoes photodegradation, the conjugation length of the polymer decreases and the light absorption power is reduced. In our particular case, the short-circuit current density of P3HT:ICBA/TiO_x device is relatively stable compared to P3HT:ICBA device. The relatively stable short-circuit current density is indicator of the existence of stable polymer without reduction in conjugation length. If there were reduction in conjugation length, there would have been reduction in short-circuit current density. The existence of stable polymer indicates the non-existence or minimized existence of oxygen and moisture. Under light irradiation when oxygen and moisture exists they cause photooxidation of the polymer and loss of conjugation. The relatively stable short-circuit current density provides a good proof for the role of the TiO_x layer in blocking oxygen and water penetration into the P3HT:ICBA active layer.

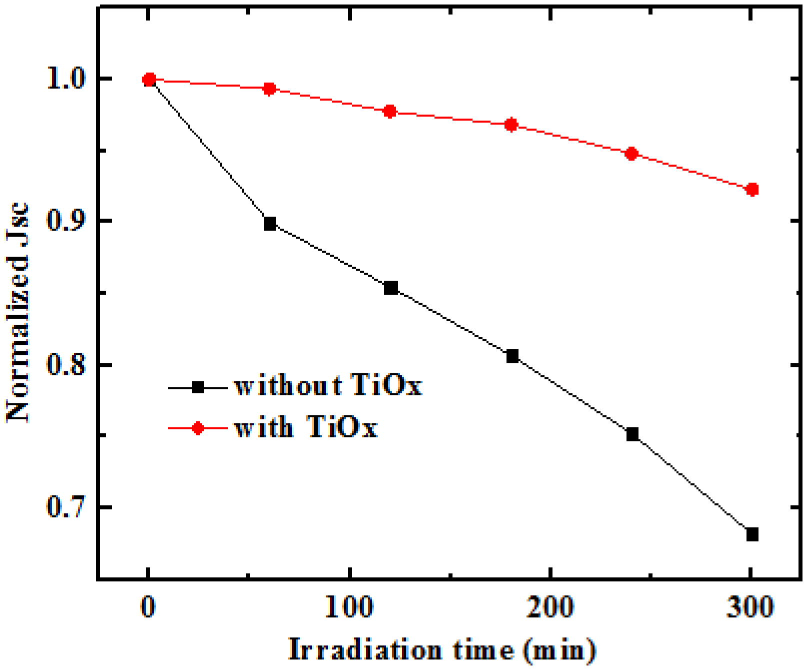

Figure 4.2.7: Normalized J_{sc} of a P3HT:ICBA devices with and without TiO_x interlayer as a function of light irradiation time in ambient air.

Figure 4.2.8 shows normalized *FF* of a P3HT:ICBA devices with and without TiO_x interlayer as a function of light irradiation time in ambient air. In PSC, large serial resistance because of bulk material degradation or degradation of the quality of the photoactive layer electrode interface leads to reduction of FF. In P3HT:ICBA device with

TiO_x interlayer, after 300 min of light irradiation the better value of *FF* (compare to reference device) shows the relative stability of the photoactive layer and quality of the interfaces.

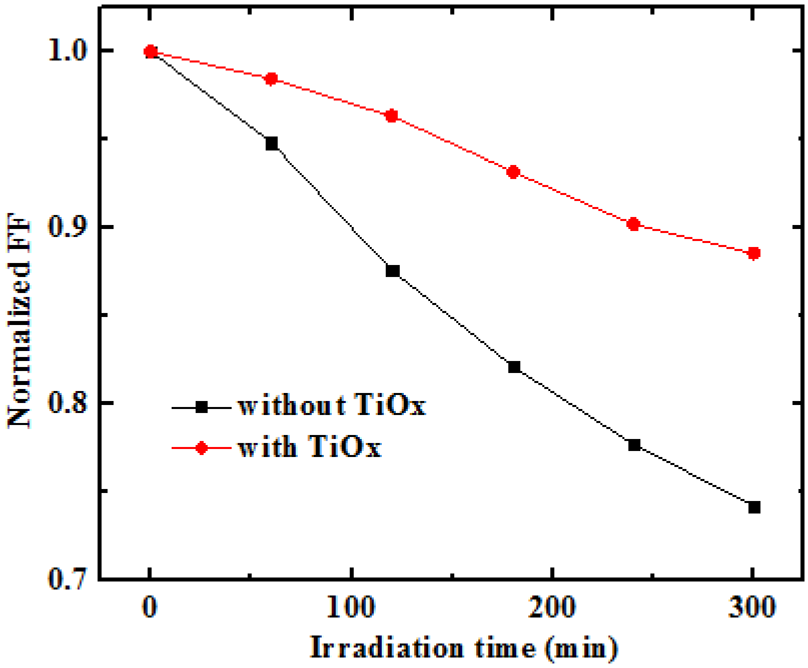

Figure 4.2.8: Normalized *FF* of a P3HT:ICBA devices with and without TiO_x interlayer as a function of light irradiation time in ambient air.

Figure 4.2.9 is the plot of normalized V_{oc} of a P3HT:ICBA devices with and without TiO_x interlayer as a function of light irradiation time in ambient air. V_{oc} decrease may occur upon P3HT doping by oxygen [214 - 216]. In the case of p-type doping a Schottky junction with the cathode is formed, and the band bending with its corresponding electric field is then limited only to the depletion region of the diode, leading to V_{oc} loss. For the device with TiO_x interlayer, the active layer (P3HT) is protected from oxygen attack and as a result it has relatively stable V_{oc}.

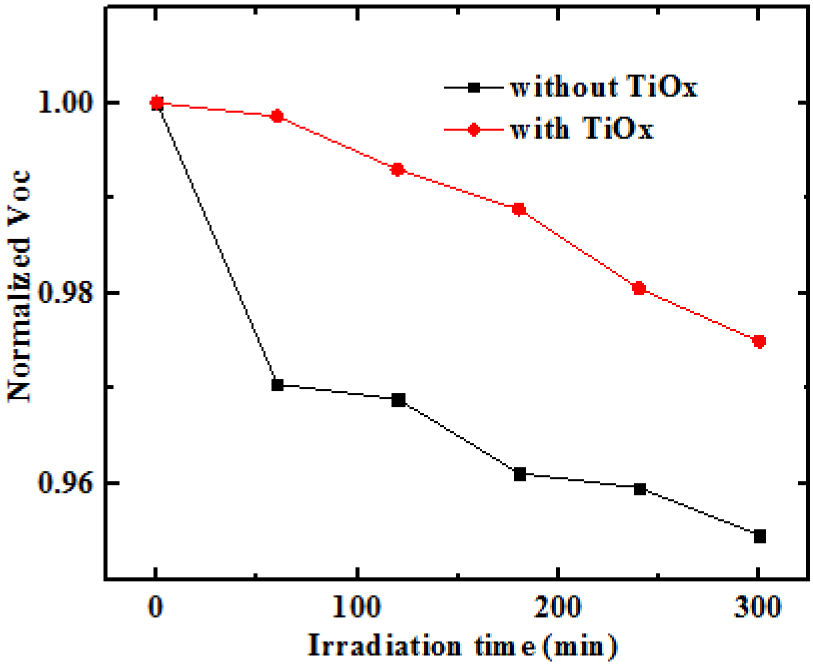

Figure 4.2.9: Normalized V_{oc} of a P3HT:ICBA devices with and without TiO_x interlayer as a function of light irradiation time in ambient air.

4.2.4. Capacitance-voltage characteristics

When exposed to oxygen and/or moisture and light, P3HT undergo p-type doping [216, 217]. When doped P3HT comes in contact with aluminum, it forms Schottky junction. This results in band bending and the formation of depletion region. For a Schottky diode the junction capacitance, which appears as a consequence of the modulation of the depletion layer, exhibits a bias dependence according to the Mott-Schottky relation [147]. Since P3HT shows a Schottky diode behavior the dependence of the depletion width upon the applied voltage provides information on the P3HT's internal characteristics, such as dopant concentration and built-in potential.

Knowledge of dopant concentration in polymer solar cells is very essential since the amount of dopant has direct effect on charge carrier mobility and recombination. To investigate the potential of TiO_x layer to protect P3HT:ICBA film from oxidation due to light irradiation and to probe dopant concentration formed as a result of P3HT oxidation we used capacitance (C) *versus* voltage (V) measurement. We compared the solar cells made of P3HT:ICBA and P3HT:ICBA/TiO_x irradiated under identical conditions. Figure

4.2.10 shows the room temperature *C-V* characteristic of ITO/PEDOT:PSS/P3HT:ICBA/Al diode measured at frequency of 1 kHz and AC oscillating amplitude of 20 mV under dark condition.

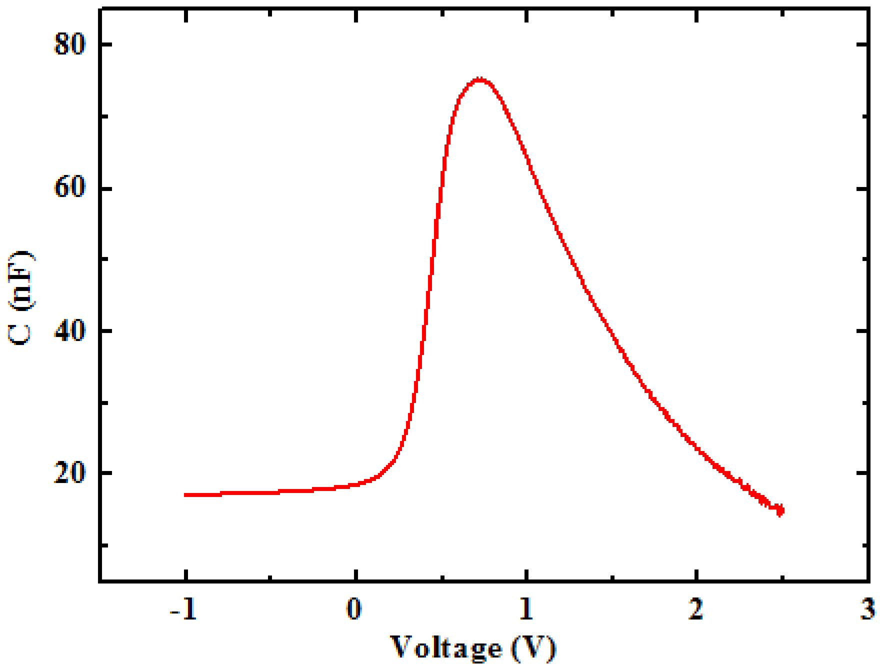

Figure 4.2.10: Room temperature capacitance *versus* voltage characteristic of ITO/PEDOT:PSS/P3HT:ICBA/Al structure measured at frequency of 1 kHz and AC oscillating amplitude of 20 mV under dark condition.

Figure 4.2.11 shows the room temperature C^{-2} *versus* V characteristic of ITO/PEDOT:PSS/P3HT:ICBA/Al diode. From the plot of C^{-2} versus V and with the help of Equation (23) and Equation (24) in section 2.10, the built-in potential (V_{bi}) and the acceptor impurity concentration (N_a) of the ITO/PEDOT:PSS/P3HT:ICBA/Al diode were calculated. By assuming $\varepsilon_s = 4$ for P3HT:ICBA, we have obtained the following results: $V_{bi} = 0.47$ eV and $N_a = 8.7 \times 10^{16}$ cm^{-3}. The depletion width is given by Equation (25) in section 2.10. In the voltage range between 0.46 and -2.5 V the depletion region varies between 3.1 and 130 nm, which is compatible with the active layer thickness of 140 nm. Similar *C-V* results for P3HT:PCBM/Al diode have been reported by G. Garcia-Belmonte et al. [147] $V_{bi} = 0.43$ eV and $N_a = 3.5 \times 10^{16}$ cm^{-3}. Other reported values of N_a for P3HT:PCBM/Al diode includes 2.67 x 10^{16} cm^{-3} [218], 3.85 x 10^{16} cm^{-3} [219], 0.47 x 10^{16} cm^{-3} [207], 3.5 x 10^{18} cm^{-3} [220], 7.0 x 10^{16} cm^{-3} [221], 4.25 x 10^{16} cm^{-3} [222]. Compared to P3HT:PCBM/Al device the relatively higher value of N_a in P3HT:ICBA/Al was expected because, P3HT:ICBA exhibit an increase of dopant density upon exposure to air and/or moisture, caused by a charge transfer reaction with oxygen, not only under light exposure, but also in the dark [71, 221]. The reported literature values for built-in potential are 0.75 eV [218], 0.362 eV [219], 0.35 eV [207], 0.43 eV [220] and 0.5 eV [221].

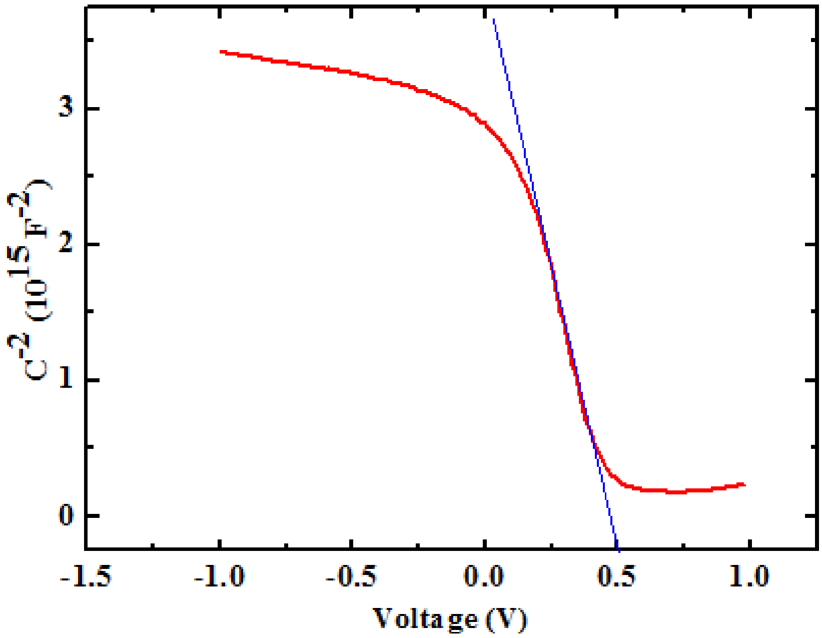

Figure 4.2.11: Room temperature C^{-2} *versus* V characteristic of ITO/PEDOT:PSS/P3HT:ICBA/Al structure measured at frequency of 1 kHz and AC oscillating amplitude of 20 mV under dark condition.

In order to elucidate the potential of TiO_x layer for protection of P3HT:ICBA film from oxidation, the *C-V* characteristic of the ITO/PEDOT:PSS/P3HT:ICBA/Al and ITO/PEDOT:PSS/P3HT:ICBA/TiO_x/Al diodes were measured after exposing the device through ITO side with 100 mW/cm^2 light for different time from solar simulator under ambient air. Under ambient air, with increasing exposure time increase in dopant concentration is expected. Figure 4.2.12 shows the variation of dopant concentration with increasing light exposure time for diodes of ITO/PEDOT:PSS/P3HT:ICBA/Al and ITO/PEDOT:PSS/P3HT:ICBA/TiO_x/Al. As Figure 4.2.12 shows in case of the device without TiO_x interlayer the rate of increase of dopant concentration with increasing exposure time is higher compared to the device with TiO_x interlayer. The obtained result shows the potentail of TiO_x interlayer in protecting the active layer from photodegradation.

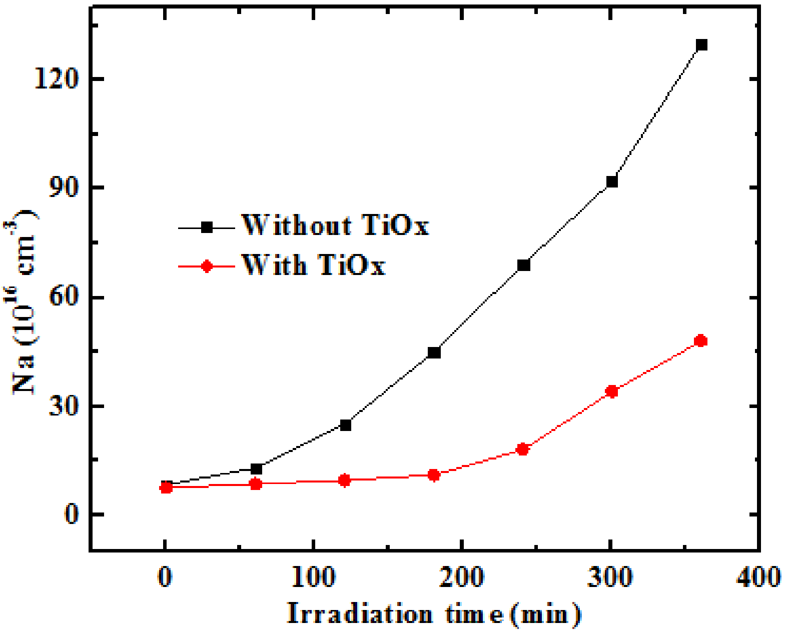

Figure 4.2.12: Variation of dopant concentration in P3HT:ICBA devices with and without TiO_x interlayer as a function of light irradiation time in ambient air.

4.2.5. Conclusions

Effect of TiO_x layer on the performance and stability of P3HT:ICBA based solar cells were investigated by spectroscopic and electrical measurement methods. In this study, we used a sol-gel synthesized TiO_x as the interfacial layer between the active layers of P3HT:ICBA and Al cathode. Results from *J-V* measurements show that P3HT:ICBA/TiO_x solar cell has better photovoltaic performance and stability compared to the reference device. The higher value of short-circuit current density and open-circuit voltage for P3HT:ICBA/TiO_x solar cell indicate the role of TiO_x layer as the optical spacer and hole blocking layer, respectively. For P3HT:ICBA/TiO_x solar cell, after 300 min of light irradiation, 79% of the initial PCE was retained, where as for P3HT:ICBA device showed only 48% of the initial PCE. The obtained results showed that TiO_x layer is an efficient shield against physical and chemical degradation of the P3HT:ICBA active layer. The results from UV-visible absorbance, *J-V* and *C-V* measurement on light irradiated P3HT:ICBA/TiO_x solar cell demonstrates that TiO_x can be used to protect P3HT:ICBA active layer from oxygen and water attack under ambient air and can be used to improve the working lifetime of the P3HT:ICBA based device.

4.3. Effect of Different Fullerene Acceptors on Device Stability of P3HT-based Bulk Heterojunction Solar Cells under Illumination

4.3.1. Background

In the research of polymer solar cell recently achieved PCE of 12% are very encouraging for further research [18, 31, 64, 65, 155, 223]. However, polymer solar cells should not only required to have high efficiency but also reasonably acceptable working lifetime. Many experimental results in the study of polymer solar cells showed that the chemical nature of the fullerene acceptor material is very significant for producing appropriate blend morphology [178, 224, 225]. Acquiring knowledge about the role of fullerene in polymer solar cell is essential not only for the realization of optimal device performance but also for the stability of the blend morphology. Stability of the blend morphology is among the main factors that determine working lifetime of real device.

In section 4.1 we have studied the effect of different electron affinity fullerene acceptors on photostability of P3HT film and device made of P3HT. In this study, we compare the working lifetime and charge carrier mobility of polymer solar cells based on active layer of P3HT and different fullerene derivatives with similar electron affinity as acceptors under the same condition. The fullerenes derivatives used as acceptor are $PC_{61}BM$ and $PC_{71}BM$. Optical properties of P3HT and the blend with $PC_{61}BM$ and $PC_{71}BM$ are studied by measuring UV-visible absorbance at different irradiation time. Light of 100 mW/cm^2 is used for irradiation. Electrical properties of the real devices based on P3HT:fullerene blends were investigated by recording the variation of current density-voltage characteristics of the solar cell irradiated at ambient air with 100 mW/cm^2 light at different time. In order to understand the effect of different fullerene acceptors on the charge carrier mobility (hole and electron mobility) in the blend and pure fullerene films, space charge limited current (SCLC) measurements are performed.

4.3.2. UV-visible absorbance measurement

Figure 4.3.1 shows the UV-visible absorbance spectra of P3HT and the two fullerenes derivatives ($PC_{61}BM$ and $PC_{71}BM$). Strong and broad light absorption of P3HT made it the polymer used for fabricating high performance polymer solar cells [226]. From the UV-visible absorbance spectra it is apparent that $PC_{71}BM$ has better light absorption compared to $PC_{61}BM$. $PC_{71}BM$ absorbs between 400 and 650 nm. The additional absorbance from $PC_{71}BM$ has contribution to increase the short circuit current when real device is fabricated using $PC_{71}BM$ as acceptor.

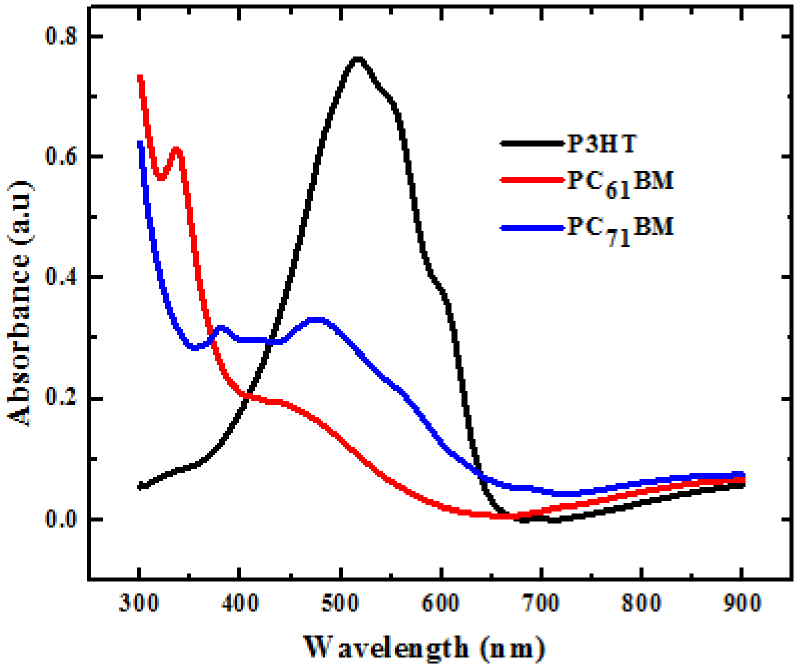

Figure 4.3.1: UV-visible absorbance spectra of P3HT, $PC_{61}BM$ and $PC_{71}BM$ films.

From Figure 4.3.2 it is evident that the blend of P3HT:$PC_{71}BM$ film shows a stronger absorption in the visible range compared to P3HT:$PC_{61}BM$ film due to the contribution from $PC_{71}BM$ as shown in Figure 4.3.1. As shown in Figure 4.3.1 pure film of $PC_{71}BM$ exhibits relatively strong and broad absorption in the wavelength range 400 to 650 nm. The longer wavelength absorption of $PC_{71}BM$ compared to the absorption of $PC_{61}BM$ at 333 nm in the UV light range is an advantage. The additional absorption of $PC_{71}BM$ has better contribution for photon harvesting in the visible range compared to $PC_{61}BM$.

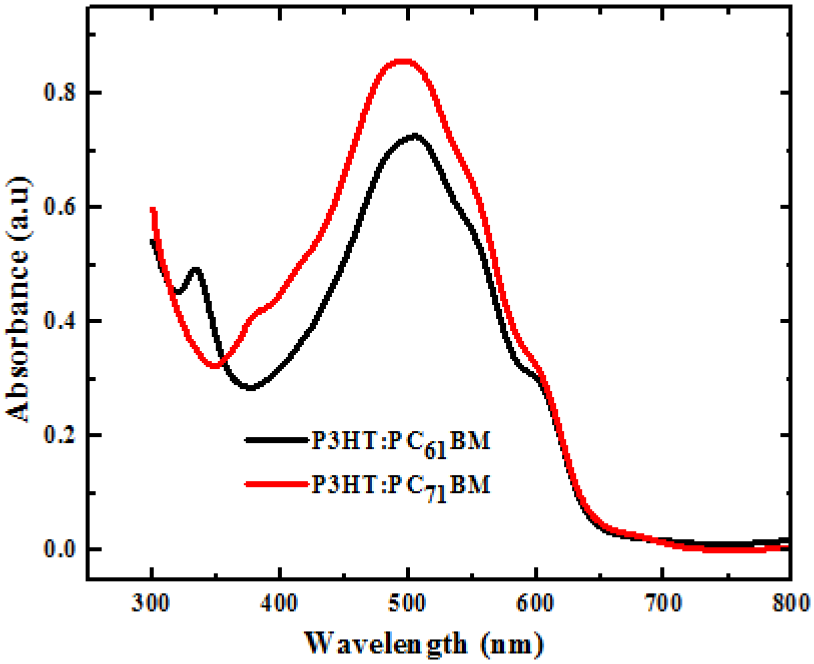

Figure 4.3.2: UV-visible absorption spectra of blend of P3HT:$PC_{61}BM$ and P3HT:$PC_{71}BM$ films.

According to the finding of Nicolaidis et al. [227] in P3HT:$PC_{61}BM$ (1:1) system under air mass (AM 1.5) illumination conditions about 13% of short-circuit current density (J_{sc}) arises from the contribution of the fullerene component. As Figure 4.3.1 shows $PC_{61}BM$ has lower photon absorption compared to $PC_{71}BM$. If $PC_{61}BM$ with lower photon absorption has contribution of 13% to J_{sc}, then it is reasonable to expect higher contribution to J_{sc} when $PC_{71}BM$ is used as acceptor in P3HT based solar cells. The finding of Nicolaidis et al. [227] indicates that when we aimed at fabricating high performance polymer solar cells containing fullerene as acceptor material it is important to consider the possible complementary absorbance by fullerene component and the resulting photocurrent that could be generated by light that is absorbed by the fullerene component. Therefore, based on the UV-visible absorbance spectra and finding of Nicolaidis et al. [227] it is reasonable to suppose that $PC_{71}BM$ will give more contribution to the J_{sc} in P3HT:$PC_{71}BM$ solar cell due to its stronger and broader absorption in the visible light range compared to $PC_{61}BM$.

According to Tromholt et al. [158] UV-visible absorbance measurement of films of polymers at different time give valuable information on the photochemical stability of conjugated polymers. It is known that when P3HT is exposed to heat, light and oxygen it degrades and loses its UV-visible absorption power [23, 67 - 69]. Thus, by measuring UV-visible absorbance spectra of P3HT and its blend with $PC_{61}BM$ and $PC_{71}BM$ it is possible to study the effect of similar electron affinity fullerene acceptors on the photochemical stability of P3HT.

In order to distinguish the effect of similar electron affinity fullerene acceptors on the photochemical stability of P3HT film, we measured the UV-visible absorbance of the film of P3HT and the blends by aging the films using light illumination (100 mW/cm^2) at ambient air and their absorption spectra were measured at different time. Figure 4.3.3 shows the absorbance of P3HT (at 517 nm), P3HT:$PC_{61}BM$ (505 nm) and P3HT:$PC_{71}BM$ (494 nm) film normalized to their initial value as a function of irradiation time in ambient air. As shown in Figure 4.3.3, the intensity of the absorption band at 517 nm of pure P3HT film decreases continuously with irradiation time at ambient air and this indicates the poor light stability of P3HT. The decrease of UV-visible light absorption corresponds to changes in degree of conjugation in P3HT (interruption of the π-conjugation leads to a decrease of the UV-visible absorbance) and/or ordering of the P3HT chains (e.g. due to chain scission) [23, 65, 69]. However, in case of P3HT mixed with either $PC_{61}BM$ or $PC_{71}BM$, the intensity of the absorption band at 505 nm for P3HT:$PC_{61}BM$ and 494 nm for P3HT:$PC_{71}BM$ films are relatively constant compared to pure P3HT film. The films of P3HT:$PC_{61}BM$ and P3HT:$PC_{71}BM$ blends have almost similar and constant absorbance under illumination.

In Figure 4.3.3, simple inspection of normalized UV-visible absorbance of P3HT, P3HT:$PC_{61}BM$ and P3HT:$PC_{71}BM$ films show that both $PC_{61}BM$ and $PC_{71}BM$ fullerene acceptors stabilized the P3HT film compared to the pure film of P3HT. The stabilizing power of both fullerenes helps to improve the working lifetime of P3HT based polymer solar cells. Based on UV-visible absorbance results the viable conclusion is that the air photochemical stability of P3HT does appear to be significantly affected and improved by the different fullerenes acceptors used in this study. In our previous study we found out that ICBA is inferior in stabilizing the film of P3HT compared to $PC_{61}BM$.

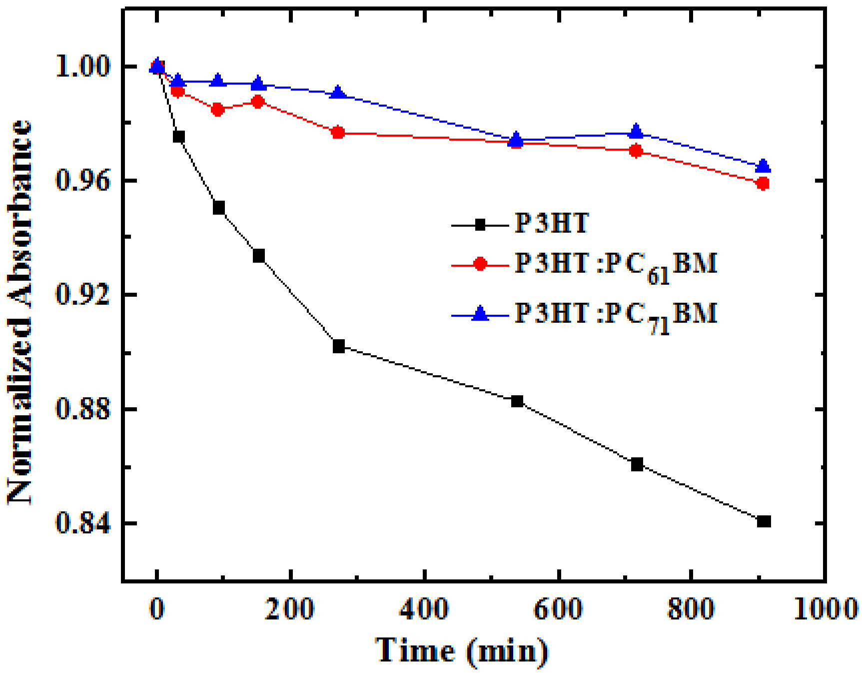

Figure 4.3.3: Normalized UV-visible absorbance of P3HT (at 517 nm), P3HT:PC$_{61}$BM (at 505 nm) and P3HT:PC$_{71}$BM (at 494 nm), film as a function of irradiation (100 mW/cm^2 light) time at ambient air.

The obtained results in Figure 4.3.3 is consistent with the prediction of photochemical stability of polymer blends (polymer mixed with different fullerene) based on the electron affinity of different fullerene acceptors by Hoke et al. [100]. Based on Hoke et al. [100] result and LUMO levels of the two fullerenes acceptors [228], it is expected that the blend of P3HT with PC$_{61}$BM is expected to have slightly lower air photochemical stability in comparison with the blend of P3HT with PC$_{71}$BM. In Figure 4.3.3 irradiation time dependent normalized UV-visible absorbance results show that P3HT:PC$_{61}$BM film is a bit lower in photochemical stability compared to P3HT:PC$_{71}$BM film.

4.3.3. Charge carrier mobility measurement

From experimental work conducted on polymer solar cells, it is evident that the photochemical stability of the film and morphology of the active layer have an effect on charge carrier mobility [224]. To investigate the influence of similar electron affinity fullerene acceptors on the charge carrier mobility, we carried out charge carrier mobility measurement for both holes and electrons in the blend as well as in the pure films of P3HT,

$PC_{61}BM$ and $PC_{71}BM$ using space charge limited current (SCLC) analysis of current density-voltage (*J-V*) characteristics in the dark.

4.3.3.1. Electron transport in fullerenes derivatives films and P3HT:Fullerene blend

To measure the mobility of electron in different fullerene acceptor as well as P3HT:Fullerene films we used electron only single-carrier device. For electron only device aluminum oxide is used as anode. The structure of electron only single-carrier device is as follows: Glass/Al/Fullerene/Al and Glass/Al/P3HT:Fullerene/Al. Based on the work functions of Al, it is expected that Al forms an Ohmic contact for electron injection into fullerene film [229 - 231]. The work function of aluminum oxide does not match with HOMO level of both fullerene acceptors, therefore, without much compromise hole injection from Al electrode into fullerene acceptors films can be neglected. Accordingly, only electrons are expected to flow through the fullerenes films under forward bias conditions. The values of electron mobility in $PC_{61}BM$, $PC_{71}BM$ and in their blend with P3HT were calcualted by using SCLC method.

For all films, $\varepsilon_s = 4$ [77, 181], $\varepsilon_o = 8.854 \times 10^{-12}$ F/m is used. Substituting the relevant values in Equation [18] and a linear fit of J *versus* V^2 give the value of electron mobility. The obtained electron mobility in the pristine film of $PC_{61}BM$ and $PC_{71}BM$ are 4.7×10^{-4} cm^2/Vs and 1.6×10^{-4} cm^2/Vs, respectively. From our measurement and calculations we can conclude that at room temperature, the electron mobility of $PC_{61}BM$ film is higher than the electron mobility of pristine $PC_{71}BM$ films. The lower electron mobility in $PC_{71}BM$ films as compared to $PC_{61}BM$ films indicates that disorder may play an important role in the reduction of electron mobility in $PC_{71}BM$ films.

The calculated value of electron mobility is 2.5×10^{-4} cm^2/Vs and 8.0×10^{-5} cm^2/Vs for Al/P3HT:$PC_{61}BM$/Al and Al/P3HT:$PC_{71}BM$/Al diode, respectively. In the blend of P3HT:Fullerene film, electrons are transported through the n-type fullerene molecules, therefore, the different electron mobility can be correlated with the different fullerene structures. The electron mobility in film of P3HT: $PC_{61}BM$ is lower than the mobility in pure film of $PC_{61}BM$. Therefore, it is possible to conclude that the electron mobility in the blend film is affected by the presence of P3HT. The result is expected because when

$PC_{61}BM$ is mixed with P3HT, the percolation pathways for the transport of electrons in the $PC_{61}BM$ phase will be disturbed due the existence of P3HT and this result in lower current. The same conclusion can be used for the higher electron current observed in pure film of $PC_{71}BM$ compared to P3HT:$PC_{71}BM$ blend film.

4.3.3.2. Hole transport in pure P3HT films and P3HT:Fullerene blend

In order to identify the effect of different acceptor materials on hole mobility, we measured the hole mobility in the pure film of P3HT and the blend of P3HT:$PC_{61}BM$ and P3HT:$PC_{71}BM$. In order to investigate the hole transport in pure film of P3HT and through the P3HT phase in P3HT:Fullerene blend, the electron current through the fullerene phase have to be blocked by using high work function metal as cathode. In the measurement of hole mobility in polymers and polymer:fullerene blend the use of gold as cathode is very common since it effectively blocks the injection of electrons [232]. Therefore, gold is the best alternative to block electron injection in the pure P3HT as well as in the blend of P3HT and different fullerene acceptors. Because of large injection barrier for electrons from gold into P3HT and P3HT:fullerene films, the experimental current that flows through ITO/PEDOT:PSS/P3HT/Au and ITO/PEDOT:PSS/P3HT:Fullerene/Au device is strongly suppressed and the device can be taken as hole only device. With the reasonable assumption that the devices are hole only devices, the *J-V* measurements can provide information on the hole mobility in P3HT and P3HT:Fullerene blend film.

The calculated hole mobility in the pure film of P3HT is 1.7×10^{-3} cm^2/Vs. For the blends the calculated value of hole mobility is 7.0×10^{-5} cm^2/Vs and 1.9×10^{-5} cm^2/Vs for ITO/PEDOT:PSS/P3HT:$PC_{61}BM$/Au and ITO/PEDOT:PSS/P3HT:$PC_{71}BM$/Au diode, respectively. The different hole mobility in the blend of P3HT:Fullerene film shows that the crystallinity of the polymer film is affected differently by the different fullerene acceptors used. Generally, in polymer solar cells unbalanced charge carrier mobility between hole and electron in the blend results in development of space charge which can hinder further extraction of charge carriers and results in lower fill factor. Based on the difference in mobility between hole and electron in blend of P3HT and the two fullerene acceptors, we expect lower *FF* in case of P3HT:$PC_{71}BM$ based polymer solar cell.

4.3.4. Current-voltage characteristics in the dark

Figure 4.3.4 shows the variation of dark current density *versus* voltage for (a) P3HT:PC$_{71}$BM and (b) P3HT:PC$_{61}$BM BHJ solar cell devices aged at ambient air with irradiation of 100 mW/cm^2 light. For P3HT:PC$_{71}$BM diode n = 1.6, whereas for P3HT:PC$_{61}$BM diode it is 1.4. The diode ideality factor is higher for P3HT:PC$_{71}$BM device. Higher values of the diode ideality factor have been associated with increased recombination loss or increased disorder in the electronic states [88, 168 - 170]. Recombination through surface or interface states can lead to deviations of the ‘ideal’ ideality factor from ideal value (n = 1) [171, 233]. Thus, the increase in the diode ideality factor can be attributed to an increase in interfacial trap-assisted trapping and recombination due to the formation of recombination centers as a result of photodegradation of P3HT and fullerene or increased electronic disorder in the BHJ [168, 169, 172]. However, the result from UV-visible shows that in blend of P3HT:PC$_{61}$BM and P3HT:PC$_{71}$BM the films are stable in the study time. Therefore, it is not the photooxidation of the donor and acceptor that increased diode ideality factor but it could be the appearance of electronic disorder in the BHJ. As shown in Figure 4.3.4 with increasing ageing time the exponentiality of the diode dark current decreased, indicating that the formation of trap state reduces the “quality” of the P3HT:PC$_{71}$BM and P3HT:PC$_{61}$BM diode. Nevertheless, in comparison the rate of reduction is higher for P3HT:PC$_{71}$BM diode.

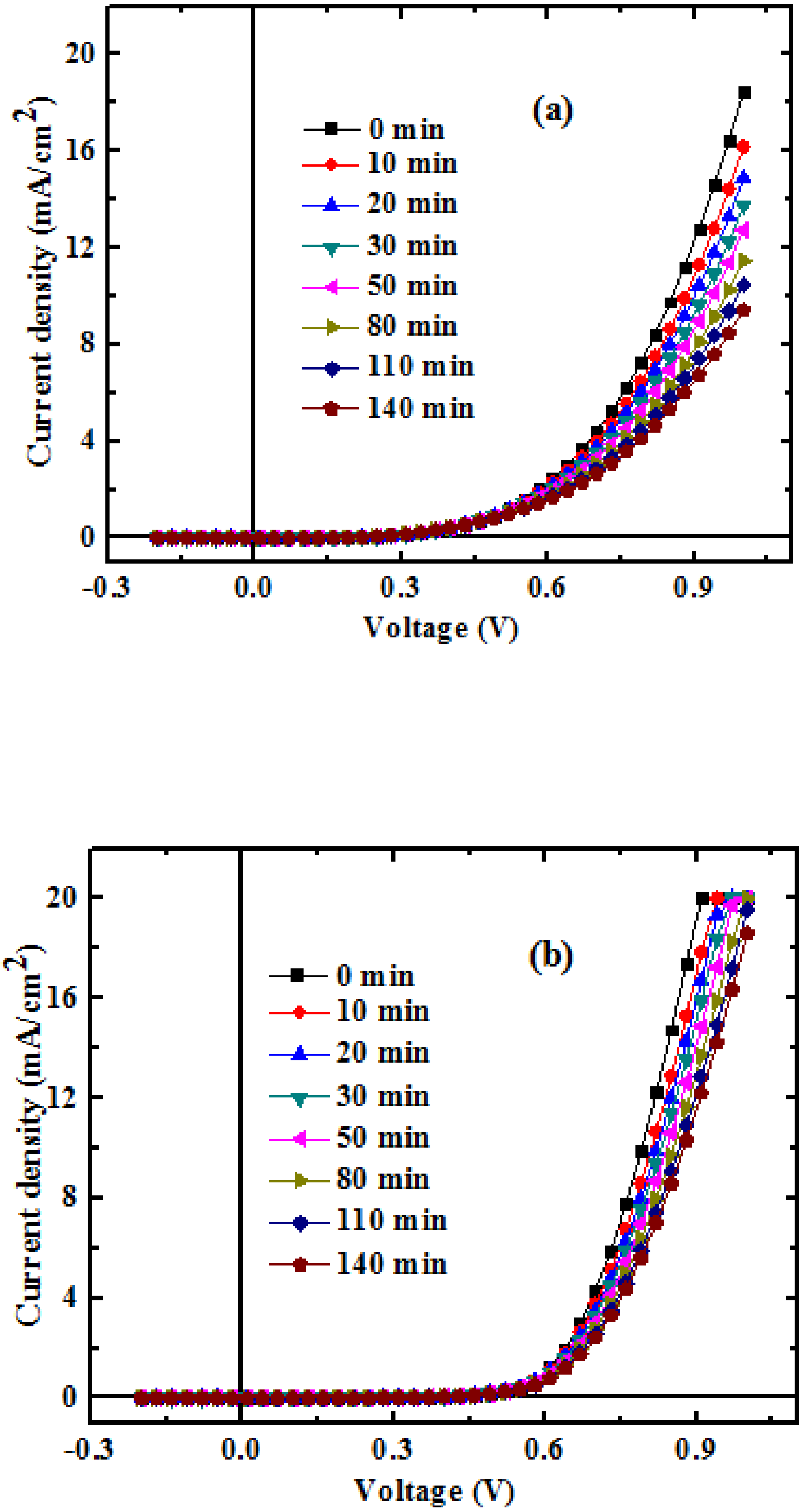

Figure 4.3.4: Dark current density *versus* voltage in the dark for (a) P3HT:PC$_{71}$BM and (b) P3HT:PC$_{61}$BM BHJ solar cell devices aged at ambient air with irradiation of 100 mW/cm^2 light.

Figure 4.3.5 below shows the variation of normalized series resistances (R_s) of P3HT:PC$_{61}$BM and P3HT:PC$_{71}$BM solar cells as a function of irradiation (100 mW/cm^2 light) time at ambient air. From Figure 4.3.5 it is obvious that with increasing irradiation time, the series resistance of the device based on P3HT:PC$_{71}$BM blend increases continuously, however the value for the device based on P3HT:PC$_{61}$BM active layer is almost constant.

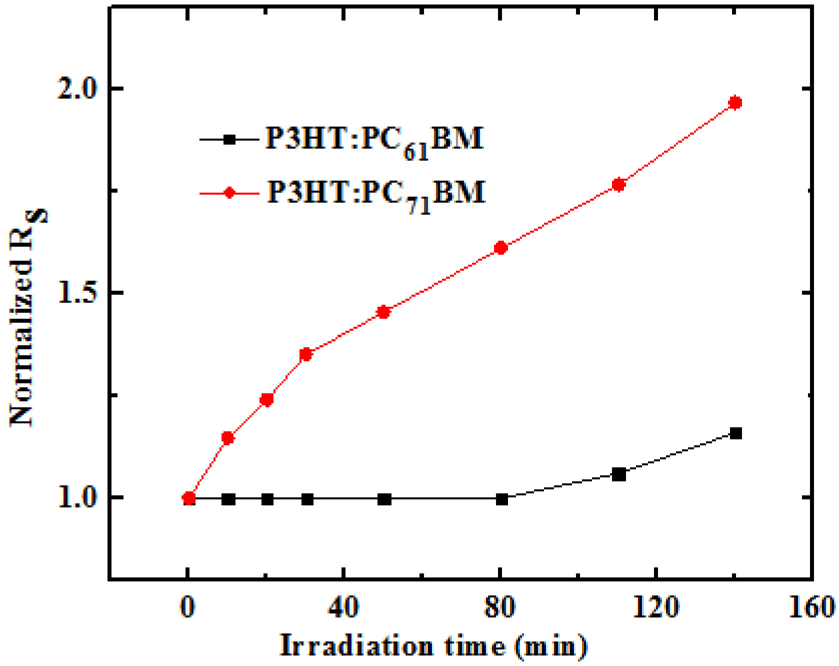

Figure 4.3.5: Normalized R_s of P3HT:PC$_{61}$BM and P3HT:PC$_{71}$BM solar cells as a function of irradiation (100 mW/cm^2 light) time at ambient air.

4.3.5. Photovoltaic measurements

Based on the results of UV-visible absorbance data at different irradiation time, the better stabilization of P3HT film by PC$_{61}$BM and PC$_{71}$BM motivated us to further investigate the effect of different acceptors on working lifetime of solar cells made from P3HT and the two fullerene acceptors. In order to test the photovoltaic performance efficiency stability of real device, solar cells were fabricated from the blend of P3HT:PC$_{61}$BM or P3HT:PC$_{71}$BM and their efficiency stability in air under illumination were measured, computed and compared. In Figure 4.3.6 we see degradation of both devices irrespective of the type of fullerene acceptor used. However, when we compare the rate of reduction, it is higher in case of device where PC$_{71}$BM is used as acceptor.

Based on the UV-visible absorbance result we said that $PC_{71}BM$ imparts similar photochemical stability with $PC_{61}BM$ to the film of P3HT. However, as we can see in Figure 4.3.6, the rate of reduction of photovoltaic performance efficiency of P3HT:$PC_{71}BM$ based device is higher. We speculate that photodegradation of the active layer may not be the cause for the continuous decline of efficiency because UV-visible absorbance results show that the film of P3HT:$PC_{71}BM$ is equally stable with that of P3HT:$PC_{61}BM$ under continuous illumination. Accordingly, the cause for the higher rate of decline of efficiency may be something different from the photochemical stability of the polymer. This indicates that working lifetime of polymer solar cell is controlled by many factors in addition to the photochemical stability of photoactive polymer. Photochemical stability of the donor polymer is just one factor that determines efficiency. The photochemical stability of the photoactive layer is necessary but not sufficient condition.

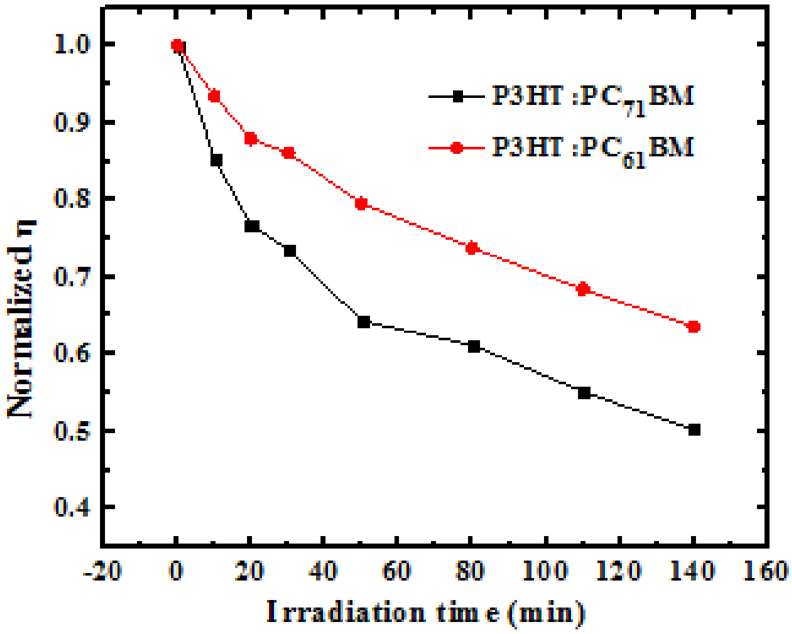

Figure 4.3.6: Normalized η of P3HT:$PC_{61}BM$ and P3HT:$PC_{71}BM$ solar cells as a function of irradiation (100 mW/cm^2) time at ambient air.

To study the influence of different fullerenes acceptors on device working lifetime, we compared the device short-circuit current density (J_{sc}) as a function of irradiation time at ambient air (Figure 4.3.7). Irradiation of the device causes accelerated aging and reduction of J_{sc}. In Figure 4.3.7 comparing the rate of normalized short-circuit current density reduction shows that when $PC_{71}BM$ is used as acceptor, the rate of decrease of short-circuit current density is slightly higher. Generally, photooxidation of the donor polymer (loss of polymer conjugation) of the photoactive layer is responsible for the reduction of light absorption and resulting in lower J_{sc}. Nevertheless, photooxidation of P3HT may not be responsible for the difference in rate of reduction of short circuit-current density between P3HT:PC$_{61}$BM and P3HT:PC$_{71}$BM based solar cells since as we have seen in the UV-visible absorbance measurement, with light irradiation the absorbance of the film of P3HT:PC$_{71}$BM were equally stable with that of P3HT:PC$_{61}$BM film. Therefore, relatively higher rate of reduction could be related with the morphology of the P3HT:PC$_{71}$BM film.

Morphology degradation affects charge dissociation potential at the interface between donor polymer and acceptor material. Morphology degradation also negatively affects charge transport to the electrodes [92]. Thus, for P3HT:PC$_{71}$BM based device decrease of short circuit-current density after device irradiation can be related with a decrease of donor acceptor interface or increase of the blend domains (above the diffusion length of the exciton) caused by morphology degradation of the device. Due to lower solubility of PC$_{71}$BM in DCB, there could be large PC$_{71}$BM aggregates and the larger PC$_{71}$BM aggregates could hinder integration of PC$_{71}$BM molecules into the P3HT domain [225]. With increasing exposure time the PC$_{71}$BM aggregates are expected to increases further and decreases the P3HT:PC$_{71}$BM interface area compared to P3HT:PC$_{61}$BM.

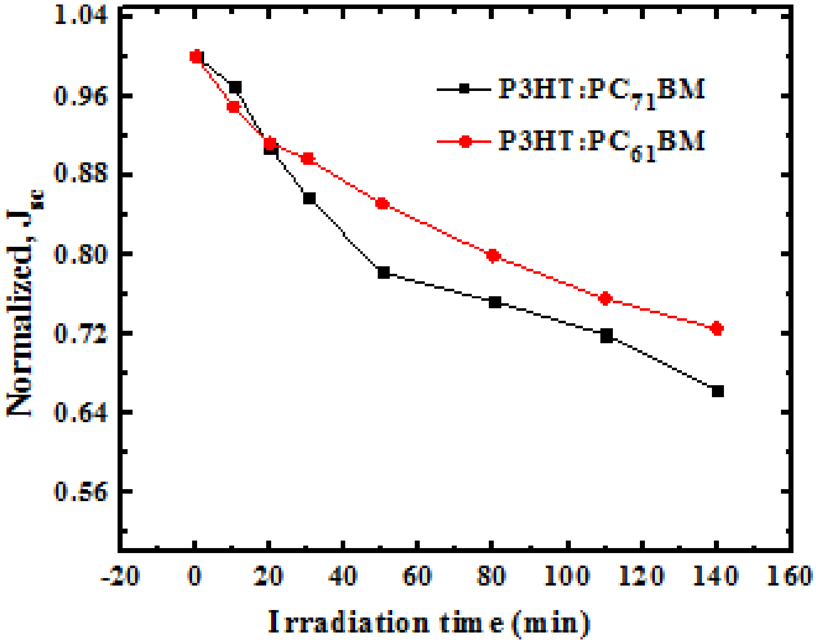

Figure 4.3.7: Normalized J_{sc} of P3HT:PC$_{61}$BM and P3HT:PC$_{71}$BM solar cells as a function of irradiation (100 mW/cm^2) time at ambient air.

As shown in Figure 4.3.8 for P3HT:PC$_{61}$BM device, open-circuit voltage remained almost constant during the aging experiment, while that of P3HT:PC$_{71}$BM device exhibited a fast reduction of open-circuit voltage with aging time. The value of V_{oc} is linked to the energy levels in the donor polymer and acceptor material. When there is photooxidation, UV-visible absorbance decreases due to chemical change and as a result of chemical change the energy level changes. Photochemical stability deduced from UV-visible absorbance data indicates the stability of the energy levels in the donor polymer and acceptor fullerenes. Thus, the cause for reduction of V_{oc} may not be related with photooxidation of the P3HT:PC$_{71}$BM film.

Experimentally observed results show that PC$_{71}$BM has poor miscibility with P3HT [225]. Due to poor miscibility of PC$_{71}$BM with P3HT, the blend may have poor contact to the top electrode. With aging the already poor contact to the top electrode deteriorates continuously. It is known that V_{oc} is affected by the quality of the contact between the blend and top electrode [92]. Hence, under constant illumination deterioration of the contact to the top electrode increases for P3HT:PC$_{71}$BM device and ends up with reduced V_{oc} [224].

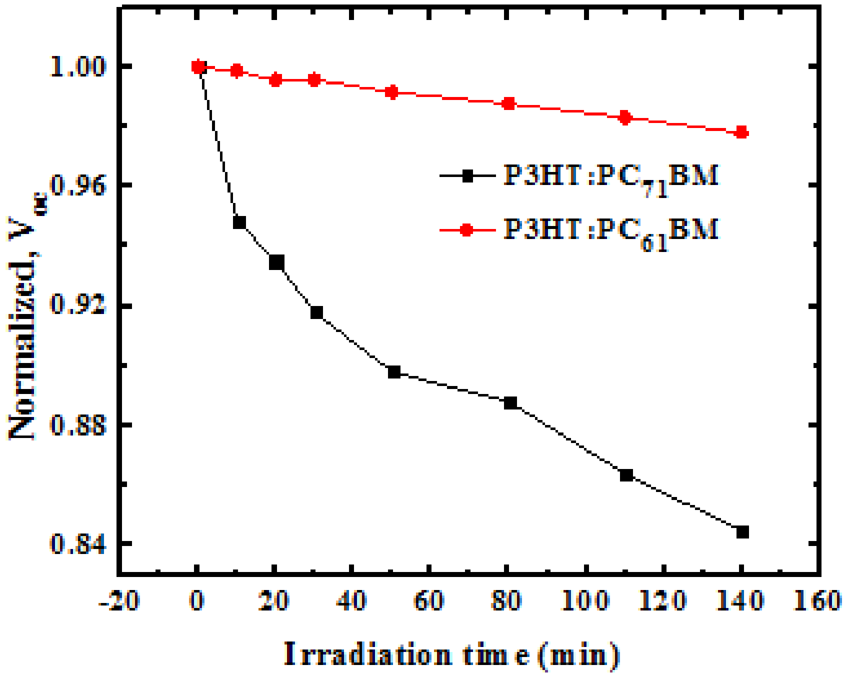

Figure 4.3.8: Normalized V_{oc} of P3HT:PC$_{61}$BM and P3HT:PC$_{71}$BM solar cells as a function of irradiation (100 mW/cm^2) time at ambient air.

The relatively lower electron mobility and the relatively big size of $PC_{71}BM$ molecule influence the phase separation and charge transport in $P3HT:PC_{71}BM$ solar cells [234]. The formation of space charges region due to unbalanced transport of hole and electron results in lower *FF*. The lower *FF* for $PC_{71}BM$ based device also may arised due to poor interfacial contact between the metal electrode and the active layer [235]. It is found out that with increasing the size of the fullerene cage, the solubility of the big size fullerene derivatives becomes inferior and the miscibility of the fullerene derivative with donor polymers diminishes from $PC_{61}BM$ to $PC_{71}BM$ [225, 236]. Different miscibility of the two fullerenes results in different morphology of active layer. For efficient exciton splitting, the donor and acceptor materials should be intermixed at a length scale less than the exciton diffusion length. The *FF* is sensitive to competition between photocurrent generation and charge recombination and therefore is significantly impacted by the morphology of the active layer. If the miscibility is poor it is clear that the interface between the active layer and electrode and quality of the device will be not good and results in low *FF*. The normalized fill factor shows that the rate of reduction of fill factor is higher for P3HT: $PC_{71}BM$ based device (Figure 4.3.9) due to the above mentioned reasons.

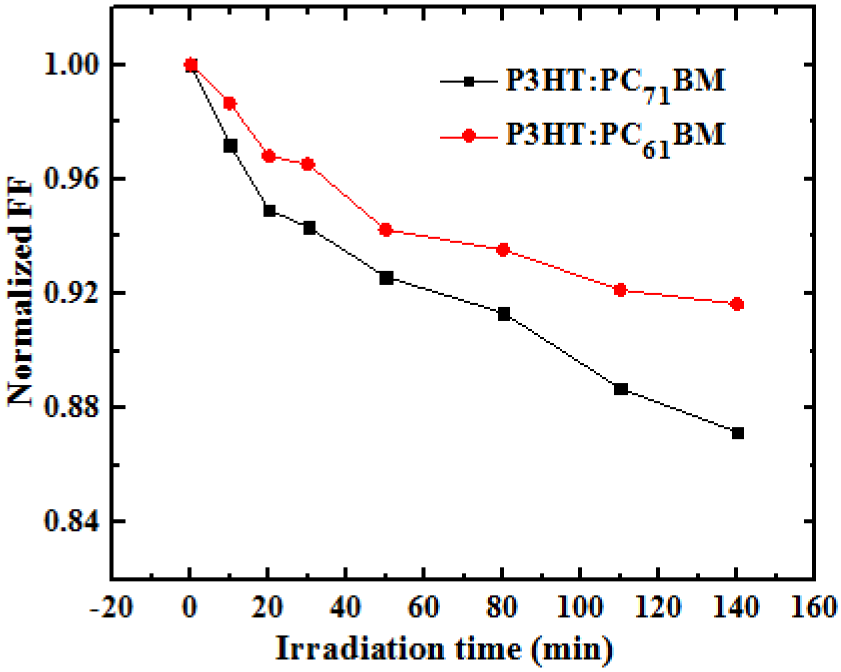

Figure 4.3.9: Normalized *FF* of $P3HT:PC_{61}BM$ and $P3HT:PC_{71}BM$ solar cells as a function of irradiation (100 mW/cm^2) time at ambient air.

Figure 4.3.10 shows the comparison of external quantum efficiency (EQE) of fresh and aged P3HT:PC$_{61}$BM and P3HT:PC$_{71}$BM solar cells. The devices were aged by irradiation with 100 mW/cm^2 light at ambient air for 812 min. The P3HT:PC$_{61}$BM aged device shows change of EQE from 74% to 72% at 505 nm (2.7% relative reduction). In contrast, for P3HT:PC$_{71}$BM the EQE of aged device decreased and the maximum EQE dropped from 73.3% at 505 nm to 68.5% (6.6% relative reduction). For solar cell based on P3HT:PC$_{71}$BM the EQE has decreased after illumination for 812 min, nevertheless, there is no noticeable difference in the shape of the curves before and after light illumination. The implication of the observation is that illumination of the film did not change the original characteristics of the materials in the BHJ films but instead affected the arrangement of the polymer chains and PC$_{71}$BM molecules [237]. Therefore, the observed decrease in EQE efficiency is attributed to the recombination of singlet excitons or free electrons and holes as a result of traps formed in the active layer or at the interface between active layer and electrode. The emergence of traps also hinder charge transport due to enhanced disorder and reduce charge carrier mobility in the bulk heterojunction material and as a result only a fraction of the carriers generated are extracted before recombination.

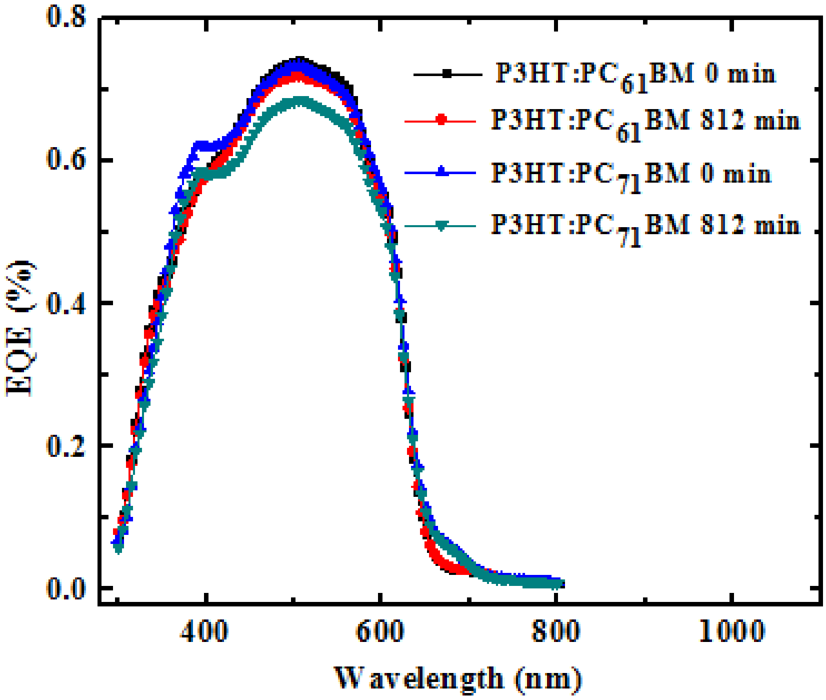

Figure 4.3.10: EQE measurement of fresh and aged devices. The devices were aged by irradiation with 100 mW/cm^2 light at ambient air for 812 min.

4.3.6. Conclusions

We have investigated the effect of two different fullerene acceptors with similar electron affinity on the photovoltaic performance and stability of P3HT based solar cells. From UV-visible measurements we found out that P3HT mixed with both $PC_{61}BM$ and $PC_{71}BM$ has good ambient air photochemical stability. The better UV-visible absorbance stability in P3HT:$PC_{61}BM$ and P3HT:$PC_{71}BM$ blend film under illumination draws attention to the importance of different fullerene acceptors for fabrication of long working lifetime P3HT based bulk heterojunction solar cells. Based on SCLC measurements, $PC_{61}BM$ has higher electron mobility than that of $PC_{71}BM$ film. Similarly, blend of P3HT:$PC_{61}BM$ has higher electron mobility. Regarding device stability, P3HT:$PC_{61}BM$ based device has better stability compared to P3HT:$PC_{71}BM$ based devices.

Given that both devices used the same P3HT donor polymer, it appears that the different power conversion efficiency, short-circuit current density, open-circuit voltage and device photostability are caused by the different fullerene acceptors used. When designing new acceptor materials for polymer solar cells, complementary light absorption, good miscibility with donor polymer and charge transport in the acceptor phase should be considered. Acquiring knowledge about the effect of different fullerene acceptors is essential in the search for alternative fullerene acceptor materials with higher power conversion efficiency and improved device working lifetime.

4.4. Investigation on the Effects of $PC_{61}BM$, $PC_{71}BM$ and their Mixture on Photovoltaic Performance and Stability of PCDTBT:Fullerene Solar Cells

4.4.1. Background

PCDTBT is one of a relatively large class of push-pull carbazole-based copolymers that have been developed to better harvest the solar radiation spectrum. PCDTBT has gained attraction as a promising candidate for next generation materials due to its deep highest occupied molecular orbital (HOMO) energy level to enhance the open circuit voltage (V_{oc}) and the PCE of BHJ polymer solar cells [16]. PCDTBT has high hole mobility, which is, required to remove photoexcited holes from the heterojunction layer effectively [59].

In this work, we have fabricated bulk heterojunction solar cells using a blend of PCDTBT and $PC_{61}BM$, $PC_{71}BM$ and their mixture and studied the effect of different acceptors on the stability of photovoltaic performance under illumination. Spectroscopic and electrical studies were carried out to study the effect of light irradiation on photochemical stability of PCDTBT, PCDTBT:$PC_{61}BM$, 1:1 mixture of PCDTBT:$PC_{61}BM$ and PCDTBT:$PC_{71}BM$, PCDTBT:$PC_{71}BM$ film and solar cells made from the films. From now on the symbol "PCDTBT:$PC_{61+71}BM$" will always mean 1:1 mixture of PCDTBT:$PC_{61}BM$ and PCDTBT:$PC_{71}BM$.

4.4.2. Evolution of UV-visible absorbance

PCDTBT is a class of low bandgap materials that allow absorption of photons further in the solar spectrum. As low bandgap polymers PCDTBT is promising for photon absorption as well as fine tuning of its electronic properties. PCDTBT (Figure 4.4.1) shows two absorption peaks where the first peak at 395 nm can be related to π-π^* electronic transition and the second peak at 570 nm is due to intramolecular charge transfer between donor moeity and the acceptor moeity of PCDTBT [105]. The bandgap of (E_g) PCDTBT is around 1.8 eV [16], which better harvest the solar spectrum compared to polythiophene derivatives where their E_g of 2.0 eV [238].

Figure 4.4.1 shows the UV-visible absorbance spectra of PCDTBT, PCDTBT:PC$_{61}$BM, PCDTBT:PC$_{61+71}$BM, PCDTBT:PC$_{71}$BM film. To mimic BHJ solar cells active layer thickness, the concentration of the solutions used for film formation for UV-visible studies were the same as those used for real device fabrication. When we compare the UV-visible absorbance spectra of the blends, the films of PCDTBT:PC$_{61+71}$BM, PCDTBT:PC$_{71}$BM have stronger absorption in the visible range 440 to 500 nm compared to PCDTBT:PC$_{61}$BM film due to additional absorbance from PC$_{71}$BM. The additional absorption of PC$_{71}$BM has better contribution for photon harvesting in the visible range compared to PC$_{61}$BM when mixed with PCDTBT.

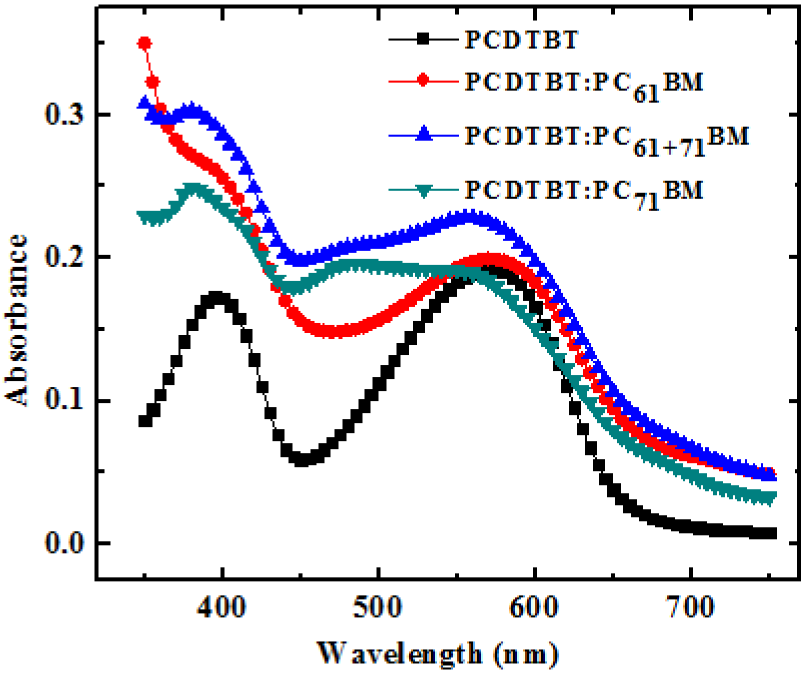

Figure 4.4.1: UV-visible absorbance spectra of PCDTBT, PCDTBT:PC$_{61}$BM, PCDTBT:PC$_{61+71}$BM and PCDTBT:PC$_{71}$BM film.

Figure 4.4.2 shows the UV-visible absorbance spectra of PCDTBT thin film irradiated in ambient air. Before light irradiation, PCDTBT had two absorption bands at 395 nm and 570 nm. However, after continuous light irradiation, continuous decreases in the intensity of the two absorption bands are observed. After 330 min of light irradiation both absorption bands disappeared (Figure 4.4.2) indicating the complete breakdown of π-conjugated backbone of PCDTBT during irradiation. The observation indicates that light irradiation provoked the photobleaching of PCDTBT film. The change of UV-visible absorbance spectra imply that π-π* absorption spectrum is significantly affected by constant irradiation in ambient air. As shown in Figure 4.4.2 with continuous light irradiation, we can notice a blue-shift of the absorption maximum, initially located at 570 nm. Blue shift indicates a reduction of π-conjugation length of the polymer [92].

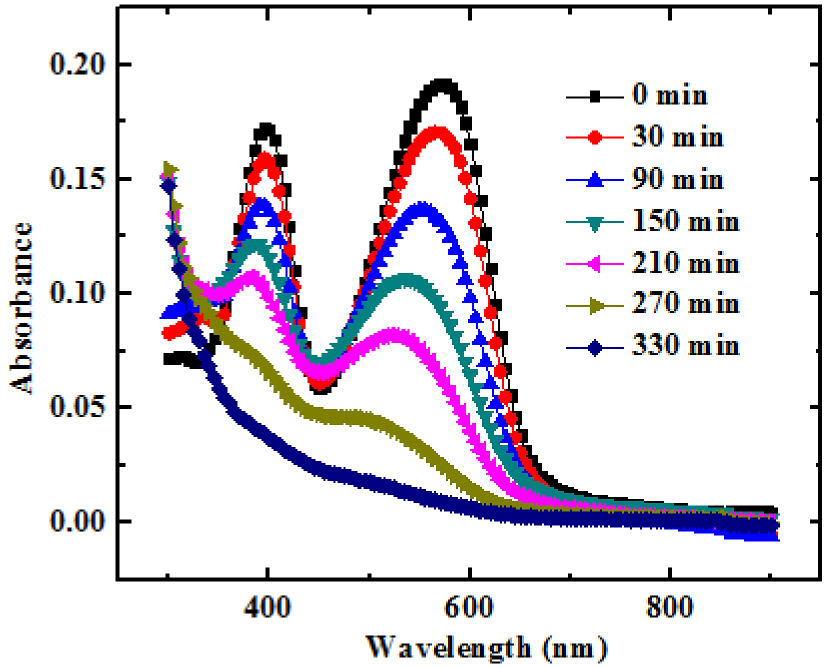

Figure 4.4.2: Changes in the UV-visible absorbance spectra of PCDTBT thin film during photooxidation due to irradiation at ambient air with 100 mW/cm^2 light at different time.

Figure 4.4.3 shows the deviation of absorption maximum of PCDTBT from the absorption maximum of the pristine PCDTBT film as the irradiation time increases, that is, it is the plot of 570 - $\lambda_{\text{Abs. max (t)}}$ *versus* irradiation time, where $\lambda_{\text{Abs. max (t)}}$ is the wavelength (nm) of the maximum absorption at a given irradiation time. With increasing exposure time, the deviation of absorbance maximum from the maximum absorbance of pristine PCDTBT film increased. As known, for conjugated polymers, when conjugation length decreases there will be blue shift in the absorbance maximum. In our case with increasing exposure time, the increased blue shift indicates a continuous reduction of π-conjugation length of PCDTBT.

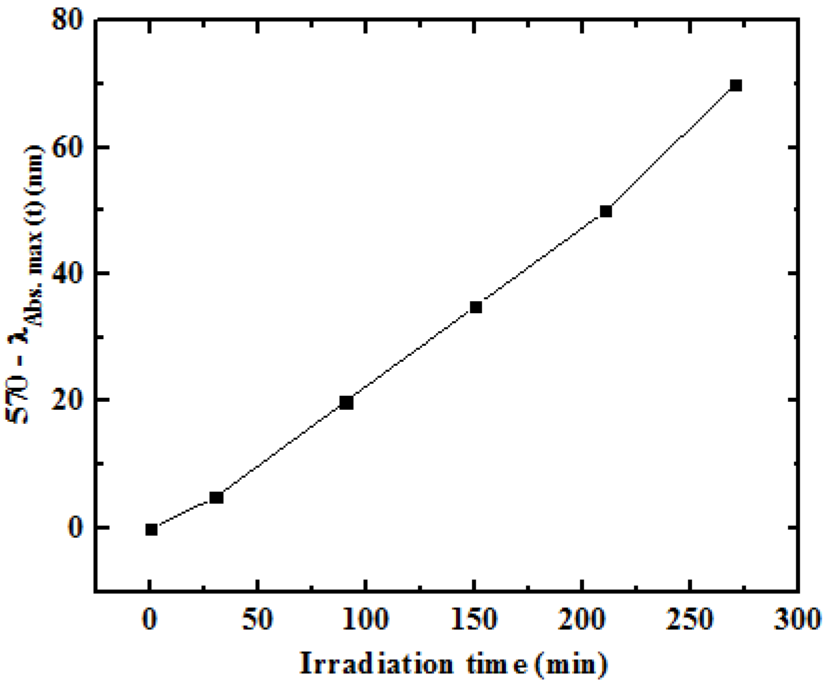

Figure 4.4.3: Deviation of absorption maximum of PCDTBT film from the absorption maximum of the pristine PCDTBT film (570 nm) as the irradiation time increases.

By studying PCDTBT photooxidation products in ambient air by IR and UV spectroscopy, Tournebize et al. [20] clearly demonstrated that PCDTBT oxidation involve the scission of the C-N bond between the carbazole group and the tertiary carbon atom bearing the alkyl side-chain. As stated by the authors the tertiary carbon atom bearing the alkyl side-chain is the preferential site for an alkyl radical attack. The instability of the tertiary carbon atom bearing the alkyl chains is the source of failure of the entire polymer backbone. According to Tournebize et al. [105] recommendation substitution of tertiary carbon atom by a quaternary carbon atom, for instance the replacement of the hydrogen atom by a methyl group, could result in a significant improvement in the stability of PCDTBT under irradiation in the presence of oxygen. According to Tournebize et al. [105] oxidation of the alkyl side chains cannot be solely responsible for the photobleaching of the polymer as these alkyl groups are not involved in the π-conjugation. However, breaking of the thiophene rings of the backbone by the radicals formed along the oxidation of the alkyl side-chains and chain scissions of the backbone results in a loss of π-conjugation and photobleaching of PCDTBT film with the lowering of UV-visible absorbance.

Figure 4.4.4 - Figure 4.4.6 show the UV-visible absorbance spectra of PCDTBT:PC$_{61}$BM, PCDTBT:PC$_{61+71}$BM and PCDTBT:PC$_{71}$BM thin films irradiated under the same condition with pure PCDTBT film. As shown in Figure 4.4.2 after irradiation for 330 min the absorbance of pure film of PCDTBT totally disappeared. Unlike that of pure film of PCDTBT, film of blend of PCDTBT with PC$_{61}$BM, PC$_{71}$BM or mixture of PC$_{61}$BM and PC$_{71}$BM has slower rate of decrease. Simple comparison of results of time dependent UV-visible absorbance in Figure 4.4.2 with Figure 4.4.4 to Figure 4.4.6 show that all fullerene acceptors PC$_{61}$BM, PC$_{71}$BM and the mixture of PC$_{61}$BM and PC$_{71}$BM have stabilized the PCDTBT film compared to the pure film of PCDTBT. In spite of the severe photodegradation observed in the pure PCDTBT film, the blends demonstrated reduced degradation. The stabilizing power of both fullerenes and their mixture will help to improve the working lifetime of PCDTBT based polymer solar cells.

We speculate that like that of P3HT, photodegradation of the PCDTBT is initiated by the excited state of PCDTBT and the inclusion of PCBM stabilizes PCDTBT by quenching the reactive excited states of PCDTBT and by this means slows the photodegradation of PCDTBT [159 - 161]. In addition, radical scavenging properties of fullerene could contribute to the stability of PCDTBT [114, 163].

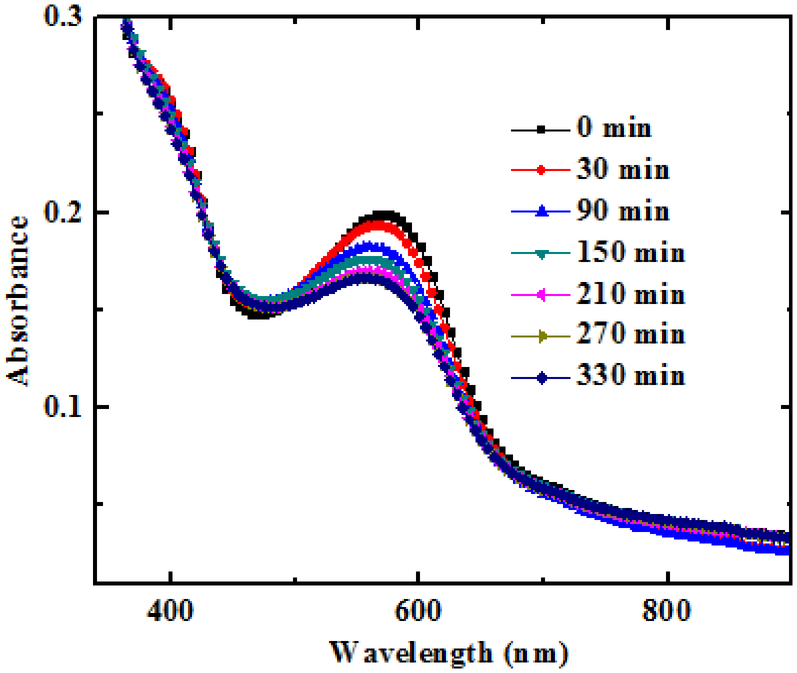

Figure 4.4.4: Changes in the UV-visible absorbance spectra of PCDTBT:PC$_{61}$BM thin film during photooxidation due to irradiation at ambient air with 100 mW/cm^2 light at different time.

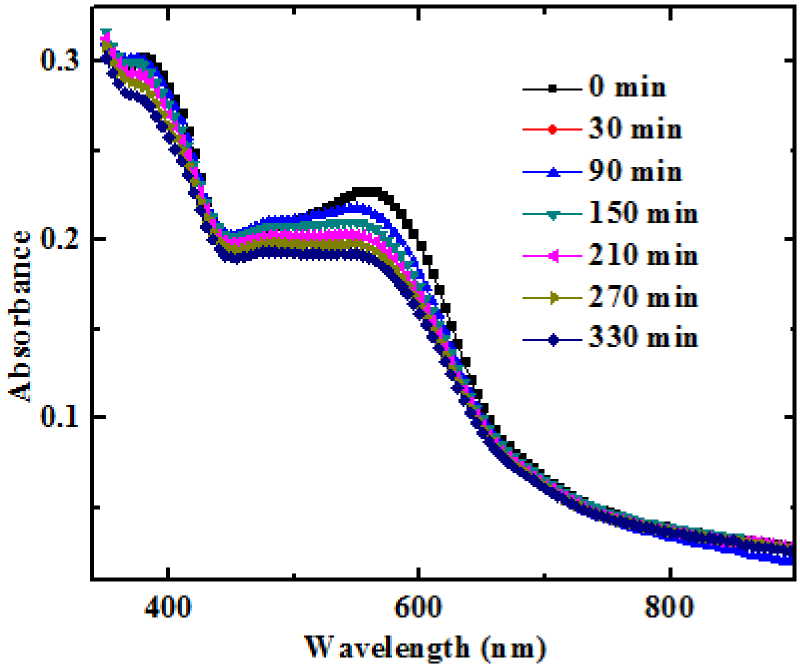

Figure 4.4.5: Changes in the UV-visible absorbance spectra of PCDTBT:$PC_{61+71}BM$ thin film during photooxidation due to irradiation at ambient air with 100 mW/cm^2 light at different time.

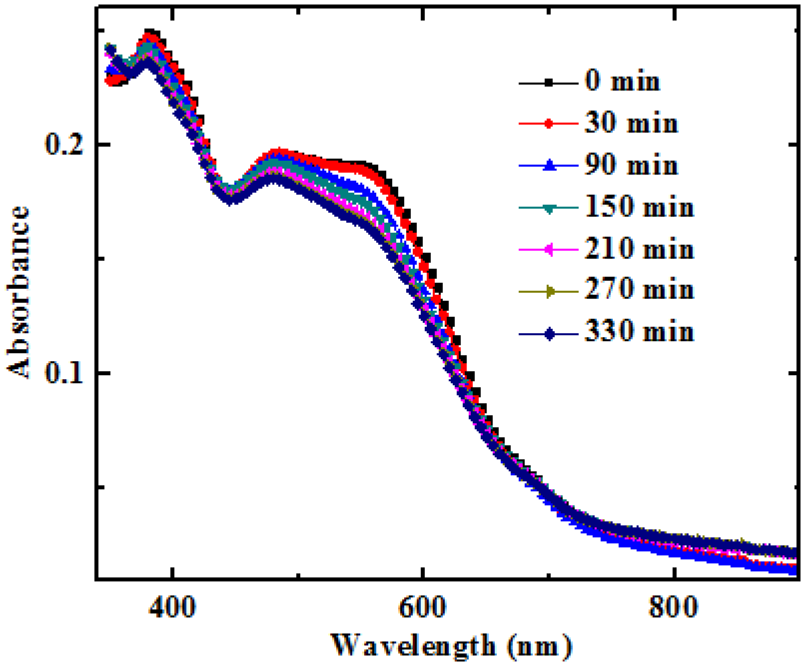

Figure 4.4.6: Changes in the UV-visible absorbance spectra of PCDTBT:$PC_{71}BM$ thin film during photooxidation due to irradiation at ambient air with 100 mW/cm^2 light at different time.

Figure 4.4.7 shows the normalized UV-visible absorbance of the film of PCDTBT (570 nm), PCDTBT:$PC_{61}BM$ (570 nm), PCDTBT:$PC_{61+71}BM$ (555 nm), PCDTBT:$PC_{71}BM$ (555 nm) as a function of photo-oxidation time. Unlike that of pure film of PCDTBT, in case of PCDTBT blended with either $PC_{61}BM$, $PC_{71}BM$ or mixture of $PC_{61}BM$ and $PC_{71}BM$ the absorbance is relatively constant. Under the conditions used in this study, the decrease of the UV-visible absorbance spectra maximum peak resulting from photo-oxidation of the PCDTBT:fullerene blends were considerably slower than that due to the pure film of PCDTBT. The results show the stabilizing power of acceptor fullerenes when mixed with PCDTBT. Both fullerenes and their mixture have almost similar effect in slowing down photooxidation of PCDTBT.

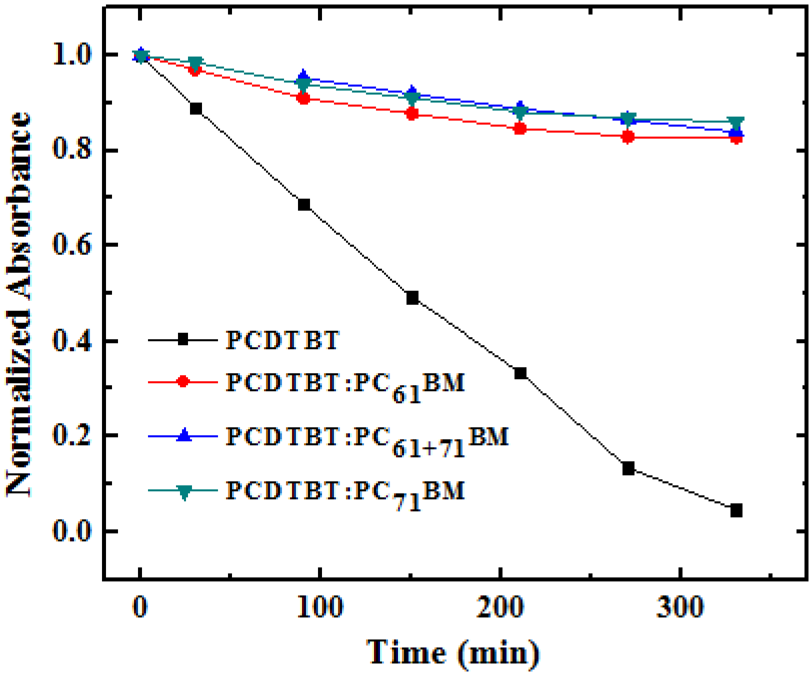

Figure 4.4.7: Normalized UV-visible absorbance of PCDTBT (at 570 nm), PCDTBT:$PC_{61}BM$ (at 570 nm), PCDTBT:$PC_{61+71}BM$ (at 555 nm), PCDTBT:$PC_{71}BM$ (at 555 nm) film as a function of irradiation (100 mW/cm^2 light) time at ambient air.

4.4.3. Photoluminescence measurement

Figure 4.4.8 shows the photoluminescence (PL) spectra of pure film of pristine PCDTBT and after 20 hr of 100 mW/cm^2 light irradiation at ambient air. The decrease of PL spectra after 20 hr of light irradiation shows the reduction of the part of the polymer which is responsible for light absorption. The result of PL spectra is consistent with that of UV-visible absorbance data.

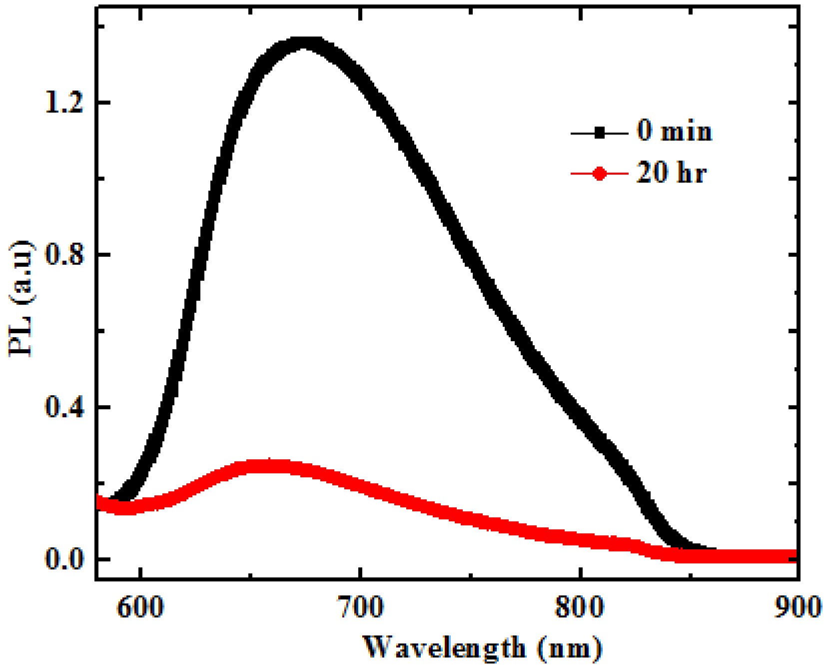

Figure 4.4.8: PL spectra of pristine and 20 hr in ambient air light (100 mW/cm^2) exposed PCDTBT films. The excitation wavelength is 550 nm.

In order to study the degree of charge transfer between PCDTBT and acceptor fullerenes photoluminescence were measured on the film of pure PCDTBT and its blend with the different acceptors. Figure 4.4.9 shows photoluminescence spectra of pure film of PCDTBT and its blend with different fullerenes. As already found out most conjugated polymers show strong photoluminescence [239]. When acceptor fullerene is mixed with the PCDTBT there will be quenching of the photoluminescence due to photoinduced charge transfer from PCDTBT to fullerene. The obtained results show that almost complete quenching of PCDTBT's photoluminescence occurred due to efficient charge transfer from PCDTBT to fullerene.

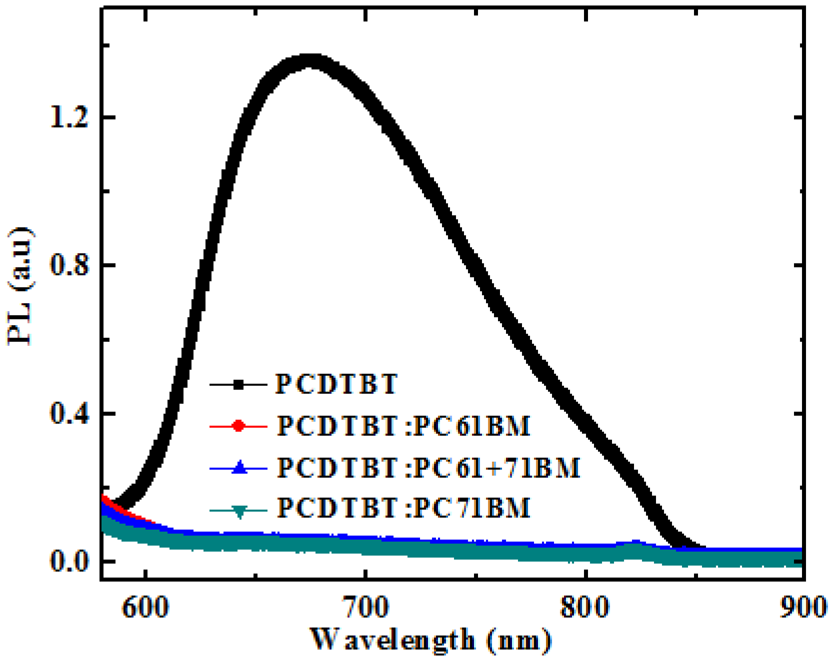

Figure 4.4.9: PL spectra of PCDTBT, PCDTBT:PC$_{61}$BM, PCDTBT:PC$_{61+71}$BM, PCDTBT:PC$_{71}$BM films. The excitation wavelength is 550 nm.

4.4.4. Photovoltaic measurements

Based on the results of UV-visible absorbance data at different irradiation time, the better stabilization of PCDTBT film by PC$_{61}$BM, PC$_{71}$BM and the 1:1 mixture of PC$_{61}$BM and PC$_{71}$BM has motivated us to further investigate the effect of different fullerene acceptors on working lifetime of solar cells made from PCDTBT and the two fullerene acceptors and their 1:1 mixture.

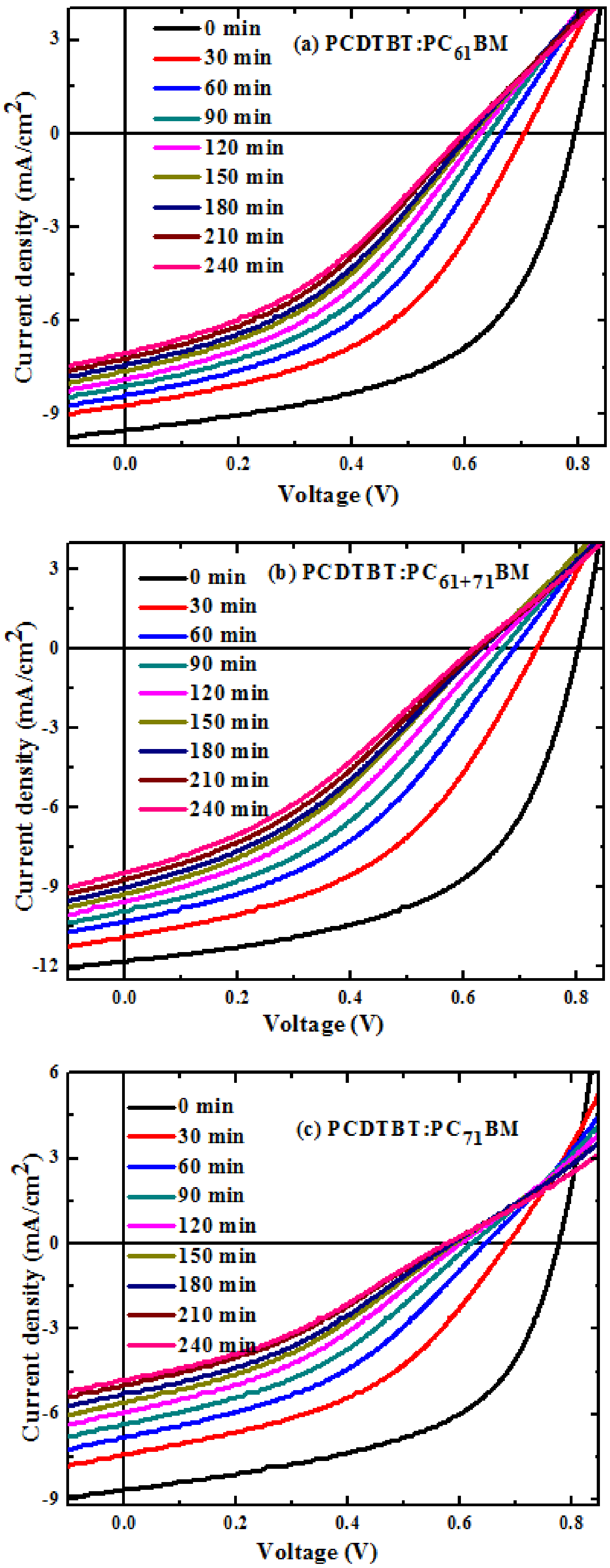

Figure 4.4.10: Current density-voltage (*J*-*V*) curves of bulk heterojunction solar cell made from (a) PCDTBT:PC$_{61}$BM, (b) PCDTBT:PC$_{61+71}$BM and (c) PCDTBT:PC$_{71}$BM and aged at ambient air with irradiation of 100 mW/cm^2 light.

In Figure 4.4.11 normalized η show that the solar cells made from the blend of PCDTBT:$PC_{61}BM$ and PCDTBT:$PC_{61+71}BM$ have slower rate of decay of PCE compared to solar cell made from blend of PCDTBT:$PC_{71}BM$. Based on the result of UV-visible absorbance (Figure 4.4.7) it was expected that the solar cell made from PCDTBT:$PC_{71}BM$ will have similar stability of efficiency with PCDTBT:$PC_{61}BM$ and PCDTBT:$PC_{61+71}BM$ based solar cells. However, the result of Figure 4.4.11 shows that the solar cells made from PCDTBT:$PC_{71}BM$ has inferior stability. PSC based on the blend of PCDTBT:$PC_{61+71}BM$ has intermediate stability. All solar cells show exponential decay of efficiency. The change of UV-visible absorption does not take into account all reactions taking place on PCDTBT as a result of light exposure. For example, reactions such as rearrangements, cross linking or morphological changes on the film cannot be seen on UV-visible absorbance spectra. Therefore, stability of the UV-visible absorption of the blend film alone is not the only criterion to be used as indicator for predicting the working lifetime of PSC. In other word, the results obtained from UV-visible spectroscopy do not explain the dependency of PCDTBT:fullerene solar cells photostability on the type of fullerene acceptors used. Comparing the result from UV-visible spectroscopy and *J-V* measurement implies that the origin of the degradation of the devices is not the photooxidation of active layer.

Based on Figure 4.4.11, the sound conclusion is that it is better to use $PC_{61}BM$ as acceptor to fabricate relatively stable solar cells compared to $PC_{71}BM$. However, if the condition necessitates the use of $PC_{71}BM$, then it is advantageous to use the mixture of $PC_{61}BM$ and $PC_{71}BM$ instead of the pure $PC_{71}BM$.

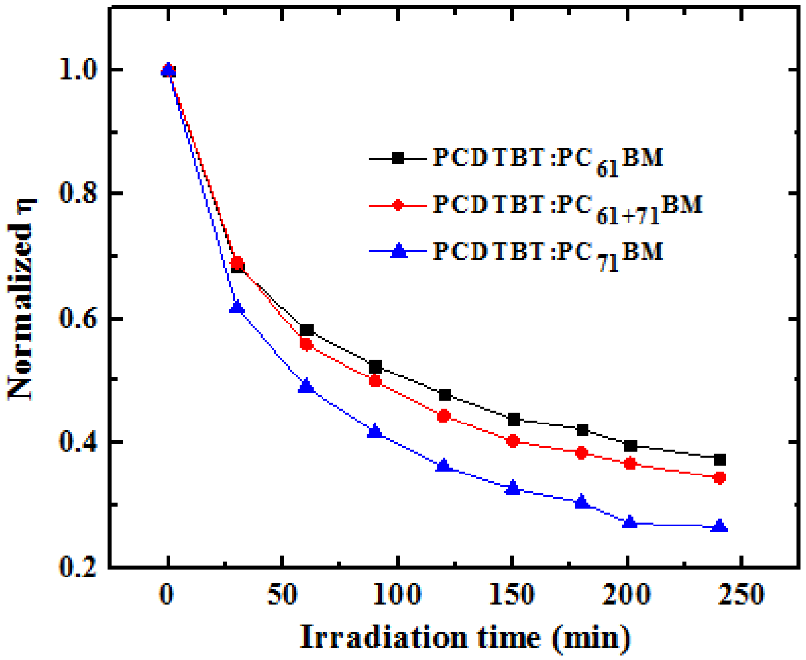

Figure 4.4.11: Normalized *η* of PCDTBT:PC$_{61}$BM, PCDTBT:PC$_{61+71}$BM and PCDTBT:PC$_{71}$BM solar cell as a function of irradiation (100 mW/cm^2) time at ambient air.

Figure 4.4.12 shows that the solar cell made from PCDTBT:PC$_{71}$BM has higher rate of decay of short circuit current-density compared to PCDTBT:PC$_{61}$BM and PCDTBT:PC$_{61+71}$BM based solar cells. Literature report shows that PC$_{71}$BM aggregate easily and form a large domain size of ~100 - 200 nm diameter [15, 240, 241]. Larger domain size of PC$_{71}$BM decreases the PCDTBT:PC$_{71}$BM interface area which is responsible for exciton dissociation. The already formed larger PC$_{71}$BM domain continue to grow with time, decreasing further the polymer:fullerene domain and resulting lower exciton splitting which results in lower short circuit current density.

Light absorption efficiency of the active layer is among the factors that determine short-circuit current density of the device. The result from light irradiation time dependent UV-visible absorption indicates that all films have good absorbance even after 330 min of light exposure. Thus, the cause for decrease of short circuit current density is not the loss of light absorption efficiency, it must be something different and that something has severe impact on the blend of PCDTBT:PC$_{71}$BM compared to the other two. Once light is absorbed J_{sc} is determined by other factors. Morphology is among the other factor. Morphology of the donor:acceptor blend is the interpenetrating network of polymer donor and fullerene acceptor which determines how easily the exciton gets separated before geminate recombination takes place. It is a common knowledge that due to morphology degradation when the interface area between the polymer and fullerene decreases the rate of geminate recombination increases. The increase of geminate recombination reduces short-circuit current density of the solar cell. The higher rate of decrease of J_{sc} of PCDTBT:PC$_{71}$BM solar cell may be caused by the continuous decrease of the interface area between PCDTBT and PC$_{71}$BM due to the further growth of aggregates of PC$_{71}$BM already started as a result of lower solubility of PC$_{71}$BM in DCB.

Non-geminate recombination of free charge at the interface of donor-acceptor or before reaching the electrode has effect on short circuit current density. The non-existence of bi-continuous paths for the transport of charges enhances the probability of non-geminate recombination. As already said, when aggregates of PC$_{71}$BM created there will be domains with high PC$_{71}$BM content and there will be domains with little PC$_{71}$BM and the implication is that there might be no bi-continuous paths for the transport of charge carriers. That is, non-geminate recombination will be enhanced and the result is decrease of short-circuit current density.

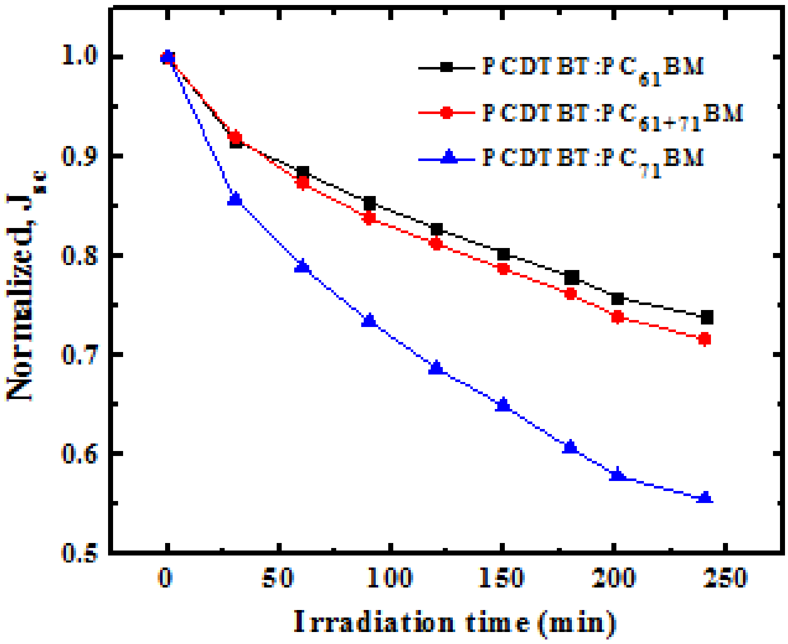

Figure 4.4.12: Normalized J_{sc} of PCDTBT:PC$_{61}$BM, PCDTBT:PC$_{61+71}$BM, PCDTBT:PC$_{71}$BM solar cell as a function of irradiation (100 mW/cm^2) time at ambient air.

Figure 4.4.13 shows the normalized rate of reduction of V_{oc} of the solar cells made from the blend of PCDTBT:PC$_{61}$BM, PCDTBT:PC$_{71}$BM and PCDTBT:PC$_{61+71}$BM. As Figure 4.4.13 shows the normalized open-circuit voltage of the solar cell made from active layer of PCDTBT:PC$_{61+71}$BM has slower rate of decay compared to solar cell made from blend of PCDTBT:PC$_{61}$BM and PCDTBT:PC$_{71}$BM.

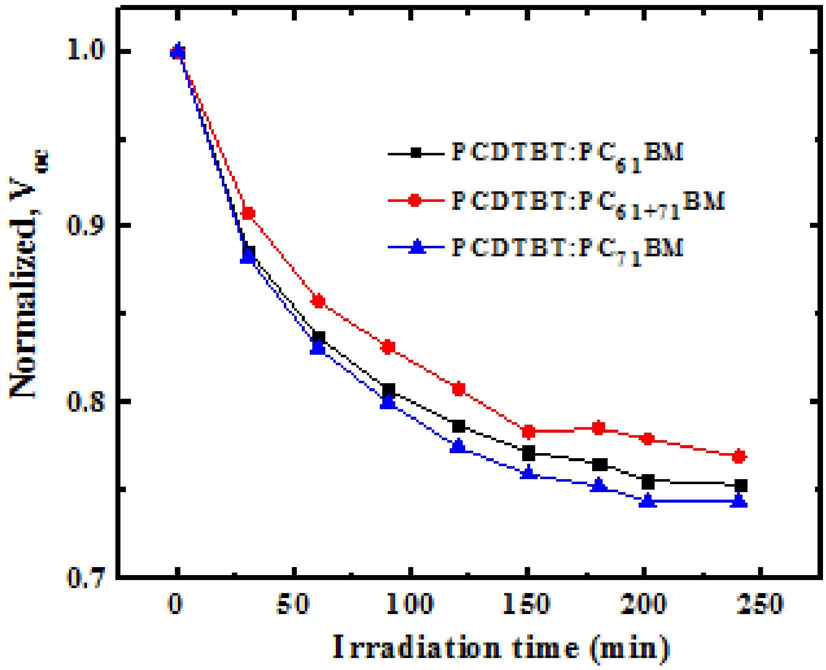

Figure 4.4.13: Normalized V_{oc} of PCDTBT:PC$_{61}$BM, PCDTBT:PC$_{61+71}$BM, PCDTBT:PC$_{71}$BM solar cell as a function of irradiation (100 mW/cm^2 light) time at ambient air.

Figure 4.4.14 shows the normalized rate of reduction of *FF* of the solar cells made from the blend of PCDTBT:PC$_{61}$BM, PCDTBT:PC$_{71}$BM and PCDTBT:PC$_{61+71}$BM. As Figure 4.4.14 shows the normalized *FF* of the solar cell made from active layer of PCDTBT:PC$_{61}$BM has slower rate of decay compared to solar cell made from blend of PCDTBT:PC$_{61+71}$BM and PCDTBT:PC$_{71}$BM. The decrease of *FF* is related with appreciable increase in series resistance of the device due to light exposure. In relative term the device made from PCDTBT:PC$_{61}$BM has better *FF* after aging the device by light exposure.

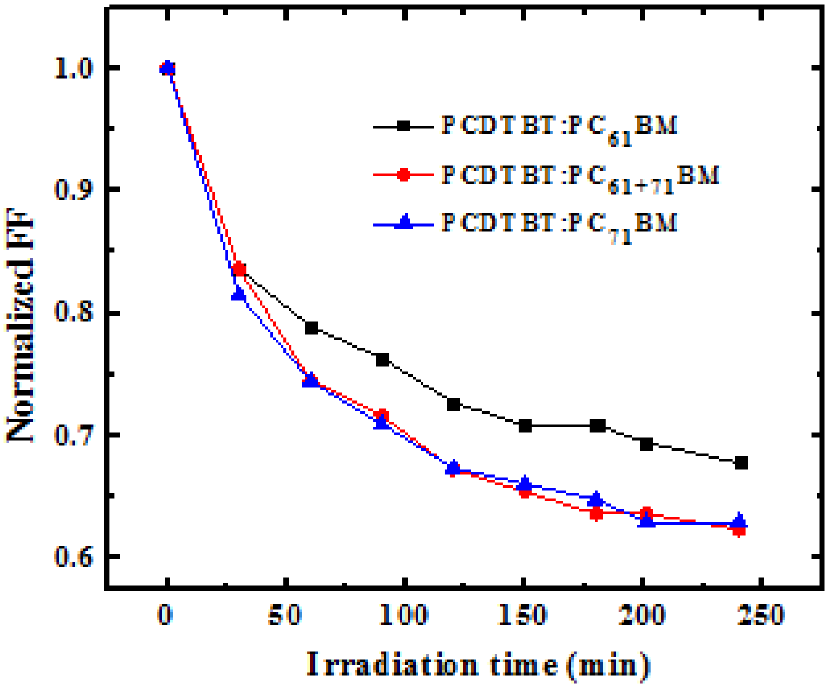

Figure 4.4.14: Normalized *FF* of PCDTBT:$PC_{61}BM$, PCDTBT:$PC_{61+71}BM$, PCDTBT:$PC_{71}BM$ solar cell as a function of irradiation (100 mW/cm^2 light) time at ambient air.

Figure 4.4.15 show the normalized series resistance of solar cells made from the blend of PCDTBT:$PC_{61}BM$, PCDTBT:$PC_{61+71}BM$ and PCDTBT:$PC_{71}BM$ as a function of 100 mW/cm^2 light irradiation time. As Figure 4.4.15 shows PCDTBT:$PC_{61}BM$ and PCDTBT:$PC_{61+71}BM$ based solar cells have slower rate of increase of series resistance compared to solar cell made from blend of PCDTBT:$PC_{71}BM$. The increase of series resistance implies an increase in the resistance of the active layer or an increase in the resistance at the electrodes. The main impact of series resistance is reduction of *FF* of the device. The results of series resistance measured for PCDTBT:$PC_{61}BM$ solar cell is in agreement with the trend of *FF*.

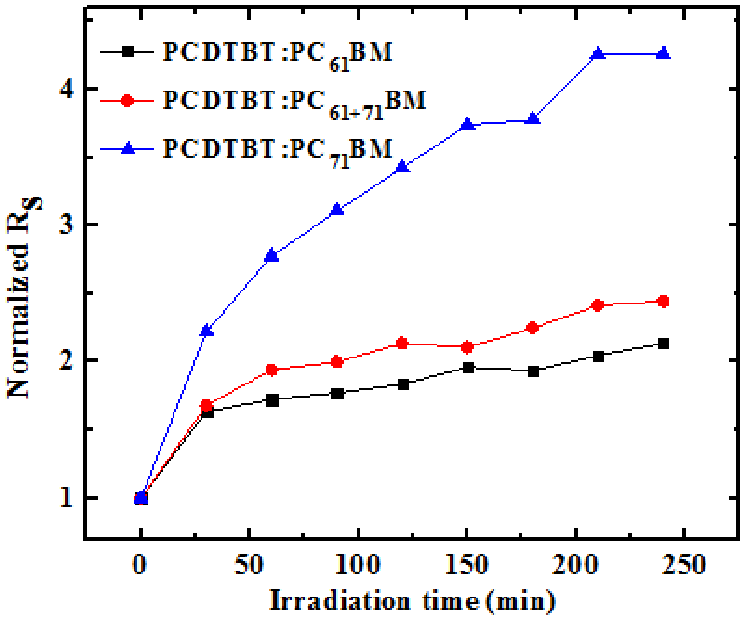

Figure 4.4.15: Normalized R_s of PCDTBT:PC$_{61}$BM, PCDTBT:PC$_{61+71}$BM, PCDTBT:PC$_{71}$BM solar cell as a function of irradiation (100 mW/cm^2 light) time at ambient air.

4.4.5. Conclusions

We have studied the effect of light irradiation at ambient condition on the photostability of the film of PCDTBT, PCDTBT:PC$_{61}$BM, PCDTBT:PC$_{61+71}$BM and PCDTBT:PC$_{71}$BM. We have also studied the effect of light irradiation on the solar cells made from PCDTBT:PC$_{61}$BM, PCDTBT:PC$_{61+71}$BM and PCDTBT:PC$_{71}$BM. Unlike that of pure film of PCDTBT, in case of PCDTBT blended with either PC$_{61}$BM, PC$_{71}$BM or mixture of PC$_{61}$BM and PC$_{71}$BM the UV-visible absorbance is relatively constant. The results show the stabilizing power of acceptor fullerenes when mixed with PCDTBT. Both fullerenes and their mixture have almost similar effect in slowing down photooxidation of PCDTBT. Decrease of the UV-visible absorbance of PCDTBT film highlights the close relationship between the effects of irradiation by light on the chemical structure of PCDTBT and the reduction in its π-conjugation length.

The results from *J-V* measurement indicates that the solar cells made from PCDTBT:PC$_{61}$BM and PCDTBT:PC$_{61+71}$BM have better stability under light exposure in ambient air compared to the device based on PCDTBT:PC$_{71}$BM. Therefore, to fabricate relatively stable solar cells it is better to use PC$_{61}$BM or 1:1 mixture of PC$_{61}$BM and PC$_{71}$BM instead of pure PC$_{71}$BM as acceptor.

4.5. Investigation on the Effects of Additive on Photovoltaic Performance and Photostability of PCDTBT:$PC_{71}BM$ Solar Cells

4.5.1. Background

In PSCs, morphology of active layers plays a decisive role in determining power conversion efficiency because charge carrier generation, recombination and transport are all affected by morphology of the active layers formed after spin casting [15, 60, 64, 155, 242 - 245]. As we know in PSCs excitons are dissociated into free electrons and holes at the interface between donor polymer and acceptor fullerene [246]. To get reasonable PCE the electrons and holes which are formed from dissociated excitons must be transported and should reach the appropriate extracting electrodes and this requires bi-continuous paths of donor and acceptor phases. Hence, the optimum morphology of the active layer for PSCs is a trade-off between charge carrier generation and transport to the corresponding electrodes. The problem is that the ideal morphology of the active layers which strongly depends on the solubility and miscibility of donor polymer and acceptor fullerenes cannot be formed during spin coating of the active layer. To alleviate the problem and to improve PCE of PSCs it is necessary to tune the morphology of the active layers and the following treatments are in use by researchers working in the field. They are thermal annealing, using mixed solvents and adding suitable additives to the main solvent [15, 57, 60, 247, 248].

In the previous section (section 4.4) we have seen that the stability of power conversion efficiency of light illuminated PCDTBT:$PC_{71}BM$ based solar cells are inferior compared to $PC_{61}BM$ and mixture (1:1) of $PC_{61}BM$ and $PC_{71}BM$ based PCDTBT solar cells. For efficient PSCs the BHJ donor:acceptor domain length scale of $\leq$ 10 nm with good polymer-fullerene miscibility is highly required. However, literature reports tell us that $PC_{71}BM$ aggregate easily and form a large domain size of ~100 - 200 nm diameter [15, 240, 241]. In order to solve the problem of the aggregation of $PC_{71}BM$ in polymer:fullerene systems, additives, especially di(R)alkanes with various functional groups (R), have been added to the BHJ blends solution [249] and they resulted in significant increase of PCE. In literatures related with PSCs the use of additives for tuning the morphology of active layers is very common and resulted in improvement of PCEs [15, 250]. It is becoming an attractive method for morphology control. However, little attention is given about the consequence of processing additives on the working lifetime of real device. Therefore, main objective of this study is revealing the effect of additive on the working lifetime of PSC aged by light exposure.

The solvent additive diiodomethane (DIM) is a commonly used additive and the use of it has enhanced PCE in PSCs based on different polymers [251]. As observed in our laboratory by PhD student Bedasa Abdisa, the addition of 3% of diiodomethane (DIM) as processing additives to PCDTBT:$PC_{71}BM$ in 1, 2 dichlorobenzene (DCB) has improved the power conversion efficiency. PCDTBT is insoluble in DIM while $PC_{71}BM$ is soluble. The reason for the better solubility of $PC_{71}BM$ in the presence of DIM is that the iodine atom bears a partial negative charge and $PC_{71}BM$ is electrodeficient which results in strong interactions with each other [252]. Therefore, when DIM is mixed with the main solvent, it will increase the solubility of $PC_{71}BM$ and this results in optimal mixing of PCDTBT and $PC_{71}BM$ and better morphology when the film of PCDTBT:$PC_{71}BM$ is formed by spin casting. No question that the optimal mixing will give improved PCE compared to a device processed without DIM.

In section 4.4, based on literature and our experimental results we have speculated that it is the lower solubility of $PC_{71}BM$ in DCB contributed for morphology degradation and decay of power conversion efficiency. Lower solubility of $PC_{71}BM$ in DCB result in larger phase separation with $PC_{71}BM$-rich and PCDTBT-rich phases. When exposed to light at ambient air the already started phase separation increases in size further. Therefore, any means which improves the solubility of $PC_{71}BM$ in DCB is expected to improve the morphology (decrease large phase separation between $PC_{71}BM$-rich and PCDTBT-rich phases) and the stability of the working device based PCDTBT and $PC_{71}BM$ blend. Therefore, addition of DIM to the main solvent is expected to improve the stability of PCDTBT:$PC_{71}BM$ solar cells by improving the morphology and contact to top electrode. In order to confirm the hypothesis on the effect of DIM on stability of PCDTBT:$PC_{71}BM$ based solar cells, we have fabricated the real device with the blend containing no DIM and 3% DIM and studied the J-V characteristics under light irradiation. We also used impedance spectroscopy and UV-visible spectroscopy to find out the effect of DIM on the photostability of PCDTBT:$PC_{71}BM$ based device.

4.5.2. UV-visible absorbance measurement

Figure 4.5.1 shows UV-visible absorbance spectra of PCDTBT:$PC_{71}BM$ film with and without 3% DIM. As we can see on the Figure 4.5.1 there is no much difference between the UV-visible absorbance spectra of PCDTBT:$PC_{71}BM$ films with and without DIM. However, we can see a little lower absorption intensity at high energy region and a little higher absorption intensity at low energy region for the film processed with DIM.

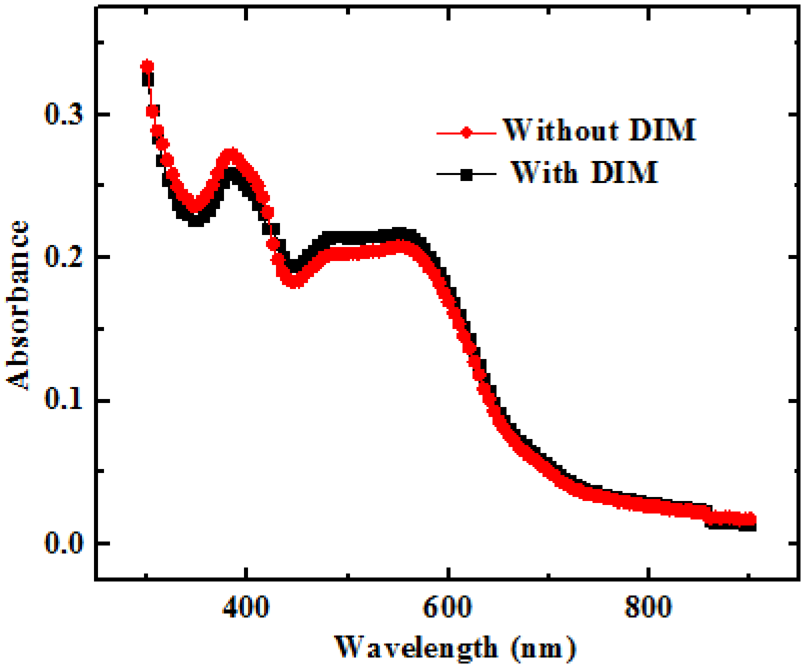

Figure 4.5.1: UV-visible absorption spectra of PCDTBT:$PC_{71}BM$ blend films prepared with and without DIM.

Figure 4.5.2 shows the variation of normalized UV-visible absorbance of BHJ films of PCDTBT:$PC_{71}BM$ processed with and without DIM. The observation indicates that with increasing light exposure time, the BHJ films of PCDTBT:$PC_{71}BM$ processed with DIM has lower stability or higher rate of degradation compared to the BHJ film without DIM. As a consequence, it is very important to study the effect of DIM on the stability of PCDTBT:$PC_{71}BM$ based device under light exposure in ambient air. The higher rate of photodegradation of the film of PCDTBT:$PC_{71}BM$ with DIM may be explained as follows. Due to solubility of $PC_{71}BM$ in DIM, the addition of DIM produces homogeneous morphology between PCDTBT and $PC_{71}BM$. The homogeneous morphology would make more PCDTBT exposed to air, which is more easily degraded by O_2 and H_2O molecules compared to the BHJ layer without DIM.

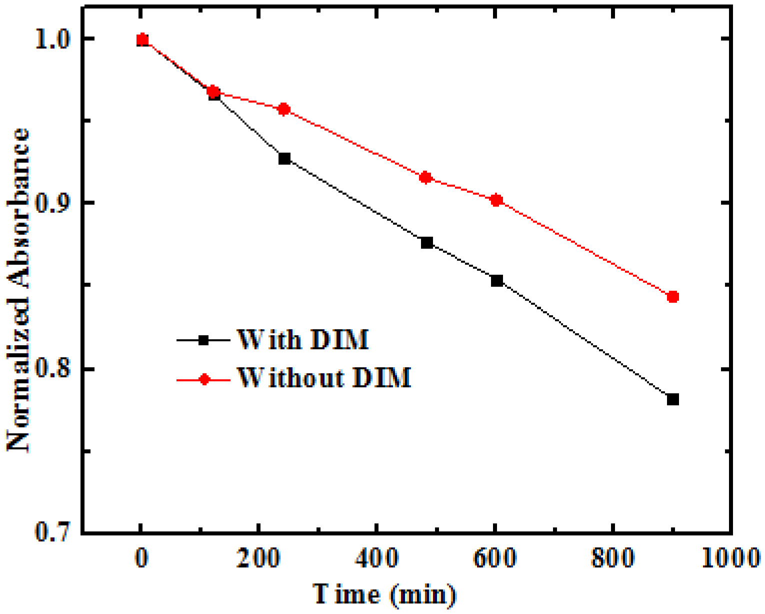

Figure 4.5.2: Normalized UV-visible absorbance of PCDTBT:$PC_{71}BM$ processed with and without DIM as a function of irradiation (100 mW/cm^2 light) time at ambient air.

4.5.3. Current density-voltage characteristics

The current density-voltage characteristics (*J*-*V*) of the PCDTBT:$PC_{71}BM$ devices processed with and without 3% DIM are shown in Figure 4.5.3. PCDTBT:$PC_{71}BM$ solar cell without DIM (reference cell) shows a PCE of 2.77%, J_{sc} = 8.8 mA/cm^2, FF = 46%, V_{oc} = 691 mV and R_s = 70 Ω.cm^2 whereas, PCDTBT:$PC_{71}BM$ solar cell processed with 3% DIM shows a PCE of 3.42%, J_{sc} = 10.65 mA/cm^2, FF = 47%, V_{oc} = 690 mV and R_s = 50 Ω.cm^2. For the solar cell processed with 3% DIM, short circuit current density has increased by 21% and series resistance has reduced by 34%. As the result shows PCDTBT:$PC_{71}BM$ solar cell processed with 3% DIM has better PCE with improved short-circuit current density and reduced series resistance.

For the solar cell without DIM the formation of heavily aggregated $PC_{71}BM$ results in lower intercalation into PCDTBT domains, thereby lowering the PCDTBT-$PC_{71}BM$ interface area and exciton dissociation. However, when DIM is used, it selectively dissolves $PC_{71}BM$ aggregates promoting formation of smaller domains and greater PCDTBT-$PC_{71}BM$ interpenetration within the film and optimizing the PCDTBT-$PC_{71}BM$

interface and which in turn resulting in higher exciton splitting. The existence of bi-continuous paths for the transport of holes and electrons facilitate charge carrier transport. The improved dissociation of excitons and good charge collection efficient leads to better power conversion efficiency.

The increased short-circuit current density for PCDTBT:$PC_{71}BM$ device processed with 3% DIM can be explained as follows. DCB is not the best solvent for $PC_{71}BM$. When $PC_{71}BM$ is dissolved in DCB large $PC_{71}BM$ grains are formed [64, 252]. When PSC is fabricated using $PC_{71}BM$ as acceptor, the large $PC_{71}BM$ grains could hinder the exciton migration to the D/A interface, thereby limiting the charge separation in the BHJ layer [253]. Additions of solvent processing additives affect the size of fullerene and enhance bi-continuous channels formation within the BHJ composite resulting in higher J_{sc} [250, 254 - 257]. When DIM is mixed with the DCB, $PC_{71}BM$ grain boundary size is reduced in the BHJ active layer. As $PC_{71}BM$ aggregates are diminished there will be higher interface area between PCDTBT and $PC_{71}BM$ and better bi-continuous channels for charge carrier transport and this result in higher J_{sc}. Therefore, the addition of DIM is responsible for higher J_{sc} relative to the device processed without DIM.

When DIM is added the reduced value of R_s indicates that the morphology induced by DIM made ease charge carrier transport in the active layer of PCDTBT:$PC_{71}BM$. Therefore, improved J_{sc} combined with decreased R_s mean the morphology of the active layer processed with 3% DIM permitted more efficient charge carrier generation and transport to the electrodes compared to the device processed without DIM.

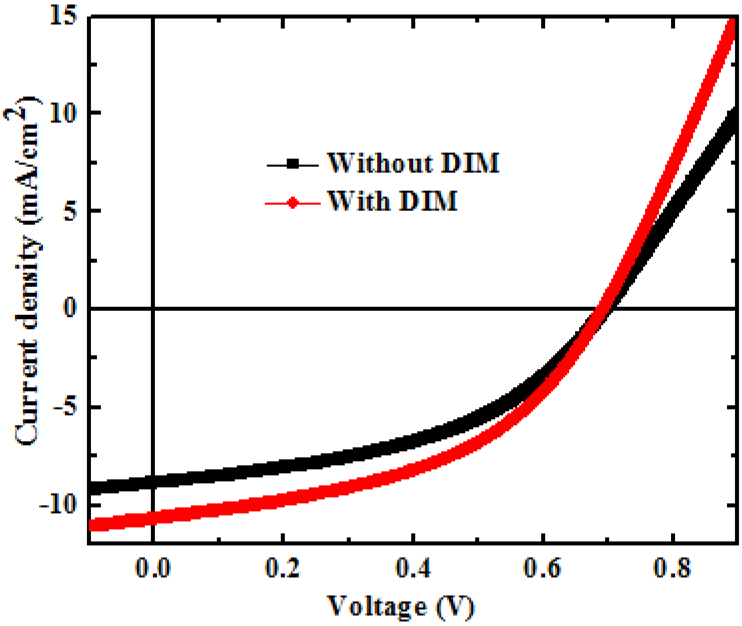

Figure 4.5.3: Current-voltage characteristics of PCDTBT:PC$_{71}$BM solar cells processed without and with 3% DIM.

4.5.4. Effect of DIM on charge carrier generation

In case of a weak voltage dependence of the photocurrent density and negligible non-geminate recombination at high reverse bias, information about charge carrier generation can be obtained directly from the *J-V* curve. The solar cell total current density (*J*) can be expressed as a combination of the dark diode current density (J_{dark}) and the photocurrent density (J_{ph}) [64, 223]:

$$J = J_{dark} - J_{ph} \tag{28}$$

$$J(V) = J_{dark}(V) - qLG(I)P_C(I,V) \tag{29}$$

where q is the elementary charge, L is the thickness of the active layer, $G(I)$ is the generation rate of bound electron-hole pairs per unit volume and $P_c(I, V)$ is the charge collection probability [64, 258].

From Equation (28) and Equation (29), photocurrent density (J_{ph}) of polymer solar cell is given by the following equation:

$$J_{ph} = qLG(I)P_C(I,V) \tag{30}$$

When sufficiently large reverse bias is applied, $P_c(I, V) = 1$ since the internal field is large enough to sweep out all the charge carriers to the respective electrodes (non-geminate recombination can be neglected) and Equation (30) becomes:

$$J_{sat} = qLG \tag{31}$$

From Equation (31) generation rate is given by:

$$G = \frac{J_{sat}}{qL} \tag{32}$$

From the measured saturated current density at -1.0 V (J_{sat}) the generation rates for the PCDTBT:PC$_{71}$BM solar cells processed without and with 3% DIM are calculated. For the device processed with 3% DIM, G = 1.0 x 10^{22} $\text{cm}^{-3}\text{s}^{-1}$ where as for the device processed without 3% DIM, G = 1.3 x 10^{21} $\text{cm}^{-3}\text{s}^{-1}$. A lower generation rate for devices without 3% DIM is in agreement with a large domain phase separation in PCDTBT:PC$_{71}$BM blend because of lower solubility of PC$_{71}$BM in DCB. When the interface area is lower, excitons undergo geminate recombination because they may not find interface area for dissociation in their lifetime. Excitons not able to find interface area undergo geminate recombination. However, when there is higher interface area, the excitons can get interface area within their diffusion length and lifetime and get dissociated. The higher generation rate for the device processed with 3% DIM indicates that the effect of DIM is to suppress the formation of the large fullerene clusters, leading to a smaller length scale of the polymer and fullerene phases and an increase of the effective interfacial area for efficient exciton splitting. The results obtained from our measurements are consistent with experimental results reported on the effect of additives by different groups [240, 241, 259].

In order to understand the origin of higher performance of PCDTBT:PC$_{71}$BM solar cell with 3% DIM, we have investigated the recombination mechanisms in PCDTBT:PC$_{71}$BM solar cell with and without 3% DIM under different illumination intensities. Since exciton quenching of the bulk heterojunction is strongly related to the charge recombination, investigation of the light intensity dependence of the J-V characteristics helps to probe the dominant recombination mechanism that affects device performance. Therefore, recombination kinetics can be illustrated by the investigation of variations of J_{sc} as the function of the light intensity. Figure 4.5.4 presents the light-intensity dependence of J_{sc} for PCDTBT:PC$_{71}$BM solar cell processed with and without DIM. Figure 4.5.4 reveals that for PCDTBT:PC$_{71}$BM solar cell without DIM, J_{sc} has slight non-linear dependence on light intensity. However, PCDTBT:PC$_{71}$BM solar cell with DIM show good linear dependence on light intensity. The dependence of J_{sc} on light intensity is given by the power law [64, 260]:

$$J_{sc}\ \alpha\ I^{\beta} \tag{33}$$

where I is the light intensity. In principle, the observance of $\beta = 1$ indicates that all the charge carriers have been removed prior to recombination (i.e, bimolecular recombination is negligible (maximum carrier sweep out) [64, 223, 261]. Deviation from $\beta = 1$ is attributed to non-geminate recombination [257] and space charge effects [262, 263].

For PCDTBT:PC$_{71}$BM solar cell without DIM, $\beta = 0.6$ corresponding to the power law fit of Equation (33). However, for PCDTBT:PC$_{71}$BM solar cell with DIM $\beta = 0.8$ is observed. Based on the obtained values of β it is possible to expect higher non-geminate recombination in device processed without DIM. For the device processed with DIM β value better close to unity undoubtedly shows that bimolecular/non-geminate recombination is appreciably suppressed relative to the device without DIM. That is, charge carrier sweep-out is the most effective in device where DIM was used. The obtained results prove that 3% DIM can be used to enhance charge carriers generation and transport which result in improved PCE [264].

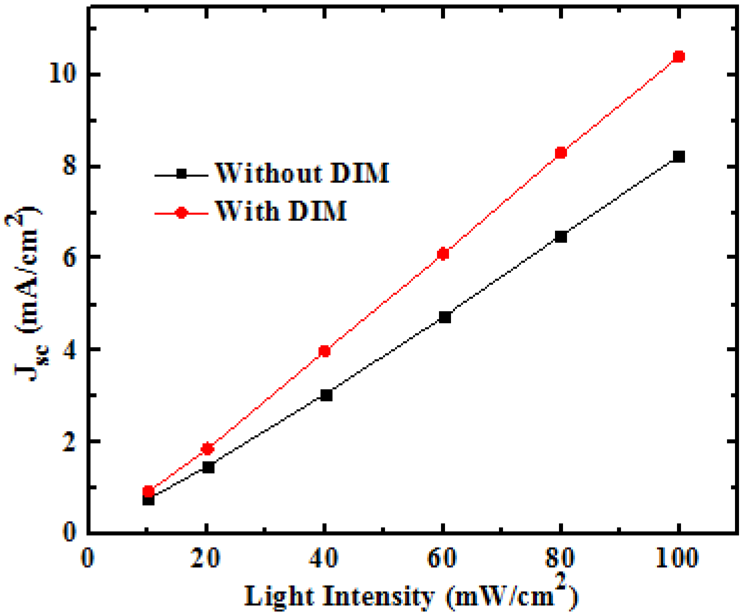

Figure 4.5.4: J_{sc} *versus* light intensity for PCDTBT:PC$_{71}$BM solar cell processed without and with DIM.

4.5.5. Effect of DIM on the stability of PCDTBT:PC$_{71}$BM solar cells

In order to study the effect of DIM on the stability of PCDTBT:PC$_{71}$BM solar cells exposed to continuous illumination of 100 mW/cm^2 light, solar cells processed with and without DIM were fabricated in open air and their PCE were compared. The PCDTBT:PC$_{71}$BM solar cells processed without and with 3% DIM were illuminated with 100 mW/cm^2 light while taking the J-V measurements and the J-V curve is given in Figure 4.5.5. Qualitative analysis of Figure 4.5.5 implies that for both kinds of devices PCE, J_{sc}, FF and V_{oc} decreased with increasing irradiation time and this can be related with bleaching or/and the degradation of the morphology, the active layer-electrode contact and oxidation of metal electrode etc. Bleaching of the polymer results in lower absorption of photons. When morphology degrades it results in an increased rate of exciton and free charge carrier recombination, decreased charge carrier transport to the electrodes and reduced PCE of the device.

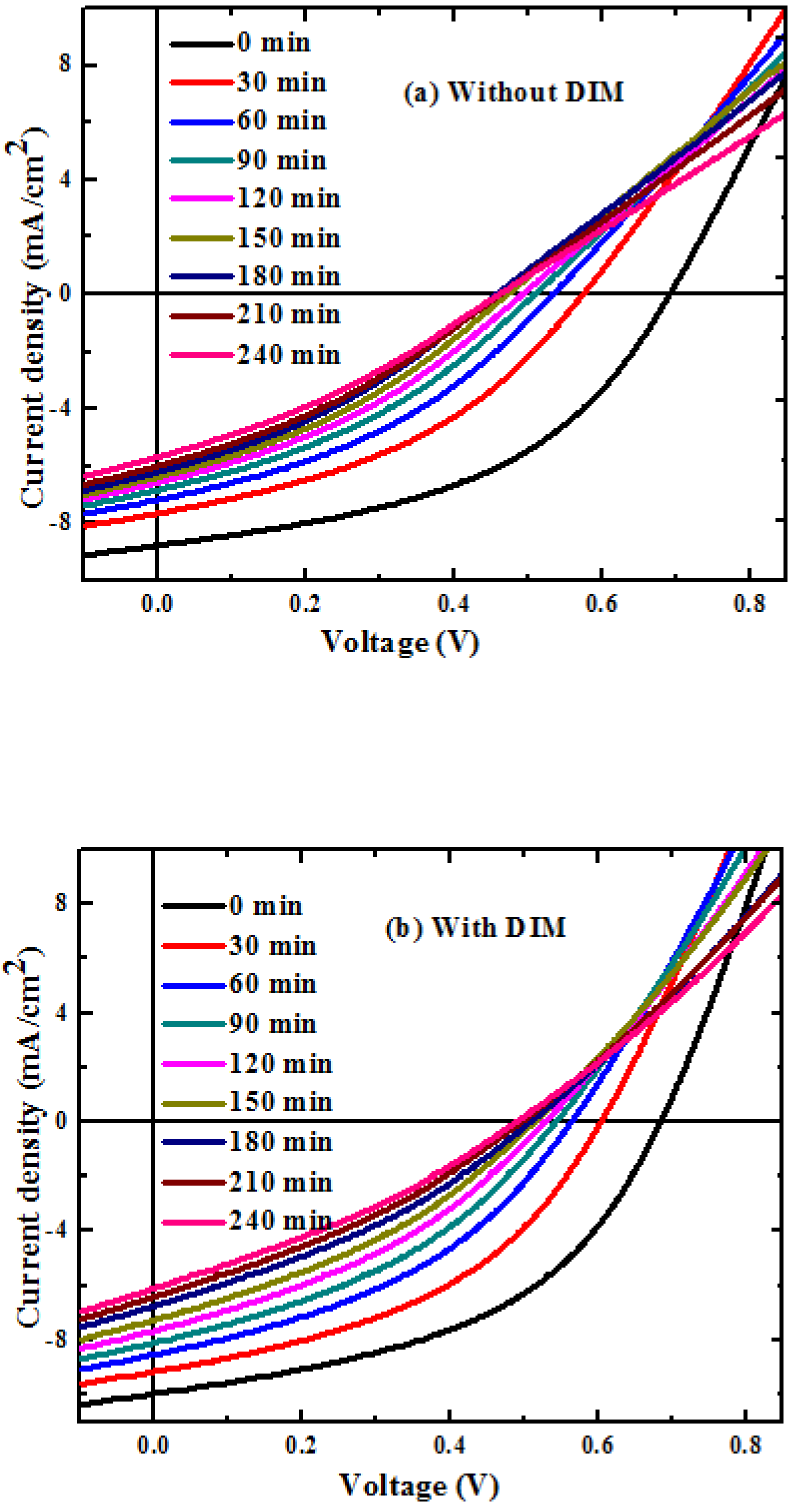

Figure 4.5.5: The *J-V* curves of the PCDTBT: $PC_{71}BM$ solar cell processed without (a) and (b) with 3% DIM as a function of light irradiation (100 mW/cm^2) time at ambient air.

The normalized values of PCE are given in Figure 4.5.6. As shown in Figure 4.5.6, there is relatively lower rate of decrease of PCE for the device processes with 3% DIM compared to the reference device until irradiation time of 210 min. The results demonstrated that the morphology of PCDTBT:$PC_{71}BM$ film is controlled by the addition of 3% DIM and hence improved the stability of the power conversion efficiency of the devices. Under light irradiation, device performance stability in PCDTBT:$PC_{71}BM$ film treated with DIM is due to the improved solubility and reduction of aggregation of $PC_{71}BM$ in the PCDTBT:$PC_{71}BM$ BHJ film which facilitated the efficient exciton dissociation and charge transport to the electrode. In the absence of DIM, aggregation of $PC_{71}BM$ already formed due to lower solubility of $PC_{71}BM$ continuously grow larger and larger and results in higher rate of geminate and non-geminate recombinations, however, when there is DIM it hinders aggregation of $PC_{71}BM$ at least for some time.

On the other hand, beyond 210 min, for the device processed with 3% DIM the performance drops on the same fashion with the reference device indicating that the advantage obtained from DIM begins to fade away with time. The reduction of photovoltaic performance is due to inadequate morphology for the efficient dissociation of excitons, charge transportation and extraction [265]. The obtained result show that in the long run at ambient condition and continuous irradiation PCDTBT:$PC_{71}BM$ solar cell processed with 3% DIM has lower environmental stability.

Wang et al. [266] found out that bilayer PSCs shows more stable performance than the BHJ PSCs in air condition due to the shielding effect of PCBM layer. PTB7 polymer processed with diiodooctane (DIO) showed an increased PTB7 on the film surface because large aggregated $PC_{71}BM$ domains dissolved and integrated into PTB7 domains [15]. Because of exposure of the polymer to air, PSCs processed with additives undergo degradation faster than the unprocessed device [175, 267 - 269]. Based on literature results it may be the case that BHJ film of PCDTBT:$PC_{71}BM$ processed with DIM show an increased PCDTBT content on the film surface because large aggregated $PC_{71}BM$ domains dissolved and integrated into PCDTBT domains. Consequently, in the long run BHJ layer of PCDTBT:$PC_{71}BM$ processed with DIM degraded more easily in the air compared to the device without DIM.

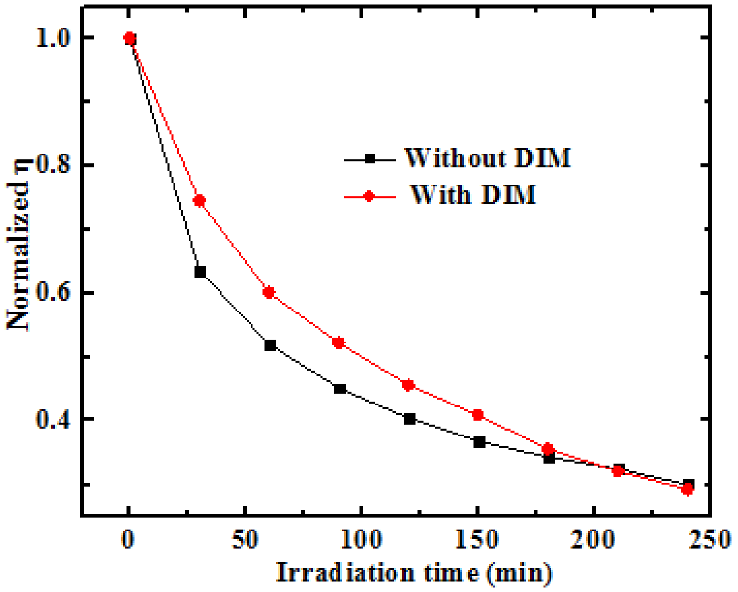

Figure 4.5.6: Normalized η of the PCDTBT:PC$_{71}$BM solar cell processed without and with 3% DIM as a function of irradiation (100 mW/cm^2) time at ambient air.

The rates of decrease of normalized J_{sc} for devices with and without DIM are shown in Figure 4.5.7. From the time of fabrication until irradiation time of 150 min. the device with DIM had lower rate of decrease of $J_{sc,}$ however after 150 min the rate of decay of J_{sc} had increased in comparison with the device without DIM. The result implies that at ambient condition and continuous irradiation for longer time, the solvent additive DIM contributes for the decrease of J_{sc} of the solar cell and it has harmful effect on the PCE.

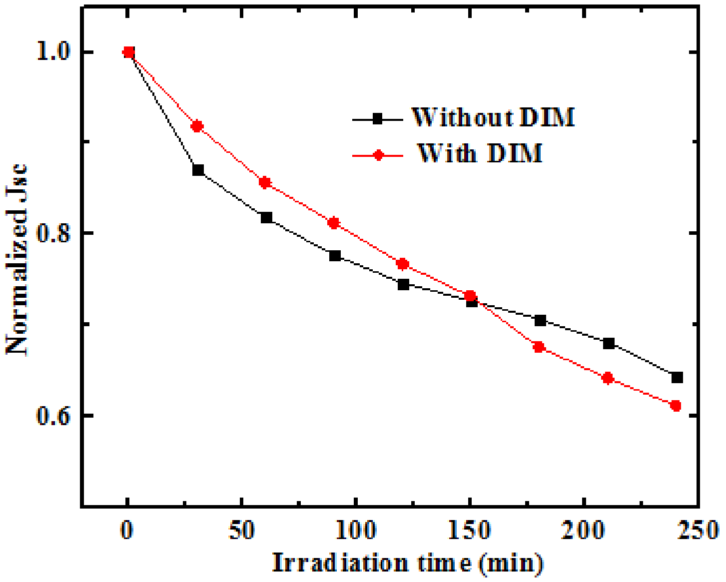

Figure 4.5.7: Normalized J_{sc} of the PCDTBT:PC$_{71}$BM solar cell processed without and with 3% DIM as a function of irradiation (100 mW/cm^2) time at ambient air.

Figure 4.5.8 shows measurements of the dark current, solar cell current, dark current minus solar cell current and dark current minus reverse saturation current of PCDTBT:PC$_{71}$BM solar cell processed with 3% DIM and illuminated with solar illumination intensity of 40 mW/cm^2 in ambient air. In Figure 4.5.8 dark current minus reverse saturation current (J_{sat}) curve is the estimate of the response that the solar cell would have in the absence of any recombination. In Figure 4.5.8 the curve of dark current minus reverse saturation current shows that recombination mainly reduces the fill factor and open-circuit voltage of the solar cell.

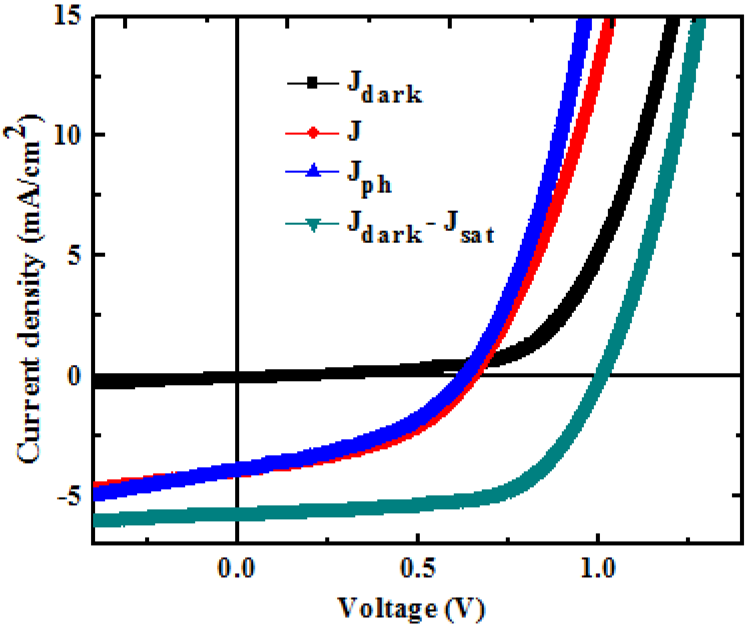

Figure 4.5.8: Measurements of the dark current, solar cell current, dark current minus solar cell current and dark current minus reverse saturation current of PCDTBT:PC$_{71}$BM solar cell processed with 3% DIM and illuminated with solar illumination intensity of 40 mW/cm^2 in ambient air.

Figure 4.5.9 shows that the *FF* of both devices processed with and without DIM decreased continuously upon light irradiation. Based on Figure 4.5.8 charge carrier recombination is the cause for lower *FF* measured after light exposure. As Figure 4.5.9 shows until irradiation time of 150 min the solar cell processed with 3% DIM had relatively lower rate of reduction in *FF* compared to the solar cell processes without DIM. However, after irradiation time of 150 min the solar cell processed with 3% DIM showed continuous increase in rate of reduction of *FF* compare to device without DIM. Again, similar to the case of J_{sc}, in the long run the additive DIM has negative effect on the *FF* of PCDTBT:PC$_{71}$BM solar cell exposed to light at ambient condition.

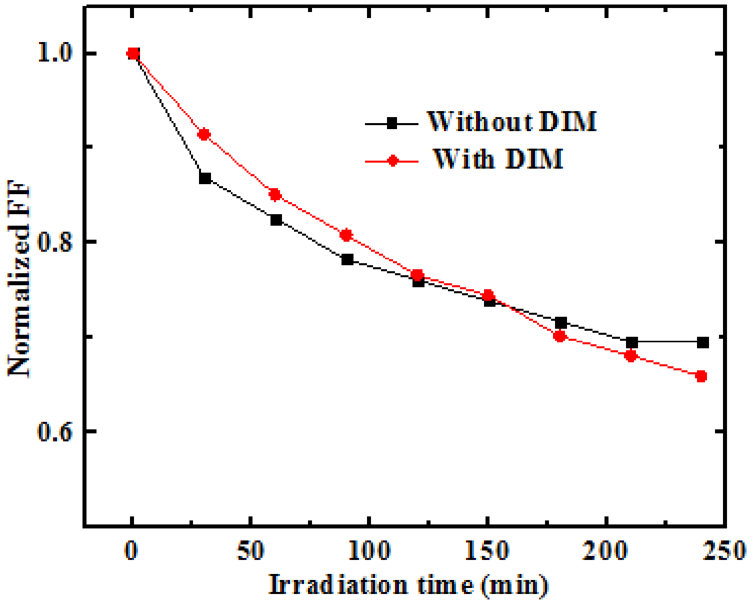

Figure 4.5.9: Normalized *FF* of the PCDTBT:PC$_{71}$BM solar cell processed without and with 3% DIM as a function of irradiation (100 mW/cm^2) time at ambient air.

The rate in reduction of V_{oc} of the PCDTBT:PC$_{71}$BM solar cell processed without and with 3% DIM as a function of irradiation (100 mW/cm^2) time at ambient air is given in Figure 4.5.10. The results indicate that the devices processed with DIM has lower rate of reduction compared to reference device in the study time. However, close examination of the result in Figure 4.5.10 (especially the last three values) indicates that after longer exposure time the device processed with DIM may not have stable V_{oc} and will give reduced value.

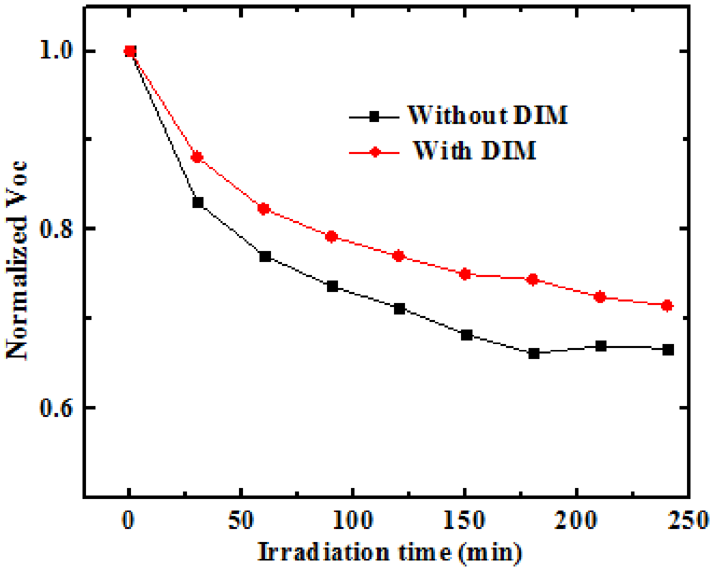

Figure 4.5.10: Normalized V_{oc} of the PCDTBT:PC$_{71}$BM solar cell processed without and with 3% DIM as a function of irradiation (100 mW/cm^2) time at ambient air.

Figure 4.5.11 shows the variation of normalized series resistance for PCDTBT:PC$_{71}$BM solar cell processed without and with 3% DIM as a function of irradiation (100 mW/cm^2) time at ambient air. The obtained values reveal that with irradiation time the series resistance of the device with DIM is continuously increasing. The increased R_s is consistent with the reduction of J_{sc} after ageing the device with light irradiation. The increased R_s is also the cause for the lower *FF* of the device processed with DIM.

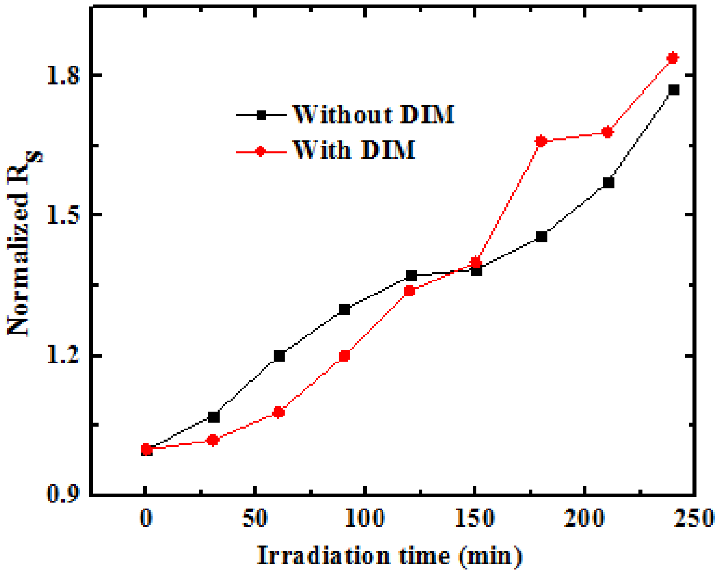

Figure 4.5.11: Normalized R_s of the PCDTBT:PC$_{71}$BM solar cell processed without and with 3% DIM as a function of irradiation time at ambient air.

4.5.6. Impedance analysis

In PSC, electrical property of the BHJ blend film is dictated by the morphology characteristics. Therefore, making connection between film morphology and electrical properties is very indispensable. Impedance spectroscopy (IS) allows the possibility of making a reasonable cause-effect relation between the morphology of the BHJ and the performance of PCDTBT:PC$_{71}$BM solar cells at different time of irradiation.

As literature shows, IS has been widely used in determining the electric characteristics through simple equivalent circuit models in PSCs [270]. The interfaces of the PCDTBT:PC$_{71}$BM solar cells can be considered as simple elements such as resistances and capacitances in circuit models (Figure 2.14). With the representation of the interfaces and BHJ film as resistances and capacitances, the electrical properties of the PCDTBT:PC$_{71}$BM

BHJ layer can be connected to current density-voltage (*J*-*V*) characteristics of the devices. In PCDTBT:$PC_{71}BM$ solar cells, the interface between the PCDTBT and $PC_{71}BM$ in the BHJ can directly relate to the morphology of the BHJ and the morphology of the BHJ directly affects performance of the device. To analyze the relationship between the morphology and the device performance of solar cell based on PCDTBT:$PC_{71}BM$ and with and without 3% DIM under different aging time, we used IS method.

Let us assume that in PCDTBT:$PC_{71}BM$ solar cell R_{12} corresponds to the resistance of PCDTBT:$PC_{71}BM$ active layer and the interface between PEDOT:PSS/PCDTBT:$PC_{71}BM$ and PCDTBT:$PC_{71}BM$/Al. R_{∞} corresponds to the resistance of the electrodes and wires connected for measurement. Since both PSCs have the same device structure, only the BHJ PCDTBT:$PC_{71}BM$ blend is processed under different conditions. Thus the R_{∞} inside all the cells can be assumed to be the same. However, R_{12} can give us information about the resistance which is affected by solvent additives, DIM.

Figure 4.5.12 shows the IS results of PCDTBT:$PC_{71}BM$ solar cells processed with and without 3% DIM. In Figure 4.5.12 the radius of the Cole-Cole plot is higher for the device processed without DIM and this implies that the resistance of the whole device is higher compared to the device processed with 3% DIM. The pristine PCDTBT:$PC_{71}BM$ solar cells processed without 3% DIM shows a R_{12} of 3725 Ω. On the other hand, PCDTBT:$PC_{71}BM$ solar cells processed with 3% DIM has much reduced R_{12} of 682 Ω. The much lower value of R_{12} of PCDTBT:$PC_{71}BM$ solar cells processed with 3% DIM implies that the thin film morphology of the PCDTBT:$PC_{71}BM$ blend was much improved through higher interfacial area between PCDTBT and $PC_{71}BM$ due to addition of DIM.

Smaller value of R_{12} for the device treated with DIM indicates a slower charge recombination and a smaller dark current [271, 272]. The smallest R_{12} value in DIM treated devices implies that the DIM allows more effective suppression of the recombination of charge carriers in the cells and lower charge transport resistance. The result obtained from IS is consistent with the recombination results previously obtained.

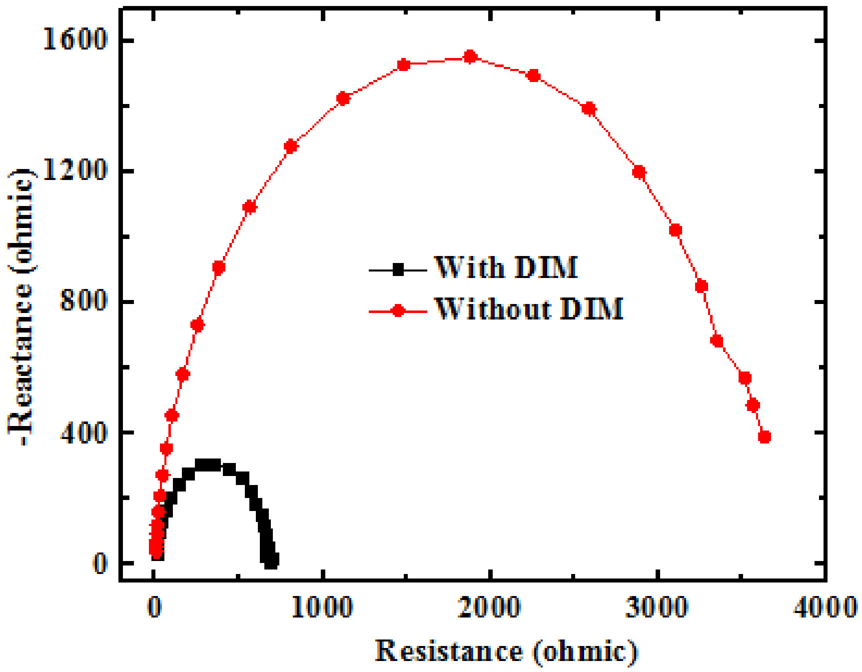

Figure 4.5.12: Cole-Cole plots of the PCDTBT:$PC_{71}BM$ solar cells processed with and without 3% DIM.

From literatures, we know that mixing additive with Polymer:$PC_{71}BM$ blend can lead to more favorable morphology of the Polymer:$PC_{71}BM$ BHJ due to decreasing the size of $PC_{71}BM$ and increasing the interfaces area between the polymer chains and $PC_{71}BM$ molecules [252, 273]. The result from Cole-Cole plot in Figure 4.5.12 shows that the resistance decreased after mixing 3% DIM with PCDTBT:$PC_{71}BM$ blend. Without DIM, the $PC_{71}BM$ aggregates are large and hinder $PC_{71}BM$ intercalation into PCDTBT network during film formation, so large segregated domains with lower interface area form (Figure 4.5.13) and increased the resistance. On the contrary, as shown in Figure 4.5.13 when DIM is added the $PC_{71}BM$ aggregates dissolves and higher interface area between PCDTBT chain and $PC_{71}BM$ molecules will be formed and as a result the resistance decreases.

Based on the general effect of additives and the result of resistance measurement, the sound logical inference is that on addition of DIM the interface area between PCDTBT chains and $PC_{71}BM$ molecules should be increased so that the resistance decreases.

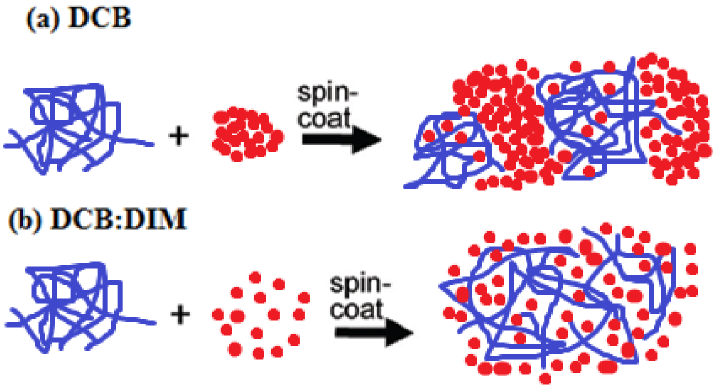

Figure 4.5.13: Schematic of PCDTBT and $PC_{71}BM$ aggregation in (a) DCB and (b) DCB:DIM and the resulting film morphology.

Figure 4.5.14 is the Cole-Cole plots of the PCDTBT:$PC_{71}BM$ solar cells processed with and without 3% DIM of pristine and 5 hr irradiated device. In Figure 4.5.14 for both devices the radius of the Cole-Cole plot increased after irradiating the device for 5 hr at ambient air, which implies that the resistance of the whole device has increased. The cause for increase of R_{12} after light irradiation is the decrease of interface area between the PCDTBT and $PC_{71}BM$. As the interface area decreases in PCDTBT:$PC_{71}BM$ due to $PC_{71}BM$ aggregate formation, the separation of exciton and penetration of carriers in the BHJ layer reduced.

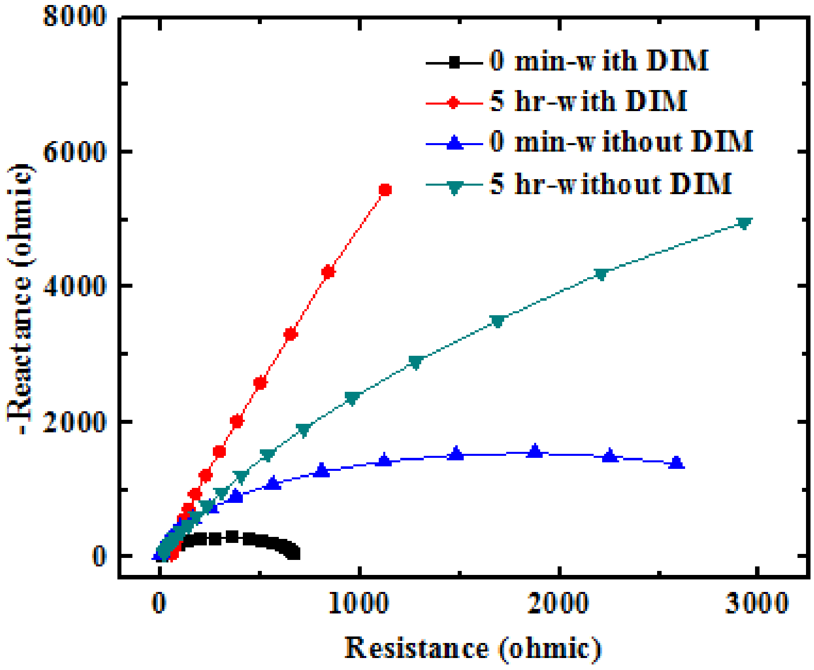

Figure 4.5.14: Cole-Cole plots of the PCDTBT:$PC_{71}BM$ solar cells processed with and without 3% DIM of pristine and 5 hr irradiated device.

4.5.7. Conclusions

In this work, the effect of DIM on the PCE and stability of PSCs made of PCDTBT:$PC_{71}BM$ was investigated. DIM is an effective additive in BHJ PCDTBT:$PC_{71}BM$ solar cell since it fulfills the requirement of a selective $PC_{71}BM$ dissolution. PCE of the device based on PCDTBT:$PC_{71}BM$ processed with DIM is higher than the reference device without DIM. The device without DIM has lower short circuit current density. The reason is that without DIM the $PC_{71}BM$ aggregates are large which hinders $PC_{71}BM$ intercalation into the PCDTBT network during film formation and this creates large, segregated domains of PCDTBT and $PC_{71}BM$. As a result of reduced interface area there will be lower exciton dissociation at the interface. However, on DIM addition the $PC_{71}BM$ aggregates dissolves and this facilitates integration of the $PC_{71}BM$ molecules into the PCDTBT system resulting in a greater PCDTBT:$PC_{71}BM$ interface area and smaller domains. Because of higher interface area there will be higher rate of exciton dissociation and this result in higher short circuit current density.

In terms of the device stability, PSCs processed with DIM showed poor stability at longer light exposure time. For the device without DIM especially as the light exposure time was increased, the device stability was better. The obtained result tell us that using the solvent additive DIM in the PCDTBT:$PC_{71}BM$ solar cells not only affects PCE of the device, but also affects its working lifetime. Hence, while using DIM to enhance PCE of PCDTBT:$PC_{71}BM$ solar cells it is good to consider the stability of the device.

For the PCDTBT:$PC_{71}BM$ device processed with DIM, the results obtained from *J-V* measurement indicates that it has lower recombination rate. The result from IS measurement show that for pristine PCDTBT:$PC_{71}BM$ devices with 3% DIM, the active layer resistance is lower compared to device without DIM. However, after irradiating the device for 5 hr the resistance of the device processed with DIM is higher and it is consistent with decreased PCE of aged device.

4.6. Polymer Solar Cells Fabricated Using Nanopatterned PEDOT:PSS

4.6.1. Background

Compared to the high efficiencies of inorganic solar cells, the best polymer based solar cells still show a lower efficiency. Two critical factors limiting the performance of PSCs are the short exciton diffusion length (~10 nm) and low mobility of charge carriers, especially the hole mobility ($\mu \sim 10^{-6} - 10^{-3}$ cm^2/Vs) within the photoactive layer [247, 274].

The bulk heterojunction (BHJ) structure has greatly improved the efficiency of polymer solar cells due to phase separated active-layer blend structure that increases the heterojunction area available for exciton dissociation [275, 276]. Nevertheless, the active layer morphology within this structure still remains disordered and far from ideal. Due to discrete and randomly distributed phases in BHJ structure there is significant charge recombination. The existence of large amount of disorder in the polymer chains resulting in low carrier mobility [277]. Recombination and inhibition of transport of charges to the electrodes are the major drawbacks of BHJ approach. Therefore, to realize improvements in PSC performance, a new technique which results in more favorable active layer morphology and an increase in exciton dissociation rates as well as charge carrier transport is required [278].

The above-mentioned drawbacks of BHJ approach can be solved if a vertically bicontinuous and interdigitized heterojunction nanomorphology is achieved. Watkins et al. [277] by simulation has shown that a bicontinuous and interdigitized heterojunction nanomorphology has internal quantum efficiency (IQE) 1.5 times higher than that for BHJ morphology, indicating a possible improvement in PCE. The ordered morphology allows for highly efficient lateral exciton diffusion and vertical transport with reduced recombination rates.

In this study we have investigated the effect of nanopatterned PEDOT:PSS on the *J-V* characteristics of P3HT:ICBA BHJ solar cells. By studying a series of solar cells with PEDOT:PSS on ITO-coated glass substrate either as spin-coated or processed by nanoimprint lithography (NIL), we observed that solar cells' characteristics are strongly affected by PEDOT:PSS patterning conditions.

4.6.2. Filling of nanopatterned PEDOT:PSS with active layer blend

Once nanopatterned PEDOT:PSS film is produced, the nanopatterns should be filled with blend material. To obtain improved light conversion efficiency in nanopatterned solar cells, the complete infiltration of blend materials into the nanostructured PEDOT:PSS film is critical in order to form an intimate and large interfacial junction area for efficient hole collection. PEDOT:PSS line grating structures with moderate aspect ratio (AR) (1 - 2) were filled using a concentration of 20 mg/mL of blend and spinning speed (500 - 1000 rpm). As shown in Figure 4.6.1 completely filled homogeneous film was obtained.

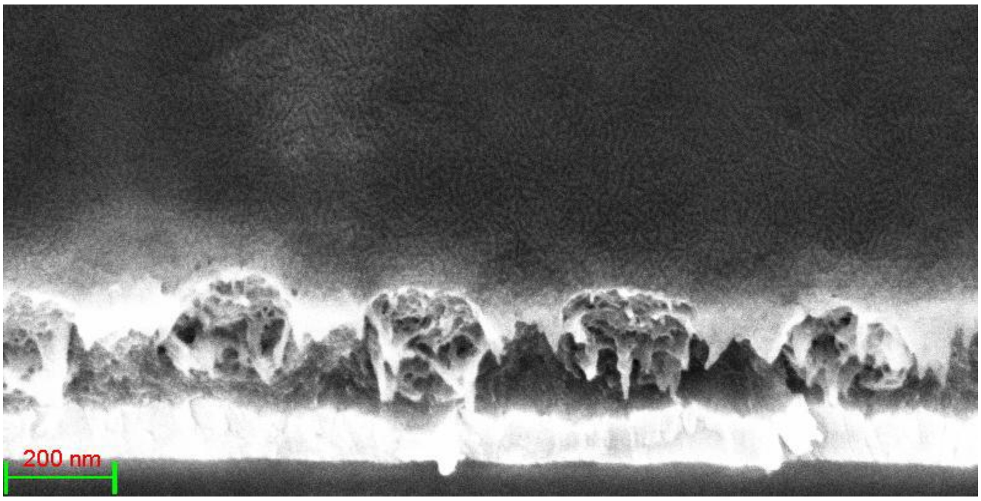

Figure 4.6.1: SEM micrograph of a 500 nm period PEDOT:PSS line grating, filled by spin coating at 700 rpm with 20 mg/mL solution of P3HT:ICBA (1:1).

4.6.3. Polymer solar cells on nanopatterned PEDOT:PSS electrode

To explore the effect of nanopattering of PEDOT:PSS on photovoltaic performance of P3HT based solar cell, solar cells fabricated using 300 nm period PEDOT:PSS line gratings (120/180 nm lines/gaps), aspect ratio ~2, imprinted at 95% RH, pressure-8 Mpa, temperatures of 80, 100, 130, and 150°C are characterized along with a flat reference cell.

Figure 4.6.2 shows the *J-V* characteristics of reference and nanopatterned solar cells. As shown in Figure 4.6.2, *J-V* curve of nanopatterned PEDOT:PSS based solar cell depend on the processing temperature. Nanopatterning of hole transporting layer (PEDOT:PSS) caused a clear change in the *J-V* characteristics of nanopatterned solar cells compared to flat reference.

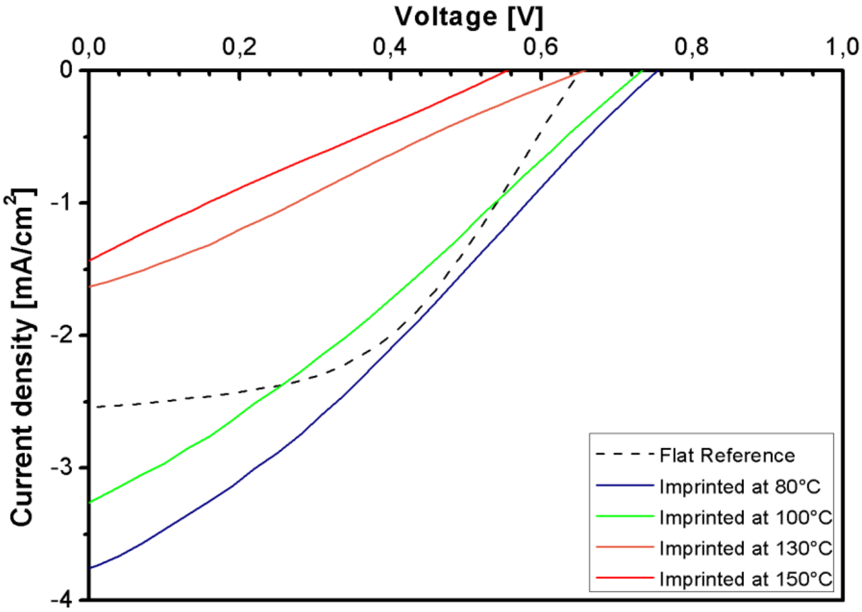

Figure 4.6.2: *J-V* characteristics of P3HT:ICBA bulk heterojunction solar cells build on the flat reference and WVA-NIL patterned PEDOT:PSS electrode patterned at different temperatures.

Figure 4.6.3 shows the main photovoltaic parameters, i.e. efficiency (η), short-circuit current density (J_{sc}), open-circuit voltage (V_{oc}) and fill factor (*FF*) under AM 1.5 simulated solar irradiation at 100 mW/cm^2 intensity. Photovoltaic parameters of the solar cells made on PEDOT:PSS patterned by WVA-NIL differ markedly from the reference cell made on the as-deposited 160 nm thick PEDOT:PSS film. Solar cell based on PEDOT:PSS patterned at 80^{o}C and the reference cell approximately shows the same efficiency of ~0.8%. However, the patterned one exhibit larger J_{sc} and V_{oc} than the flat reference cell (3.5 mA/cm^2 and 750 mV vs. 2.5 mA/cm^2 and 650 mV, respectively) and lower *FF* (30% instead of 48%).

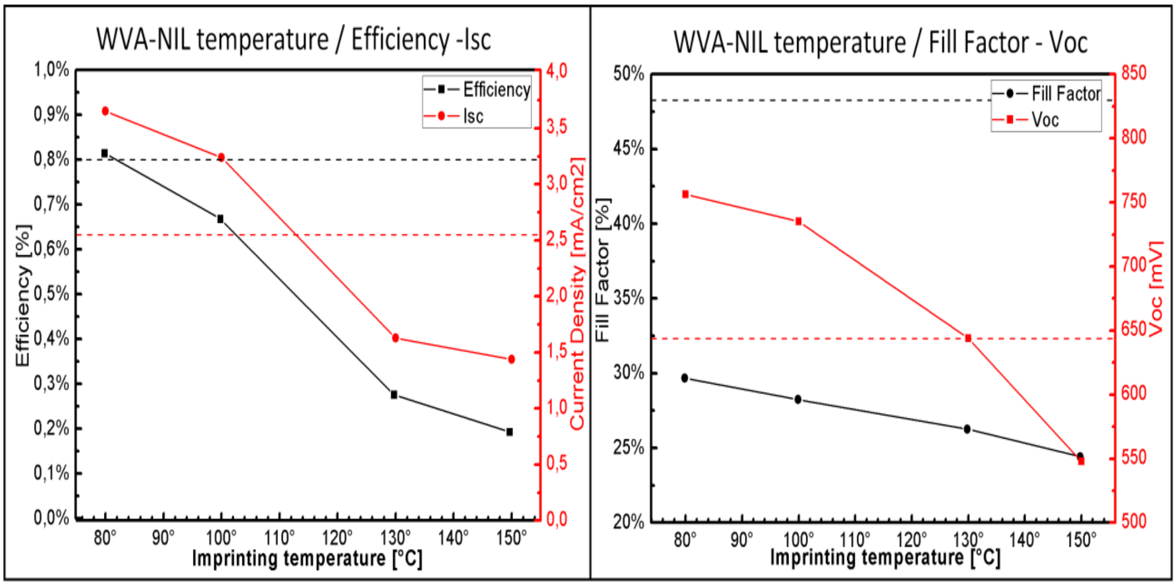

Figure 4.6.3: Effect of nanopatterning temperature on P3HT:ICBA solar cell η, J_{sc}, FF and V_{oc}. Dashed lines represent the value of the flat reference cell. The color of the lines indicates the corresponding scale.

Comparing solar cells based on PEDOT:PSS imprinted at 80°C and flat reference, increased J_{sc} for nanopatterned device is due to positive effect of the nanopatterned PEDOT:PSS in collecting holes. In case of nanopatterned PEDOT:PSS electrode, holes created far from flat PEDOT:PSS layer will have more chance for collection due to the nanopatterns penetrated into the active layer. Generally, V_{oc} depends on donor-acceptor energy gap and charge carrier recombination rate. For patterned device, the increased V_{oc} is due to lower charge carrier-recombination as a result of increased hole collection at nanopatterned PEDOT:PSS electrode. Increasing nanopatterning temperature to 150^{o}C leads to a progressive reduction of J_{sc}, V_{oc}, FF and efficiency of the solar cell.

Table 4.6.1: Comparison of the photovoltaic performance of flat and nanopatterned solar cells

PEDOT:PSS	η (%)	J_{sc} (mA/cm^2)	V_{oc} (mV)	FF (%)
Flat (reference)	0.80	2.5	649	48
Patterned at 80^{o}C	0.82	3.5	750	30
Patterned at 150^{o}C	0.19	1.44	548	24

The mechanism of lower holes and electrons recombination in nanopatterned PEDOT:PSS based solar cell is explained as follows. According to Yang et al. [279] nanopatterned PEDOT:PSS might change the directions of the electric field in the active layer. The change of direction of the electric field from *E* in a device using non-imprinted PEDOT:PSS film to *E'* in a device using PEDOT:PSS nanogratings makes the holes (h^+) dissociated close to the cathode able to be collected by shortening the hole collection path from dashed line to solid line. These holes are supposed to recombine with electrons in non-imprinted devices due to the relatively short hole drift length.

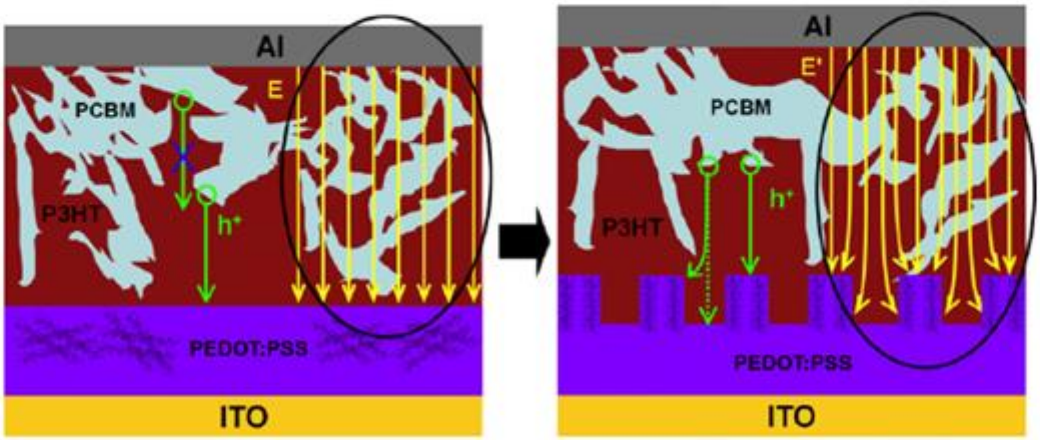

Figure 4.6.4: Comprehensive schematic overview of the proposed mechanisms [279].

Frohne et al. [280] has shown that decreasing work function of PEDOT:PSS results in *J-V* curves shifts closer to the origin of axes showing a progressive reduction in efficiency, J_{sc} and V_{oc}. As shown in Figure 4.6.2, when PEDOT:PSS is patterned at different temperature J_{sc} and V_{oc} shifted and closer to the origin of axes showing a reduction in their value and efficiency of the device. Therefore, by taking the experimental finding of Frohne et al. [280] as a premises, we expect decrease in work function of nanopatterned PEDOT:PSS at different temperatures. Thus, to verify our hypothesis it is imperative to measure the work function of PEDOT:PSS film patterned at different temperatures. The result of work function measurement of nanopatterned PEDOT:PSS at different conditions is given in Table 4.6.2 [281]. Lowering of the workfunction of nanopatterned PEDOT:PSS from 5.05 eV to 3.53 eV due to nanopatterning at 150°C results in a reduction of solar cell efficiency from 0.8% down to 0.19%. The decreased work function of nanopatterned PEDOT:PSS at 150°C results in the formation of barrier for hole injection from the polymer to the PEDOT:PSS.

Table 4.6.2: Workfunction of nanopatterned PEDOT:PSS at different temperature [281].

Nanopatterning Condition	**Work function (eV)**
Reference (flat)	5.05
Nanopatterned at 90% RH and 80^{o}C	4.97
Nanopatterned at 90% RH and 150^{o}C	3.53

Lee et al. [282] has clearly shown that there is correlation between work function and surface concentration of the PSS dopant in PEDOT:PSS film, with work function increasing for increasing PSS-to-PEDOT ratio at the surface. This effect was confirmed by Radivo et al. [281] using XPS measurement, in the opposite direction, i.e. a decreasing work function for decreasing PSS-to-PEDOT ratio. Currently most accepted morphological model of the PEDOT:PSS system can be used to explain the lower work function of nanopatterned PEDOT:PSS. The model give a picture of PEDOT:PSS morphology as consisting of colloids dispersed in water segregated into PEDOT-rich cores surrounded by PSS-rich shells, due to hydrophobic and hydrophilic character of PEDOT and PSS respectively. The core-shell structure is preserved to some extent also in the film. During spin coating the colloids fatten into a lamellar structure of PEDOT-rich layers vertically alternated with PSS-rich ones [283]. Spin coated PEDOT:PSS film forms a surface layer that is highly enriched in PSS, with respect to bulk PSS:PEDOT ratio [282, 284]. The surface composition of the PEDOT:PSS film highly depends on the film preparation processes such as thermal annealing process, solvent treatment and coating method [285].

In our particular case based on the above model and XPS measurement by Radivo et al. [281], therefore, the viable conclusion is that the lower work function of nanopatterned PEDOT:PSS film is due to lower ratio of PSS on the surface of nanopatterned PEDOT:PSS film caused by nanopatterning. During nanopatterning, PSS-rich top surface is replaced by a phase more rich in PEDOT would explain the reduction in the work function of nanopatterned PEDOT:PSS. To recover the appropriate ratio of PEDOT and PSS on the surface of the film, it is smart way to remove some of the PEDOT on the surface of nanopatterned PEDOT:PSS using appropriate means. To take away part of the PEDOT, oxygen plasma treatment of the nanopatterned PEDOT:PSS film is the right choice. By oxygen plasma treatment we can remove the PEDOT rich top surface and expose the PSS to the surface. Table 4.6.3 shows the work function of nanopatterned PEDOT:PSS film before and after oxygen plasma treatment. As the results show compared to flat (reference/unpatterned) PEDOT:PSS the work function of nanopatterned devices has decreased after nanopatterning. However, as we have speculated oxygen plasma treatments of the nanopatterned device increased the work function of nanopatterned PEDOT:PSS. The obtained experimental results show that oxygen plasma treatment is the easy and efficient means for increasing the work function of nanopatterned PEDOT:PSS.

Table 4.6.3: Work function of nanopatterned PEDOT:PSS before and after oxygen plasma treatment [281].

PEDOT:PSS patterning temp. (°C)	**Workfunction (eV)**	
	Before O_2 plasma	**after O_2 plasma**
Flat (N/A)	5.05	------
80	4.97	5.21 at 5 s
150	3.54	3.97 at 5 s
150	3.54	4.62 at 20 s

In order to understand the effect of modified work function of nanopatterned PEDOT:PSS as a result of oxygen plasma treatment on photovoltaic performance, real devices are fabricated based on nanopatterned and oxygen plasma treated PEDOT:PSS. O_2 plasma treatments were carried out for 0, 5, 30, 60 and 120 s on the nanopatterned PEDOT:PSS. Figure 4.6.5 shows the current-voltage characteristics and Figure 4.6.6 and Figure 4.6.7 shows extracted values for η, J_{sc}, V_{oc} and *FF* of the device fabricated on PEDOT:PSS nanopatterned by NIL at 80°C and 95% RH. The nanopatterns consisted of gratings of lines (250/250 nm lines/spaces) and were subsequently subjected to oxygen plasma for 0, 5, 30, 60 and 120 s.

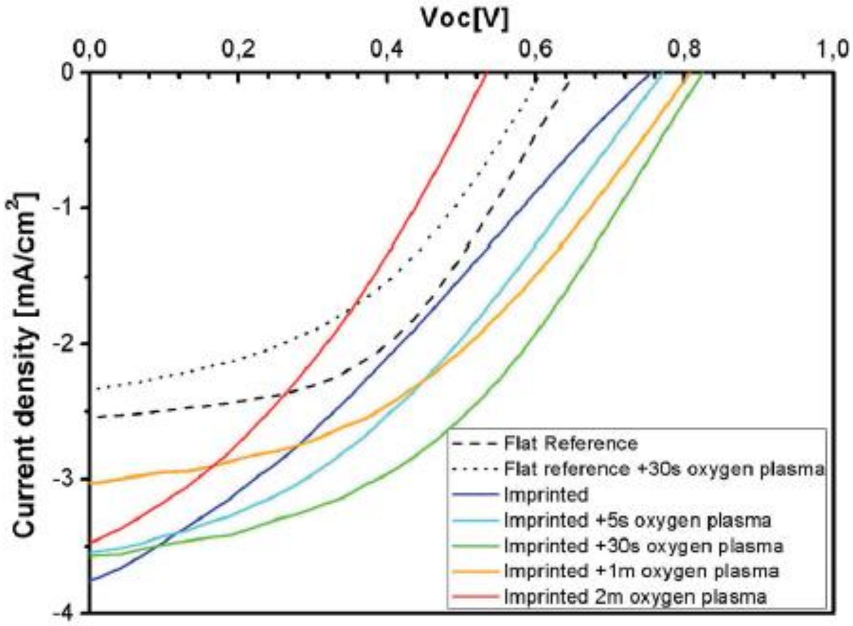

Figure 4.6.5: *J-V* characteristics of P3HT:ICBA BHJ solar cells build on flat reference and nanopatterned PEDOT:PSS at 80°C as a function of an additional oxygen plasma treatment time.

Figure 4.6.6 shows the summary of efficiency and short-circuit current density of P3HT:ICBA solar cells fabricated on nanopatterned PEDOT:PSS at 80°C as a function of an additional oxygen plasma treatment time. After 30, 60 and 120 s oxygen plasma treatment time, efficienciency of 1.3%, 1.1% (due to drop in J_{sc}) and 0.7% (due to drop in J_{sc}, V_{oc}, FF) respectively obtained.

The oxygen plasma treatment increased the work function from 4.97 to 5.21 eV and result in reducing the barrier for the hole injection and consequently increased the efficiency to 1.3%, i.e. 60% relative increase compared to the reference cell. The relative improvement in efficiency for devices using nanopatterned PEDOT:PSS over those using flat PEDOT:PSS film proves that nanopatterning of hole transporting layer (HTL) is a promising method to improve the performance of polymer solar cells. With additional study of factors governing nanopattering process of PEDOT:PSS, further improvement in efficiency can be envisaged.

By increasing the duration of the oxygen plasma to 1 min, the cells efficiency has decreased to 1.1%, mainly due a drop in the short circuit current density (whereas *FF* and V_{oc} remain essentially stable). Increasing further the oxygen plasma treatment to 2 min results in a drop to 0.7% efficiency by a combined drop of V_{oc} (from 800 mV to 525 mV) and *FF* (from 42.5% to 35%). The observed trends as a function of nanopatterning temperature and duration of oxygen plasma treatment show that the performances of cells tend to worsen.

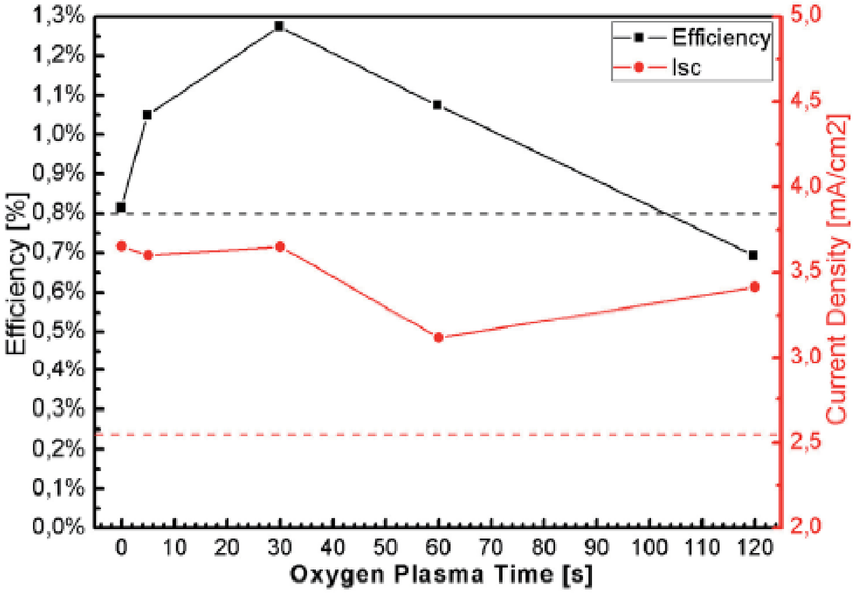

Figure 4.6.6: η and J_{sc} of P3HT:ICBA bulk heterojunction solar cells build on the flat reference and WVA-NIL patterned PEDOT:PSS electrode at 80ºC and 95% RH as a function of an additional oxygen plasma treatment time. Dashed lines represent the value of the flat reference cell.

Figure 4.6.7 shows fill factor and open-circuit voltage of P3HT:ICBA BHJ solar cells fabricated based on nanopatterned PEDOT:PSS at 80ºC as a function of an additional oxygen plasma treatment time.

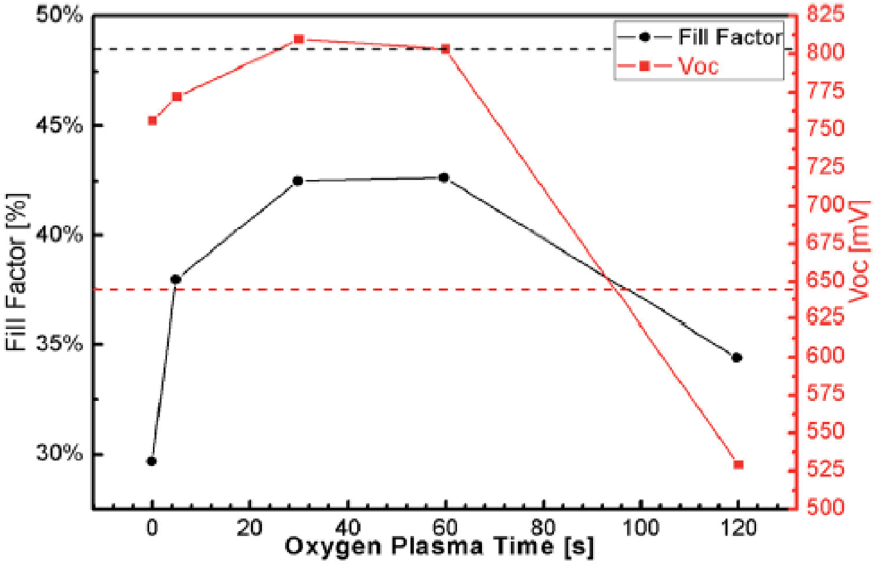

Figure 4.6.7: *FF* and V_{oc} of P3HT:ICBA bulk heterojunction solar cells build on the flat reference and WVA-NIL patterned PEDOT:PSS electrode at 80°C and 95% RH as a function of an additional oxygen plasma treatment time. Dashed lines represent the value of the flat reference cell.

Using ultraviolet photoelectron spectroscopy (UPS) Yun et al. [285] has studied the electronic properties of PEDOT:PSS at different annealing temperatures and times. From his study he has observed and reported an increase of work function (from 5.0 to 5.2 eV) upon annealing for 1 hr at 130°C in ultra high vacuum (interpreted as the effect of desorption of contaminants). On the contrary, for annealing temperature higher than 170°C the work function of PEDOT:PSS shifted gradually as a function of time towards lower values. For annealing temperatures of 220°C and 290°C for 3 hr the workfunction reduced to 4.8 and 4.5 eV, respectively. The observed progressive lowering of work function of PEDOT:PSS as the annealing temperature increases, correlated with a progressive reduction of the PSS at the film surface.

Based on the analogy with Yun et al. [285] observation, that is, initial increase and then decrease of work function of PEDOT:PSS after heating at different higher temperature, it is not irrational to expect a decrease in work function of nanopatterned PEDOT:PSS after oxygen plasma treatment for 120 s.

4.6.4. Conclusions

The presented experimental results on the application of NIL for performance improvement of organic solar cells shows that, NIL is really promising technique for improving efficiency of polymer solar cells. Nanopatterning of the PEDOT:PSS electrode can be used as a way to improve the cell efficiency. In our case relative increase of the 60%, from 0.8% to 1.3% of efficiency is obtained. The increased interfacial area and higher hole collection contributed for the improved photovoltaic performance of nanopatterned device. The obtained promising results give valuable information for further study on the application of nanopatterned PEDOT:PSS for polymer solar cells.

However, for better improvement, the following parameters should be optimized: thickness of the PEDOT:PSS lines, period, aspect ratio, P3HT:ICBA blend ratio, oxygen plasma treatment time, etc. and this require experimentation and possibly physical simulations studies.

References

1. M. Z. Jacobson, M. A. Delucchi, *Energy Policy* 39 (**2011**) 1154.
2. L. R. F. Henneman, P. Rafaj, H. J. Annegarn, C. Klausbruckner, *Energy Policy* 89 (**2016**) 160.
3. J. Ellis, H. Winkler, J. Corfee-Morlot, F. Gagnon-Lebrun, *Energy Policy* 35 (**2007**) 15.
4. E. Kisel, A. Hamburg, M. Härm, A. Leppiman, M. Ots, *Energy Policy* 95 (**2016**) 1.
5. V. Klevas, D. Streimikiene, R. Grikstaite, *Energy Policy* 35 (**2007**) 76.
6. F. Llano-Paz, A. Calvo-Silvosa, S. I. Antelo, I. Soares, *Renew. Sustain. Energy Rev*. 48 (**2015**) 49
7. S. Dubey, N. Y. Jadhav, B. Zakirova, *Energy Procedia* 33 (**2013**) 322.
8. Y. Mastai, S. Polarz, M. Antonietti, *Adv. Funct. Mater*. 12 (**2002**) 197.
9. A. A. Bakulin,Y. Xia, H. J. Bakker, O. Inganäs, Feng Gao, *J. Phys. Chem. C* 120 (**2016**) 4219.
10. I. F. Domínguez, P. D. Topham, P.-O. Bussière, D. Bégué, A. Rivaton, *J. Phys. Chem. C* 119 (**2015**) 2166.
11. S. A. Moiz, M. M. Ahmed, K. S. Karimov, F. Rehman, J.-H. Lee, *Synth. Met*. 159 (**2009**) 1336.
12. E. Bundgaard, F.C. Krebs, *Sol. Energy Mater. Sol. Cells* 91 (**2007**) 954.
13. K. S. Karimov, M. M. Ahmed, S. A. Moiz, M. I. Fedorov, *Sol. Energy Mater. Sol. Cells* 87 (**2005**) 61.
14. C. J. Brabec, N. S. Sariciftci, J.C. Hummelen, *Adv. Funct. Mater*. 11 (**2001**) 15.
15. W. Kim, J. K. Kim, E. Kim, T. K. Ahn, D. H. Wang, J. H. Park, *J. Phys. Chem. C* 119 (**2015**) 5954.
16. Y. Kawanabe, A. J. Moulé, R. Faller, *J. Chem. Eng. Data* 59 (**2014**) 2982.
17. S. Few, J. M. Frost, J. Nelson, *Phys. Chem. Chem. Phys*. 17 (**2015**) 2311.
18. M. Peach. *Optics.org. News desk*, 23 Jan. **2013**. Web Accessed 9 Aug. **2013**.
19. F. Etzold, I. A. Howard, N. Forler, A. Melnyk, D. Andrienko, M. R. Hansen, F. Laquai, *Energy Environ. Sci*. 8 (**2015**) 1511.
20. Z. He, C. Zhong, S. Su, M. Xu, H. Wu, Y. Cao, *Nat. Photonics* 6 (**2012**) 591.
21. J. You, C. C. Chen, Z. Hong, K. Yoshimura, K. Ohya, R. Xu, S. Ye, J. Gao, G. Li, Y. Yang, *Adv. Mater*. 25 (**2013**) 3973.
22. J. U. Lee, J. W. Jung, J. W. Job, W. H. Jo, *J. Mater. Chem*. 22 (**2012**) 24265.

23. M. Jørgensen, K. Norrman, S. A. Gevorgyan, T. Tromholt, B. Andreasen, F. C. Krebs, *Adv. Mater*. 24 (**2012**) 580.
24. U. Dettinger, H.-J. Egelhaaf, C. J. Brabec, F. Latteyer, H. Peisert, T. Chasse, *Chem. Mater*. 27 (**2015**) 2299.
25. M. Manceau, A. Rivaton, J.-L. Gardette, S. Guillerez, N. Lemaitre, *Polym. Degrad. Stab*. 94 (**2009**) 898.
26. M. O. Reese, A. J. Morfa, M. S. White, N. Kopidakis, S. E. Shaheen, G. Rumbles, D. S. Ginley, *Sol. Energy Mater. Sol. Cells* 92 (**2008**) 746.
27. S. A. Gevorgyan, M. Jørgensen, F. C. Krebs, *Sol. Energy Mater. Sol. Cells* 92 (**2008**) 736.
28. V. Turkovic, S. Engmann, D. A. M.Egbe, M. Himmerlich, S. Krischok, G. Gobsch, H. Hoppe, *Sol. Energy Mater. Sol. Cells* 120 (**2014**) 654.
29. W. R. Mateker, I. T. Sachs-Quintana, G. F. Burkhard, R. Cheacharoen, M. D. McGehee, *Chem. Mater*. 27 (**2015**) 404.
30. G. Dennler, M. C. Scharber, C. J. Brabec, *Adv. Mater*. 21 (**2009**) 1323.
31. J. You, L. Dou, K. Yoshimura, T. Kato, K. Ohya, T. Moriarty, K. Emery, C. C. Chen, J. Gao, G. Li, Y. Yang, *Nat. Commun*. 4 (**2013**) 1446.
32. T. Yohannes, *PhD dissertation*, Addis Ababa University (**1997**) Addis Ababa, Ethiopia.
33. I.-Y. Jeon, J.-B. Baek, *Materials* 3 (**2010**) 3654.
34. J. C. Lotters, W. Olthuis, P. H. Veltink, P. Bergveld, *J. Micromech. Microeng*. 7 (**1997**) 145.
35. A. J. Epstein, J.M. Ginder, F. Zuo, R.W. Bigelow, H.Woo, D.B. Tanner, A.F. Richter, W. Huang, G.A. MacDiarmid, *Synth. Met.* 18 *(***1987)** 303.
36. J. Pople, S. Walmsley, *Molecular Physics* 5 (**1962**) 15.
37. D. A. Weiss, B. A. Bolto, R. Mcneill, *Australian Journal of Chemistry* 16 (**1963**) 1090.
38. V. Walatka, M. M. Labes, J. H. Perlstein, *Phys. Rev. Lett.* 31 (**1973**) 1139.
39. W. D. Gill, W. Bludau, R. H. Geiss, P. M. Grant, R. L. Greene, J. J. Mayerle, G. B. Street, *Phys. Rev. Lett.* 38 (**1977**) 1305.
40. H. Shirakawa, E. J. Louis, A. G. MacDiarmid, C. K. Chiang, A. J. Heeger, *J. Chem. Soc. Chem. Commun*. (**1977**) 578.
41. C. K. Chiang, C. R. Fincher, Y. W. Park, A. J. Heeger, H. Shirakawa, E. J. Louis, A. G. MacDiarmid, *Phys. Rev. Lett.* 39 (**1977**) 1098.
42. A. K. Bakhshi, G. Bhalla, *J. Sci. Ind. Res*. 63 (**2004**) 715.

43. T. Yohannes, T. Solomon, O. Inganas, *Synt. Met.* 82 (**1996)** 215.

44. A. J. Heeger, A. G. MacDiarmid, H. Shirakawa, *Nobel lectures for the Nobel Prize in Chemistry* **2000**.

45. J. J. M. Halls, C. A. Walsh, N. C. Greenham, E. A. Marseglia, R. H. Friend, S. C. Moratti, A. B. Holmes, *Nature* 376 (**1995)** 498.

46. A. Kraft, A. C. Grimsdale, A. B. Holmes, *Angew. Chem. Int. Edit*. 37 (**1998)** 402.

47. A. R. Hepburn, J. M. Marshall, J. M. Maud, *Synt. Met.* 43 (**1991)** 2935.

48. J. C. Dubois, O. Sagnes, F. Henry, *Synt. Met.* 28 *(***1989)** C871.

49. B. Adhikari, S. Majumdar, *Prog. Polym. Sci*. 29 (**2004**) 699.

50. U. Lange, N. V. Roznyatovskaya, V. M. Mirsky, *Anal. Chim. Acta* 614 (**2008**) 1.

51. D. D. C. Bradley, *Chem. Brit.* 27 (**1991)** 719.

52. A. Burke, *J. Power Sources* 91 (**2000)** 37.

53. G. Sonmez, H. Meng, Q. Zhang, F. Wudl, *Adv. Funct. Mater.* 13 (**2003)** 726.

54. A. L. Roes, E. A. Alsema, K. Blok, M. K. Patel, *Prog. Photovolt. Res. Appl*. 17 (**2009**) 372.

55. C. W. Tang, *Appl. Phys. Lett*. 48 (**1986**) 183.

56. S. Yamamoto, H. Ohkita, H. Benten, S. Ito, S. Yamamoto, D. Kitazawa, J. Tsukamoto, *J. Phys. Chem. C* 117 (**2013**) 11514.

57. M. Gerhard, A. P. Arndt, I. A. Howard, A. Rahimi-Iman, U. Lemmer, M. Koch, *J. Phys. Chem. C* 119 (**2015**) 28309.

58. K. S. Liao, S. D. Yambem, A. Haldar, N. J. Alley, S. A. Curran, *Energies* 3 (**2010**) 1212.

59. S. H. Park, A. Roy, S. Beaupré, S. Cho, N. Coates, J. S. Moon, D. Moses, M. Leclerc, K. Lee, A. J. Heeger, *Nat. Photonics* 3 (**2009**) 297.

60. Y.-W. Su, C.-M. Liu, J.-M. Jiang, C.-S. Tsao, H.-C. Cha, U-S. Jeng, H.-L. Chen, K.-H. We, *J. Phys. Chem. C* 119 (**2015**) 3408.

61. T. Saga, *NPG Asia Mater*. 2 (**2010**) 96.

62. A. G. Martin, E. Keith, H. Yoshihiro, W. Wilhelm, *Prog. Photovoltaics Res. Appl.* 17 (**2009**) 320.

63. E. H. Sargent, *Nat. Photonics* 3 (**2009**) 325.

64. C. Liu, X. Hu, C. Zhong, M. Huang, K. Wang, Z. Zhang, X. Gong,Y. Cao, A. J. Heeger, *Nanoscale* 6 (**2014**) 14297.

65. R. A. Street, S. A. Hawks, P. P. Khlyabich, G. Li, B. J. Schwartz, B. C. Thompson, Y. Yang, *J. Phys. Chem. C* 118 (**2014**) 21873.

66. A. F. Zielnik, D. P. Dumbleton, *Solar Energy Competence Center Atlas Material Testing Technology LLC*, **2010**.
67. D. H. Wang, J. K. Kim, J. H. Seo, O. O. Park, J. H. Park, *Sol. Energy Mater. Sol. Cells* 101 (**2012**) 249.
68. M. P. Nikiforov, J. Strzalka, S. B. Darling, *Sol. Energy Mater. Sol. Cells* 110 (**2013**) 36.
69. M. Jørgensen, K. Norrman, F. C. Krebs, *Sol. Energy Mater. Sol. Cells* 92 (**2008**) 686.
70. M. Manceau, E. Bundgaard, J. E. Carle, O. Hagemann, M. Helgesen, R. Søndergaard, M. Jørgensen, F. C. Krebs, *J. Mater. Chem*. 21 (**2011**) 4132.
71. K. Norrman, M. V. Madsen, S. A. Gevorgyan, F. C. Krebs, *J. Am. Chem. Soc*. 132 (**2010**) 16883.
72. F. Gao, O. Inganas, *Phys. Chem. Chem. Phys*. 16 (**2014**) 20291.
73. R. Mauer, I. A. Howard, F. Laquai, *J. Phys. Chem. Lett.* 1 (**2010**) 3500.
74. F. Padinger, R. S. Rittberger, N. S. Sariciftci, *Adv. Funct. Mater*. 13 (**2003**) 85.
75. H. Bassler, A. Kohler, *Phys. Chem. Chem. Phys*. 17 (**2015**) 28451.
76. K. Li, P. P. Khlyabich, L. Li, B. Burkhart, B. C. Thompson, J. C. Campbell, *J. Phys. Chem. C* 117 (**2013**) 6940.
77. J.-L. Bredas, J. Cornil, A. J. Heeger, *Adv. Mater*. 8 (**1996**) 447.
78. S. Tscheuschner, H. Bässler, K. Huber, A. Köhler, *J. Phys. Chem. B* 119 (**2015**) 10359.
79. V. I. Arkhipov, H. Bassler, *phys. stat. sol. A* 201 (**2004**) 1152.
80. S. F. Alvarado, P. F. Seidler, D. G. Lidzey, D. D. C. Bradley, *Phys. Rev. Lett*. 81 (**1998**) 1082.
81. E. R. Bittner, V. Lankevich, S. Gelinas, A. Rao, D. A. Ginger, R. H. Friend, *Phys. Chem. Chem. Phys*. 16 (**2014**) 20321.
82. A. Manor, E. A. Katz, T. Tromholt, B. Hirsch, F. C. Krebs, *J. Appl. Phys*. 109 (**2011**) 074508.
83. S. Gunes, H. Neugebauer, N. S. Sariciftci, *Chem. Rev.*107 (**2007**) 1324.
84. H. Hoppe, N. S. Sariciftci, *J. Mater. Chem.* 16 (**2006)** 45.
85. K. Tvingstedt, K. Vandewal, A. Gadisa, F. Zhang, J. Manca, O. Inganas, *J. Am. Chem. Soc*. 131 (**2009**) 11819.
86. S. M. Sze, K. K. Ng, *Physics of Semiconductor Devices*, 3nd Ed. Wiley, India, **2007**.
87. J. C. Blakesley, D. Neher, *Phys. Rev. B* 84 (**2011**) 075210.
88. S. R. Cowan, W. L. Leong, N. Banerji, G. Dennler, A. J. Heeger, *Adv. Funct. Mater.* 21 (**2011**) 3083.

89. S. Lilliu, T. Agostinelli, E. Pires, M. Hampton, J. Nelson, J. E. Macdonald, *Macromol.* 44 (**2011**) 2725.

90. W. C. Tsoi, D. T. James, J. S. Kim, P. G. Nicholson, C. E. Murphy, D. D. C. Bradley, J. Nelson, J.-S. Kim, *J. Am. Chem. Soc.* 133 (**2011**) 9834.

91. T. Agostinelli, S. Lilliu, J. G. Labram, M. Campoy-Quiles, M. Hampton, E. Pires, J. Rawle, O. Bikondoa, D. D. C. Bradley, T. D. Anthopoulos, J. Nelson, J. E. Macdonald, *Adv. Funct. Mater.* 21 (**2011**) 1701.

92. N. Grossiord, J. M. Kroon, R. Andriessen, P. W. M. Blom, *Org. Electron.* 13 (**2012**) 432.

93. G. F. A. Dibb, F. C. Jamieson, A. Maurano, J. Nelson, J. R. Durrant, *J. Phys. Chem. Lett.* 4 (**2013**) 803.

94. C. Gueymard, D. Myers, K. Emery, *Solar Energy* 73 (**2002**) 443.

95. P. Kumar, S. C. Jain, V. Kumar, S. Chand, R. P. Tandon, *J. Appl. Phys*. 105 (**2009**) 104507.

96. S. Dal Zilio, *PhD dissertation*, Università degli Studi di Padova (**2009)**, Italy.

97. V. Coropceanu, J. Cornil, D. A. da S. Filho, Y. Olivier, R. Silbey, J.-L. Bredas, *Chem. Rev*. 107 (**2007**) 926.

98. F. Laquai, G. Wegner, H. Bassler, *Phil. Trans. R. Soc. A* 365 (**2007**) 1473.

99. M. S. A. Abdou, S. Holdcroft, *Macromol.* 26 (**1993**) 2954.

100. E. T. Hoke, I. T. Sachs-Quintana, M. T. Lloyd, I. Kauvar, W. R. Mateker, A. M. Nardes, C. H. Peters, N. Kopidakis, M. D. McGehee, *Adv. Energy Mater.* 2 (**2012**) 1351.

101. M. Manceau, A. Rivaton and J.-L. Gardette, *Macromol. Rapid Commun*. 29 (**2008**) 1823.

102. H. Hintz, H.-J. Egelhaaf, H. Peisert and T. Chasse, *Polym. Degrad. Stab*. 95 (**2010**) 818.

103. R. Pacios, A. J. Chatten, K. Kawano, J. R. Durrant, D. D. C. Bradley, J. Nelson, *Adv. Funct. Mater*. 16 (**2006**) 2117.

104. H. Hintz, H.-J. Egelhaaf, L. Lüer, J.A. Hauch, H. Peisert, T. Chassé, *Chem. Mater*. 23 (**2011**) 145.

105. A. Tournebize, P.-O. Bussière, P. Wong-Wah-Chung, S. Thérias, A. Rivaton, J.-L. Gardette, S. Beaupré, M. Leclerc, *Adv. Energy Mater*. 3 (**2013**) 478.

106. J. Milliken, T. M. Keller, A. P. Baronavski, S. W. McElvany, J. H. Callahan, H. H. Nelson, *Chem. Mater*. 3 (**1991**) 386.

107. I. M. K. Ismail, *Carbon* 30 (**1992**) 229.

108. Y. Matsuo, A. Ozu, N. Obata, N. Fukuda, H. Tanaka and E. Nakamura, *Chem. Commun.* 48 (**2012**) 3878.

109. A. Tapponnier, I. Biaggio, P. Günter, *Appl. Phys. Lett*. 86 (**2005**) 112114.

110. A. Hamed, Y. Y. Sun, Y. K. Tao, R. L. Meng, P. H. Hor, *Phys. Rev. B* 47 (**1993**) 10875.

111. P. C. Eklund, A. M. Rao, P. Zhou, Y. Wang, J. M. Holden, *Thin Solid Films* 257 (**1995**) 185.

112. J. W. Arbogast, A. P. Darmanyan, C. S. Foote, Y. Rubin, F. N. Diederich, M. M. Alvarez, S. J. Anz, R. L. Whetten, *J. Phys. Chem.* 95 (**1991**) 11.

113. R. Lessmann, Z. Hong, S. Scholz, B. Maennig, M.K. Riede, K. Leo, *Org. Electron*. 11 (**2010**) 539.

114. S. Chambon, A. Rivaton, J. L. Gardette and M. Firon, *Sol. Energy Mater. Sol. Cells* 91 (**2007**) 394.

115. R. Konenkamp, G. Priebe and B. Pietzak, *Phys. Rev. B* 60 (**1999**) 11804.

116. M. P. de Jong, L. J. van IJzendoorn, M. J. A. de Voigt, *Appl. Phys. Lett*. 77 (**2000**) 2255.

117. G.-F. Wang, X.-M. Tao, R.-X. Wang, *Nanotechnologies* 19 (**2008**) 145201.

118. S. I. Na, G. Wang, S. S. Kim, T. W. Kim, S. H. Oh, B. K. Yu, *J. Mater. Chem.* 19 (**2009)** 9045.

119. M. G. Kang, M. S. Kim, J. S. Kim, L. J. Guo, *Adv. Mater.* 20 (**2008)** 4408.

120. R. C. Tenent, T. M. Barnes, J. D. Bergeson, A. J. Ferguson, *Adv. Mater.* 21 (**2009)** 3210.

121. Z. Yin, S. Wu, X. Zhou, X. Huang, Q. Zhang, F. Boey, H. Zhang, *small* 6 (**2010**) 307.

122. A. M. Nardes, M. Kemerink, M. M. de Kok, E. Vinken, K. Maturova, R. A. J. Janssen, *Org. Electron*. 9 (**2008**) 727.

123. K. Kawano, R. Pacios, D. Poplavskyy, J. Nelson, D. D. C. Bradley, J. R. Durrant, *Sol. Energy Mater. Sol. Cells* 90 (**2006**) 3520.

124. A. Kumar, W. C. A. Wilisch, N. S. Lewis, *Crit. Rev. Solid State Mater. Sci*. 4 (**1993**) 327.

125. R. T. Tung, *Phys. Rev. B* 45 (**1992**) 13509.

126. J. H. Werner, H. H. Guttler, *J. Appl. Phys*. 69 (**1991**) 1522.

127. J. H. Werner, A. F. J. Levi, R. T. Tung, M. Anzlowar, M. Pinto, *Phys. Rev. Lett*. 60 (**1988**) 53.

128. R. F. Broom, H. P. Meier, W. Walter, *J. Appl. Phys*. 60 (**1986**) 1833.
129. W. Bantikassegn, P. Dannetum, O. Inganas, W. R. salaneck, *Thin Solid Films* 224 (**1993**) 232.
130. H. Tomozawa, F. Braun, S. Phillips, A. J. Heeger, H. Kroemer, *Synth. Met*. 22 (**1987**) 63.
131. O. Gullu, S. Aydogan, A. Turut, *Microelectron. Eng*. 85 (**2008**) 1647.
132. M. Okutan, F. Yakuphanoglu, *Microelectron. Eng*. 85 (**2008**) 646.
133. S. K. Cheung, N. W. Cheung, *Appl. Phys. Lett*. 49 (**1986**) 85.
134. M. A. Lampert, *Injection Currents in Solids*, New York, Academic Press, **1965**.
135. T. P. Nguyen, *Phys. Stat. Sol*. 205 (**2008**) 162.
136. P. Mark, M. Allen, *Ann. Rev. Mater. Sci*. 3 (**1973**) 111.
137. M. A. Lampert, *Phys. Rev.* 103 (**1956**) 1648.
138. G. T. Wright, *Solid State Electronics* 2 (**1961**) 165.
139. J. Lindmayer, J. Reynolds, C. Wrigley, *J. Appl. Phys*. 34 (**1963**) 809.
140. A. Rose, *Phys. Rev*. 97 (**1955**) 1538.
141. K. C. Kao and W. Hwang, *Electrical Transport in Solids*, Pergamon Press, Oxford, **1981**.
142. G. Amin, I. Hussain, S. Zaman, N. Bano, O. Nur, M. Willander, *phys. stat. sol. A* 207 (**2010**) 748.
143. K. C. Kao, *Dielectric Phenomena in Solids*, Academic Press, San Diego, **2004**.
144. E. G. Bylandeer, *J. Appl. Phys*. 49 (**1978**) 1188.
145. C. X. Zhao, A. Y. Mao, G. Xu, *Appl. Phys. Lett*. 105 (**2014**) 063302.
146. J. Simmons, *J. Phys. Chem. Solids* 32 (**1971**) 1987.
147. G. Garcia-Belmonte, A. Munar, E. M. Barea, J. Bisquert, I. Ugarte, R. Pacios, *Org. Electron.* 9 (**2008**) 847.
148. E.-P. Yao, C.-C. Chen, J. Gao, Y. Liu, Q. Chen, M. Cai, W.-C. Hsu, Z. Hong, G. Li, Y. Yang, *Sol. Energy Mater. Sol. Cells* 130 (**2014**) 20.
149. C. H. Kim, K. Kisiel, J. Jung, J. Ulanski, D. Tondelier, B. Geffroy, Y. Bonnassieux, G. Horowitz, *Synt. Met.* 162 (**2012)** 460.
150. G. Garcia-Belmonte, P. P. Boix, J. Bisquert, M. Sessolo, H. J. Bolink, *Sol. Energy. Mater. Sol. Cells* 94 (**2010**) 366.
151. G. Garcia-Belmonte, A. Guerrero, J. Bisquert, *J. Phys. Chem. Lett.* 4 (**2013**) 877.
152. I. Mora-Sero, G. Garcia-Belmonte, P. P. Boix, M. A. Vazquez, J. Bisquert, *Energy Environ. Sci*. 2 (**2009**) 678.

153. T. Ripolles-Sanchis, A. Guerrero, J. Bisquert, G. Garcia-Belmonte, *J. Phys. Chem. C* 116 (**2012**) 16925.
154. E. T. Hoke, K. Vandewal, J. A. Bartelt, W. R. Mateker, J. D. Douglas, R. Noriega, K. R. Graham, J. M. J. Fréchet, A. Salleo, M. D. McGehee, *Adv. Energy Mater*. 3 (**2012**) 220.
155. J. Kniepert, I. Lange, J. Heidbrink, J. Kurpiers, T. J. K. Brenner, L. J. A. Koster, D. Neher, *J. Phys. Chem. C* 119 (**2015**) 8310.
156. D. E. Motaung, G. F. Malgas, C. J. Arendse, S. E. Mavundla, *Mater. Chem. Phys*. 135 (**2012**) 401.
157. P. J. Brown, D. S. Thomas, A. Kohler, J. S. Wilson, J. S. Kim, C. M. Ramsdale, H. Sirringhaus, R. H. Friend, *Phys. Rev. B* 67 (**2003**) 064203.
158. T. Tromholt, M. V. Madsen, J. E. Carle, M. Helgesen, F. C. Krebs, *J. Mater. Chem*. 22 (**2012**) 7592.
159. M. O. Reese, A. M. Nardes, B. L. Rupert, R. E. Larsen, D. C. Olson, M. T. Lloyd, S. E. Shaheen, D. S. Ginley, G. Rumbles, N. Kopidakis, *Adv. Funct. Mater*. 20 (**2010**) 3476.
160. L. Luer, H.-J. Egelhaaf, D. Oelkrug, G. Cerullo, G. Lanzani, B.-H. Huisman, D. de Leeuw, *Org. Electron*. 5 (**2004**) 83.
161. B. Kraabel, J. C. Hummelen, D. Vacar, D. Moses, N. S. Sariciftci, A. J. Heeger, *J. Chem. Phys*. 104 (**1996**) 4267.
162. A. Distler, P. Kutka, T. Sauermann, H.-J. Egelhaaf, D. M. Guldi, D. D. Nuzzo, S. C. J. Meskers, R. A. J. Janssen, *Chem. Mater*. 24 (**2012**) 4397.
163. E. B. Zeynalov, N. S. Allen, N. I. Salmanova, *Polym. Degrad. Stab*. 94 (**2009**) 1183.
164. Y. Yamakoshi, N. Umezawa, A. Ryu, K. Arakane, N. Miyata, Y. Goda, T. Masumizu, T. Nagano, *J. Am. Chem. Soc*. 125 (**2003**) 12803.
165. S. Hotta, S.D.D.V. Rughooputh, A.J. Heeger, F. Wudl, *Macromol.* 20 (**1987**) 212.
166. A. Tamanai, S. Beck, A. Pucci, *Displays* 34 (**2013**) 399.
167. G. A. H. Wetzelaer, M. Kuik, M. Lenes, P. W. M. Blom, *Appl. Phys. Lett*. 99 (**2011**) 153506.
168. S. A. Hawks, G. Li, Y. Yang, R. A. Street, *J. Appl. Phys*. 116 (**2014**) 074503.
169. R. A. Street, J. E. Northrup, B. S. Krusor, *Phys. Rev. B* 85 (**2012**) 205211.
170. C. Vanberkel, M. J. Powell, A. R. Franklin, I. D. French, *J. Appl. Phys*. 73 (**1993**) 5264.

171. M. A. Wolf, M. Wolf, *IEEE Trans. Electron Devices* 31 (**1984**) 684.

172. R. A. Street, A. Krakaris, S. R. Cowan, *Adv. Funct. Mater*. 22 (**2012**) 4608.

173. M. O. Reese, S. A. Gevorgyan, M. Jørgensen, E. Bundgaard, S. R. Kurtz, D. S. Ginley, D. C. Olson, M. T. Lloyd, P. Morvillo, E. A. Katz, A. Elschner, O. Haillant, T. R.Currier, V. Shrotriya, M. Hermenau, M. Riede, K. R. Kirov, G. Trimmel, T. Rath, O. Inganas, F. Zhang, M. Andersson, K. Tvingstedt, M. Lira-Cantu, D. Laird, C. McGuiness, S. Gowrisanker, M. Pannone, M. Xiao, J. Hauch, R. Steim, D. M. De Longchamp, R. ROsch, H. Hoppe, N. Espinosa, A. Urbina, G. Yaman-Uzunoglu, J.-B. Bonekamp, A. J. J. M. van Breemen, C. Girotto, E. Voroshazi, F. C.Krebs, *Sol. Energy Mater. Sol. Cells* 95 (**2011**) 1253.

174. A. Rivaton, S. Chambon, M. Manceau, J.-L. Gardette, *Polym. Degrad. Stab*. 95 (**2010**) 278.

175. H. Neugebauer, C. Brabec, J. C. Hummelen, N. S. Sariciftci, *Sol. Energy Mater. Sol*. Cells 61 (**2000**) 35.

176. H. W. Sarkas, W. Kwan, S. R. Flom, C. D. Merritt, Z. H. Kafafi, *J. Phys. Chem*. 100 (**1996**) 5169.

177. S. R. Cowan, A. Roy, A. J. Heeger, *Phys. Rev. B* 82 (**2010**) 245207.

178. P. P. Khlyabich, B. Burkhart, B. C. Thompson, *J. Am. Chem. Soc*. 133 (**2011**)14534.

179. E. Voroshazi, B. Verreet, T. Aernouts, P. Heremans, *Sol. Energy Mater. Sol. Cells* 95 (**2011**) 1303.

180. G. Pfister, A. I. Lakatos, *Phys. Rev*. 6 (**1972**) 3012.

181. F. Yakuphanoglu, R. S. Anand, *Synth. Met*. 160 (**2010**) 2250.

182. Y.-M. Chang, W.-F. Su, L. Wang, *Sol. Energy Mater. Sol. Cells* 92 (**2008**) 761.

183. Y. He, H.-Yu Chen, J. Hou, Y. Li, *J. Am. Chem. Soc*. 132 (**2010**) 1377.

184. C.-H. Kim, M. Song, S.-Ho Jin, J. W. Lee, *Mol. Cryst. Liq. Cryst*. 538 (**2011**) 216.

185. A. Guerrero, L. F. Marchesi, P. P. Boix, J. Bisquert, G. Garcia-Belmonte, *J. Phys. Chem. Lett*. 3 (**2012**) 1386.

186. Y.-H. Lin, Y.-T. Tsai, C.-C. Wu, C.-H. Chiang, H.-F. Hsu, J.-J. Lee, C.-Y. Cheng, *Org. Electron*. 13 (**2012**) 2333.

187. K. Lee, J. Y. Kim, S. H. Park, S. H. Kim, S. Cho, and A. J. Heeger, *Adv. Mater*. 19 (**2007**) 2445.

188. J. Xiong, J. Yang, B. Yang, C. Zhou, X. Hu, H. Xie, H. Huang, Y. Gao, *Org. Electron*. 15 (**2014**) 1745.

189. J. Y. Kim, S. H. Kim, H. H. Lee, K. Lee, W. Ma, X. Gong, A. J. Heeger, *Adv. Mater*. 18 (**2006**) 572.

190. J. K. Lee, N. E. Coates, S. Cho, N. S. Cho, D. Moses, G. C. Bazan, K. Lee, A. J. Heeger, *Appl. Phys. Lett*. 92 (**2008**) 243308.

191. S. Cho, K. Lee, A. J. Heeger, *Adv. Mater*. 21 (**2009**) 1941.

192. J. Li, S. Kim, S. Edington, J. Nedy, S. Cho, K. Lee, A. J. Heeger, M. C.Gupta, J. T. Y. Jr, *Sol. Energy Mater. Sol. Cells* 95 (**2011**) 1123.

193. H.-L. Yip, A. K.-Y. Jen, *Energy Environ. Sci*. 5 (**2012**) 5994.

194. R. H. Friend, R. W. Gymer, A. B. Holmes, J. H. Burroughes, R. N. Marks, C. Taliani, D. D. C. Bradley, D. A. Dos Santos, J. L. Brédas, M. Lögdlund, W. R. Salaneck, *Nature* 397 (**1999**) 121.

195. H. Yamagata, F. C. Spano, *J. Chem. Phys*. 136 (**2012**) 184901.

196. L. H. Slooff, S. C. Veenstra, J. M. Kroon, D. J. D. Moet, J. Sweelssen and M. M. Koetse, *Appl. Phys. Lett*. 90 (**2007**) 143506.

197. R. Steim, F. R. Koglera, C. J. Brabec, *J. Mater. Chem*. 20 (**2010**) 2499.

198. S. J. Yoon, J. H. Park, H. K. Lee, O. O. Park, *Appl. Phys. Lett*. 92 (**2008**) 143504.

199. G. Grancini, M. De Bastiani, N. Martino, D. Fazzi, H.-J. Egelhaaf, T. Sauermann, M. R. Antognazza, G. Lanzani, M. Caironi, L. Franco, A. Petrozza, *Phys. Chem. Chem. Phys*. 16 (**2014**) 8294.

200. F. Deschler, A. D. Sio, E. von Hauff, P. Kutka, T. Sauermann, H. J. Egelhaaf, J. Hauch, E. Da Como, *Adv. Funct. Mater*. 22 (**2012**) 1461.

201. J. M. Shuo, L. H. Zhao, R. Q. Png, L. Y. Wong, P. J. Chia, J. C. Tang, S. Sivaramakrishnan, M. Zhou, E. C. W. Ou, S. J. Chua, S. W. Sim, L. L. Chua, P. K. H. Ho, *Adv. Mater*. 21 (**2009**) 4747.

202. D. H. Wang, S. H. Im, H. K. Lee, O O. Park, J. H. Park, *J. Phys. Chem. C* 113 (**2009**) 17268.

203. A. Roy, S. H. Park, S. Cowan, M. H. Tonh, S. Cho, K. Lee, A. J. Heeger, *Appl. Phys. Lett*. 95 (**2009**) 013302.

204. J. Kong, J. Lee, Y. Jeong, M. Kim, S.-O. Kang, K. Lee, *Appl. Phys. Lett*. 100 (**2012**) 213305.

205. A. Hayakawa, O. Yoshikawa, T. Fujieda, K. Uehara, S. Yoshikawa, *Appl. Phys. Lett*. 90 (**2007**) 163517.

206. U. Wurfel, D. Neher, A. Spies, S. Albrecht, *Nat. Commun*. 6 (**2015**) 1.

207. A. Guerrero, L. F. Marchesi, P. P. Boix, S. Ruiz-Raga, T. Ripolles-Sanchis, G. Garcia-Belmonte, J. Bisquert, *ACSNANO* 6 (**2012**) 3453.

208. P. Peumans, V. Bulovic and S. R. Forrest, *Appl. Phys. Lett*. 76 (**2000**) 2650.

209. C. Y. Nam, D. Su, C. T. Black, *Adv. Funct. Mater.* 19 **(2009**) 1.

210. M. Logdlund, J. L. Bredas, *J. Chem. Phys*. 101 (**1994**) 4357.

211. M. Wang, Q. Tang, J. An, F. Xie, J. Chen, S. Zheng, K. Y. Wong, Q. Miao, J. Xu, *Appl. Mater. Interface* 2 (**2010**) 2699.

212. F. C. Krebs, J. E. Carle, N. Cruys-Bagger, M. Andersen, M. R. Lilliedal, M. A. Hammond, S. Hvidt, *Sol. Energy. Mater. Sol. Cells* 86 (**2005**) 499.

213. A. Orimo, K. Masuda, S. Honda, H. Benten, S. Ito, H. Ohkita, H. Tsuji, *Appl. Phys. Lett*. 96 (**2010**) 043305.

214. T. D. Anthropoulos, T. S. Shafai, *Thin Solid Films* 441 (**2003**) 207.

215. E. J. Meijer, A. V. G. Mangnus, B.-H. Huisman, G. W. Hooft, D. M. deLeeuw, T. M. Klapwijk, *Synth. Met*. 142 (**2004**) 53.

216. M. S. A. Abdou, F. P. Orfino, Y. Son, S. Holdcroft, *J. Am. Chem. Soc*. 119 (**1997**) 4518.

217. S. Hoshino, M. Yoshida, S. Uemura, T. Kodzasa, N. Takada, T. Kamata, K. Yase, *J. Appl. Phys.* 95 (**2004**) 5088.

218. P. Kavak, U. D. Menda, E. A. Parlak, O. Ozdemir, K. Kutlu, *Sol. Energy Mater. Sol. Cells* 103 (**2012**) 199.

219. J. Bisquert, Garcia-Belmonte, A. Munar, M. Sessolo, A. Soriano, H. Bolink, *Chem. Phys. Lett*. 465 (**2008**) 57.

220. A. B. Guvenc, E. Yengel, G. Wang, C. S. Ozkan, M. Ozkan, *Appl. Phys. Lett*. 96 (**2010**) 143301.

221. S. Khelifi, K. Decock, J. Lauwaert, H. Vrielinck, D. Spoltore, F. Piersimoni, J. Manca, A. Belghachi, M. Burgelman, *J. Appl. Phys*. 110 (**2011**) 094509.

222. B. Ecker, J. C. Nolasco, J. Pallares, L. F. Marsal, J. Posdorfer, J. Paris, E. von Hauff, *Adv. Funct. Mater*. 21 (**2011**) 2705.

223. R. A. Street, M. Schoendorf, A. Roy, J. H. Lee, *Phys. Rev. B* 81 (**2010**) 205307.

224. D. Gao, B. Djukic, W. Shi, C. R. Bridges, L. M. Kozycz, D. S. Seferos, *Appl. Mater. Interface* 5 (**2013**) 8038.

225. Y. J. He, Y. F. Li, *Phys. Chem. Chem. Phys*. 13 (**2011**) 1970.

226. P. W. M. Blom, M. J. M. deJong, M. G. vanMunster, *Phys. Rev. B* 55 (**1997**) R656.

227. N. C. Nicolaidis, B. S. Routley, J. L. Holdsworth, W. J. Belcher, X. Zhou, P. C. Dastoor, *J. Phys. Chem. C* 115 (**2011**) 7801.

228. Sigma-Aldrich. URL http://www.sigmaaldrich.com. Web Accessed 12 June **2012**.

229. Y.-H. Lou, L. Zhang, M.-F Xu, Z.-K. Wanga, S. Naka, H. Okada, L.-S. Liao, *Org. Electron*. 15 (**2014**) 299.

230. J. H. Park, J. S. Kim, J. H. Lee, W. H. Lee, K. Cho, *J. Phys. Chem. C* 113 (**2009**) 17579.

231. M. A. Lampert, P.Mark, *Current injection in solids*, Academic Press, New York, **1970**.

232. Y. Udum, P. Denk, G. Adam, D. H. Apaydin , A. Nevosad, C. Teichert, M. S. White, N. S. Sariciftci, M. C. Scharber, *Org. Electron*. 15 (**2014**) 997.

233. C.-T. Sah, *IRE Trans. Electron Devices* 94 (**1962**) ED-9.

234. F. Zhang, Z. Zhuo, J. Zhang, X. Wang, X. Xu, Z. Wang, Y. Xin, J. Wang, J. Wang, W. Tang, Z. Xu, Y. Wang, *Sol. Energy Mater. Sol. Cells* 97 (**2012**) 71.

235. F. C. Krebs, H. Spanggaard, *Chem. Mater*. 17 (**2005**) 5235.

236. Y.-W. Su, S.-C. Lan, K.-H. Wei, *Mater. Today* 15 (**2012**) 554.

237. E.-P. Yao, Y.-J. Tsai, W.-C. Hsu, *Int. J. Photoenergy* 2014 (**2014**) 952528.

238. V. Shrotriya, J. Ouyang, R. J. Tseng, G. Li, Y. Yang, *Chem. Phys. Lett*. 411 (**2005**) 138.

239. B. C. Thompson, J. M. J. Frechet, *Angew. Chem. Int. Ed*. 47 (**2008**) 58.

240. B. A. Collins, Z. Li, J. R. Tumbleston, E. Gann, C. R. McNeill, H. Ade, *Adv. Energy Mater*. 3 (**2013**) 65.

241. G. J. Hedley, A. J. Ward, A. Alekseev, C. T. Howells, E. R. Martins, L. A. Serrano, G. Cooke, A. Ruseckas, I. D. W. Samuel, *Nat. Commun*. 4 (**2013**) 2867.

242. Z. Guo, D. Lee, R. D. Schaller, X. Zuo, B. Lee, T. Luo, H. Gao, L. Huang, *J. Am. Chem. Soc*. 136 (**2014**) 10024.

243. A. J. Barker, K. Chen, J. M. Hodgkiss, *J. Am. Chem. Soc*. 136 (**2014**) 12018.

244. F. Etzold, I. A. Howard, N. Forler, D. M. Cho, M. Meister, H. Mangold, J. Shu, M. R. Hansen, K. Müllen, F. Laquai, *J. Am. Chem. Soc*. 134 (**2012**) 10569.

245. I. A. Howard, R. Mauer, M. Meister, F. Laquai, *J. Am. Chem. Soc*. 132 (**2010**) 14866.

246. X. Shen, G. Han, D. Fan, Y. Xie, Y. Yi, *J. Phys. Chem. C* 119 (**2015**) 11320.

247. A. Tournebize, A. Rivaton, H. Peisert, T. Chassé, *J. Phys. Chem. C* 119 (**2015**) 9142.

248. M. C. Scharber, C. Lungenschmied, H.-J. Egelhaaf, G. Matt, M. Bednorz, T. Fromherz, J. Gao, D. Jarzab, M. A. Loi, *Energy Environ. Sci*. 4 (**2011**) 5077.

249. J. K. Lee, W. L. Ma, C. J. Brabec, J. Yuen, J. S. Moon, J. Y. Kim, K. Lee, G. C. Bazan, A. J. Heeger, *J. Am. Chem. Soc*. 130 (**2008**) 3619.
250. S. Ok, Y. Choe, *Mol. Cryst. Liq. Cryst*. 586 (**2013**) 95.
251. A. Ergete, F. K. Sabir, Y. Li, T. Yohannes, *J. Photonics for Energy* 5 (**2015**) 057209.
252. S. J. Lou, J. M. Szarko, T. Xu, L. Yu, T. J. Marks, L. X. Chen, *J. Am. Chem. Soc*. 133 (**2011**) 20661.
253. N. C. Greenham, X. G. Peng, A. P. Alivisatos, *Phys. Rev. B: Condens. Matter*. 54 (**1996**) 17629.
254. G. L. Schulz, M. Urdanpilleta, R. Fitzner, E. Brier, E. M. Osteritz, E. Reinold, P. Bäuerle, *Beilstein J. Nanotechnol*. 4 (**2013**) 680.
255. J. S. Moon, C. J. Takacs, S. Cho, R. C. Coffin, H. Kim, G. C. Bazan, A. J. Heeger, *Nano Lett*. 10 (**2010**) 4005.
256. Y. Yao, J. Hou, Z. Xu, G. Li, Y. Yang, *Adv. Funct. Mater.* 18 (**2008**) 1783.
257. L. Ye, S. Zhang, W. Ma, B. Fan, X. Guo, Y. Huang, H. Ade, J. Hou, *Adv. Mater*. 24 (**2012**) 6335.
258. S. R. Cowan, R. A. Street, S. Cho, A. J. Heeger, *Phys. Rev. B* 83 (**2011**) 035205.
259. F. Liu, W. Zhao, J. R. Tumbleston, C. Wang, Y. Gu, D. Wang, A. L. Briseno, H. Ade, T. P. Russell, *Adv. Energy Mater*. 4 (**2014**) 1301377.
260. I. Riedel, J. Parisi, V. Dyakonov, L. Lutsen, D. Vanderzande, J. C. Hummelen, *Adv. Funct. Mater*. 14 (**2004**) 38.
261. J. W. Jung, J. W. Jo, C.-C. Chueh, F. Liu, W. H. Jo, T. P. Russell, A. K.-Y. Jen, *Adv. Mater*. 27 (**2015**) 3310.
262. Z. Li, F. Gao, N. C. Greenham, C. R. McNeill, *Adv. Funct. Mater*. 21 (**2011**) 1419.
263. M. Lenes, M. Morana, C. J. Brabec, P. W. M. Blom, *Adv. Funct. Mater*. 19 (**2009**) 1106.
264. P. Schilinsky, C. Waldauf, C. J. Brabec, *Appl. Phys. Lett*. 81 (**2002**) 3885.
265. O. Sunseong, C. Youngson, *Mol. Cryst. Liq. Cryst.* 586 (**2013**) 95.
266. D. H. Wang, J. K. Kim, O. O. Park, J. H. Park, *Energy Envion. Sci*. 4 (**2011**) 1434.
267. K. Norrman, F. C. Krebs, *Sol. Energy. Mater. Sol. Cells* 90 (**2006**) 213.
268. S. Chambon, A. Rivaton, J.-L. Gardette, M. Firon, L. Lutsen, *J. Polym. Sci., Part A: Polym. Chem*. 45 (**2007**) 317.
269. K. Norrman, S. A. Gevorgyan, Krebs, *ACS Appl. Mater. Interfaces* 1 (**2009**) 102.
270. M.-J. Jin, J. Jo, J.-W. Yoo, *Org. Electron*. 19 (**2015**) 83.
271. Y. J. Kim, S. Ahn, D. H. Wang, C. Eon Park, *Appl. Phys. Lett*. 107 (**2015**) 063302.

272. A. Dualeh, T. Moehl, N. Tetreault, J. Teuscher, P. Gao, M. K. Nazeeruddin, M. Gratzel, *ACS Nano* 8 (**2014**) 362.
273. Y. Liang, Z. Xu, J. Xia, S.-T. Tsai, Y. Wu, G. Li, C. Ray, L. Yu, *Adv. Mater.* 22 (**2010**) E135.
274. G. Li, V. Shrotriya, Y. Yao, Y. J. Yang, *Appl. Phys*. 98 **(2005**) 043704.
275. P. E. Shaw, A. Ruseckas, I. D. W. Samuel, *Adv. Mater*. 20 (**2008**) 3516.
276. G. Yu, A. J. Heeger, *J. Appl. Phys*. 78 (**1995**) 4510.
277. P. K. Watkins, A. B. Walker, G. L. B. Verschoor, *Nano Lett*. 5 (**2005**) 1814.
278. J. E. Slota, X. He, W. T. S. Huck, *Nano Today* 5 (**2010**) 231.
279. Y. Yang, K. Lee, K. Mielczarek, W. Hu, A. Zakhidov, *Nanotechnology* 22 (**2011**) 485301.
280. H. Frohne, S. Shaheen, C. Brabec, D. Muller, N. Sariciftci and K. Meerholz, *Chem. Phys. Chem*. 3 (**2002**) 795.
281. A. Radivo, E. Sovernigo, M. Caputo, S. Dal Zilio, T. Endale, A. Pozzato, A. Goldonid, M. Tormen, *RSC Adv*. 4 (**2014**) 34014.
282. T.-W. Lee and Y. Chung, *Adv. Funct. Mater*. 18 (**2008**) 2246.
283. A. M. Nardes, M. Kemerink, R. A. J. Janssen, J. A. M. Bastiaansen, N. M. M. Kiggen, B. M. W. Langeveld, A. J. J. M. van Breemen, M. M. de Kok, *Adv. Mater*. 19 (**2007**) 1196.
284. G. Greczynski, T. Kugler, W. Salaneck, *Thin Solid Films* 354 (**1999**) 129.
285. D.-J. Yun, H. Ra, J. Kim, I. Hwang, J. Lee, S.-W. Rhee, J. Chung, *ECS J. Solid State Sci. Technol*. 1 (**2012**) M10.

Declaration

This thesis is my original work and has not been presented for a degree in any other university, and that all sources of financial and material used for the thesis have been duly acknowledged.

Endale Tsegaye______________________________
(PhD Candidate)

Professor Teketel Yohannes ____________________
(Advisor)